

# **Ultrasound-driven microbubble dynamics in microvessels**

---

**James Henry Bezer**

**Thesis submitted for the degree of Doctor of Philosophy**

**Imperial College London  
Department of Bioengineering  
January 2022**

# Declaration

The copyright of this thesis rests with the author. Unless otherwise indicated, its contents are licensed under a Creative Commons Attribution-Non Commercial 4.0 International Licence (CC BY-NC). Under this licence, you may copy and redistribute the material in any medium or format. You may also create and distribute modified versions of the work. This is on the condition that: you credit the author and do not use it, or any derivative works, for a commercial purpose. When reusing or sharing this work, ensure you make the licence terms clear to others by naming the licence and linking to the licence text. Where a work has been adapted, you should indicate that the work has been changed and describe those changes. Please seek permission from the copyright holder for uses of this work that are not included in this licence or permitted under UK Copyright Law

The work presented in this dissertation is the result of my own original research. Contributions from collaborators have been clearly indicated and all source material has been appropriately referenced and acknowledged.

James Bezer  
September 2021

# Abstract

Ultrasound and microbubble induced blood-brain barrier opening has shown success in clinical trials as a promising method to deliver drugs to the brain. Shelled gas bubbles, a few micrometres in diameter, are administered intravenously, and distribute throughout the cardiovascular system. When ultrasound is applied to the brain, the microbubbles expand and contract within the vasculature, temporarily disrupting the blood-brain barrier, and allowing drugs to pass through. While this technique has been shown to be effective at delivering drugs, its mechanisms remain relatively poorly understood. Better understanding how microbubbles interact with tissues could enable refinement of therapies.

This thesis investigates the fundamental physical interactions between microbubbles and soft tissues using two distinct but related experimental platforms that utilise high-speed microscopy. Firstly, microbubbles within soft tissue-mimicking hydrogel channels are observed during exposure to typical therapeutic ultrasound pulses. The primary radiation force is shown to be significant, and can cause bubbles to deform the soft gels by several micrometres.

Microbubbles are also investigated in brain tissue, using acute cortical slices from the brains of juvenile rats, transcardially perfused post-mortem with a concentrated solution of SonoVue®. This technique is shown to be an effective method of observing microbubbles using optical microscopy within the microvasculature of live brain tissue. Radial oscillations of bubbles within brain microvessels can deform surrounding tissue at both microsecond and millisecond time scales. Extravasation of microbubbles due to the primary radiation force can occur during typical ultrasound pulses, and is common at higher ultrasound pressures (mechanical index of 0.6 and above).

These results demonstrate the significance of both radial oscillations and the primary radiation force as ways in which microbubbles can physically impact their surroundings. Additionally, acute brain slices are shown to be a valuable tool to investigate microbubble behaviours and mechanisms of drug delivery in a physiologically relevant environment.

# Acknowledgements

I would first and foremost like to thank my supervisor Dr James Choi, who has been hugely supportive throughout the many highs and lows of my PhD. His guidance has been instrumental in enabling all aspects of my development as a researcher over the years we have worked together.

For their assistance with Chapter 2: I would like to thank Dr Hasan Koruk, for his invaluable help with the modelling, Dr Akaki Jamburidze and Dr Valeria Garbin, for their advice and assistance with preliminary experiments, and Dr Christopher Rowlands, for helping me design the optical apparatus.

For their assistance with Chapters 3 and 4: I am deeply indebted to Dr Andrei Kozlov, for training me in how to perform experiments with brain tissue, and for his advice throughout. I am grateful to Dr Paul Prentice for providing the Shimadzu HPV camera, for his assistance in using it, and for his advice more generally. I also wish to thank Dr Sophie Morse and William Lim Kee Chang for assisting with the data analysis, Zheng Jiang for building the transducer I used in Chapter 4, and Professor Simon Schultz for kindly allowing me to use his tissue slicer.

I would also like to thank everyone else with whom I have worked over the course of my PhD, who have provided me with less specific but no less valuable support: Dr Ahmed El-Ghamrawy, Krit Sujarittam, Shusei Kawara, Dr Ellie Watts, Dani Chattenton, Betul Ilbilgi Yildiz, Matthew Copping, Charlotte Bouldin, Dr Gerard Hernandez Mir, and Dr Antonios Pouliopoulos.

I would finally like to thank my friends, my parents, and Raquel for supporting me throughout.

This PhD was funded by the EPSRC Centre for Doctoral Training in Medical Imaging at King's College London and Imperial College London (Grant EP/L015226/1).

# List of publications

## Journal papers

1. Bezer JH, Prentice P, Lim Kee Chang W, Morse SV, Christensen-Jeffries K, Rowlands CJ, Kozlov AS, Choi JJ Microbubble dynamics in brain microvessels *Submitted for review* **(Chapters 3 and 4)**
2. Bezer JH, Koruk H, Rowlands CJ, Choi JJ Elastic deformation of soft tissue-mimicking materials using a single microbubble and acoustic radiation force. *Ultrasound in Medicine & Biology* (2020) 46(12), pp.3327-3338. **(Chapter 2)**
3. Pouliopoulos AN, Smith CA, Bezer JH, El Ghamrawy A, Sujarittam K, Bouldin CJ, Morse SV, Tang MX, Choi JJ. Doppler Passive Acoustic Mapping. *IEEE Transactions on Ultrasonics, Ferroelectrics, and Frequency Control*. (2020) Jul 24;67(12):2692-703.

## Conference presentations

1. Bezer JH, Prentice P, Rowlands CJ, Kozlov AS, Choi JJ. Acoustic Cavitation of Microbubbles in Cerebral Microvessels. 20<sup>th</sup> International Symposium on Therapeutic Ultrasound (ISTU), Gyeongju, South Korea (June 2021) (Oral + poster) *Best Student Poster Presentation*
2. Bezer JH, Koruk H, Rowlands CJ, Choi JJ. Single microbubble-induced tissue deformation to estimate tissue properties. 25<sup>th</sup> European Symposium on Ultrasound Contrast Imaging, Rotterdam (January 2020) (Poster)
3. Bezer JH, Koruk H, Jamburidze A, Garbin V, Choi JJ. Single-bubble-induced elastic deformation of capillary-mimicking hydrogel channels. 24<sup>th</sup> European Symposium on Ultrasound Contrast Imaging, Rotterdam (January 2019) (Poster)

# Contents

Declaration	2
Abstract	3
Acknowledgements	4
List of publications	5
Contents	6
List of Figures	9
<b>Chapter 1: Introduction</b>	<b>16</b>
1.1 Background and motivation	16
1.2 Medical applications of ultrasound and microbubbles	19
1.3 Physics of ultrasound driven microbubbles	26
1.4 Blood-brain barrier opening	36
1.5 Aims and scope of the thesis	49
<b>Chapter 2: Microbubble-induced elastic deformation of soft tissue mimicking materials using the primary radiation force</b>	<b>51</b>
2.1 Introduction	51
2.2 Methods	61
2.2.1 Microbubble preparation	61
2.2.3 Gel channel preparation	62
2.2.3 Gel channel characterisation	63
2.2.4 Optical setup	67
2.2.5 Ultrasound experiments	68
2.2.6 Transducer calibration	69
2.2.7 Image analysis	71
2.2.8 Data analysis	75
2.2.9 Modelling	76
2.3 Results	77

---

2.3.1 Selection of channel diameter	77
2.3.2. Feasibility of elastic indentation with a single microbubble	77
2.3.3 Estimates of applied force	81
2.3.4 Qualitative observations	82
2.4 Discussion	84
2.5 Conclusions	87
<b>Chapter 3: Microbubble interactions with brain microvessels</b>	<b>88</b>
3.1 Introduction	88
3.1.1 Tissue models for observation of microbubbles	89
3.1.2 Aims and outline of study	91
3.2 Methods	92
3.2.1 Preparation of slices	92
3.2.3 Microinjection of microbubbles	94
3.2.3 Vessel contrast and markers of extravasation	95
3.2.4 Ultrasound experiments	98
3.2.5 Optics – high-speed imaging	100
3.2.6 Optics – ultra-high-speed imaging	101
3.2.7 Analysis of videos	102
3.2.8 Tissue viability assay	102
3.3 Results	105
3.3.1 Feasibility of direct observation of microbubble dynamics in acute brain slices	105
3.3.2 Microsecond time scales	107
3.3.3 Millisecond time scales	112
3.3.4 Tissue viability	118
3.4 Discussion	121
3.5 Conclusion	128
<b>Chapter 4: Effects of ultrasound parameters on microbubble extravasation and destruction</b>	<b>129</b>
3.1 Introduction	129

---

---

3.2 Methods	133
3.2.1 Simulations	133
3.2.3 Experimental methods	134
3.2.3 Analysis	136
3.2.4 330 kHz transducer calibration	137
3.2.5 Short pulse generation	138
3.3 Results	141
3.3.1 Parameter selection – simulations	141
3.3.2 Microbubble extravasation	143
3.3.3 Dissolution of microbubbles	147
3.4 Discussion	150
3.5 Conclusion	154
 <b>Chapter 5: Conclusions</b>	 155
 <b>References</b>	 159



---

# List of figures

Figure 1.1: In-house manufactured lipid-shelled microbubbles under the microscope. 21

Figure 1.2: A) Demonstration of surface tension as a function of radius predicted by the Marmottant model for a microbubble with 2  $\mu\text{m}$  initial radius, using parameters from (Tu et al. 2009), showing buckled, elastic, and ruptured regimes. B) Radius-time curve predicted for a Sonovue microbubble from the Marmottant model for a microbubble driven with a 1 MHz ultrasound pulse at either 600 kPa (Blue) or 60 kPa (Red) PNP, at the same phase. The oscillations are approximately sinusoidal at low pressures, but become highly nonlinear at high pressures. 30

Figure 1.3: Cross-sectional view of the neurovascular unit. 37

Figure 2.1: Schematic of the bubble indentation model used, illustrating the impact of a bubble into a viscoelastic material. 53

Figure 2.2: Model predictions for a variety of parameters. A) Indentation of a 2  $\mu\text{m}$  radius bubble indenting into a 2 kPa, 0.15 Pa s gel at three different force values. B) Indentation of three different bubble radii indenting into a 2 kPa, 0.15 Pa s gel exposed to a radiation force of 5 nN. C) Indentation of a 2  $\mu\text{m}$  radius bubble exposed to a 10 nN force indenting into a 2 kPa gel, with varying viscosity values. D) Indentation of a 2  $\mu\text{m}$  radius bubble exposed to a 10 nN force indenting into gels with Young's Moduli of 2 kPa, 4.7 kPa and 8.5 kPa. 57

Figure 2.3: Size distribution of in-house manufactured microbubbles used in this study based on a sample of 1805 bubbles. 61

Figure 2.4: Scaffold used to construct the wall-less channel. Left) CAD file showing the key support structures of the channel's scaffold. Right) The scaffold was 3D-printed and assembled with a cover slip and needles. This final structure was used to form the channel and introduce the microbubble solution. 63

**Figure 2.5:** Attenuation of ultrasound by polyacrylamide gels A) Amplitude spectrum of reflected pulses through water, 2 kPa, 4.5 kPa, and 8.7 kPa gels. Error bars indicate standard deviation across 5 gels. B) Attenuation spectra of the three gels relative to water, demonstrating negligible attenuation at 1 MHz through any of the gels tested. The uncertainties are increased at high and low frequencies due to the lower signal amplitudes.

65

**Figure 2.6:** Confocal images of wall-less channels in 2 kPa Young's modulus polyacrylamide gel after introduction of quantum dots. A-B) Z-projections (vertical projection) of cross-sections through 100 (A) and 25  $\mu\text{m}$  (B) diameter channels. C) Confocal maximum intensity projection and D) Brightfield image of the 100  $\mu\text{m}$  channel. E) Maximum intensity projection of the 25  $\mu\text{m}$  channel. The channel could not be clearly resolved on the equivalent brightfield image. Scale bars: 25  $\mu\text{m}$ .

66

**Figure 2.7:** Setup used for acoustic experiments. The channel was formed in a 3D-printed chamber, and was placed in a water tank under an objective lens.

68

**Figure 2.8:** 1-MHz transducer beam profile. Left) Axial-lateral profile (transducer at the top of the image). Right) Horizontal beam profile at the focus. Step size 0.5 mm. The peak pressure at the focus was 400 kPa. The pulse length used was 10 cycles, chosen to avoid reflected pulses affecting the measurements, while being long enough to ensure a steady-state maximum pressure amplitude.

70

**Figure 2.9:** Automated segmentation of bubbles in high-speed video images. A) Example image of bubble used to generate plots in C and D. B) Bubble image overlaid with circles obtained from the code at intensity thresholds of 0.1 (red), 0.2 (green) and 0.3 (blue). C) Effect of intensity threshold on values of bubble radius for a sensitivity value of 0.8. D) Effect of sensitivity value and intensity threshold on measured bubble radius. Values of zero indicate that no bubble could be found in the image.

73

**Figure 2.10:** Brightfield image of microbubbles within a 10  $\mu\text{m}$  diameter channel in 8.5 kPa Young's modulus polyacrylamide gel.

77

**Figure 2.11:** Feasibility of elastic indentation with a single microbubble. Microbubbles in a 25  $\mu\text{m}$  diameter channel (highlighted) in 2 kPa polyacrylamide gel, exposed to a 2 ms, 600 kPa PNP, 1 MHz pulse. The bubbles indent into the gel by around 2  $\mu\text{m}$ , before relaxing back to within the channel. Left-to-Right: Before (0 ms),

maximum indentation (2 ms), after (5 ms), colour image with the before (green) and maximum indentation (magenta) images overlaid. The bubbles move slightly towards each other during the sonication due to secondary radiation forces. Ultrasound propagates from left to right. 78

Figure 2.12: Example indentation curves for four individual bubbles impacting gels with different stiffnesses. Frames from each video are shown on the left, with the x-coordinate of the centre of the bubble shown over time in a plot on the right. Arrows indicate the points at which each still was taken. The duration of the pulse is shaded in blue. Curves fitted to the data based on the mathematical model are represented by dashed lines in red. These curves were used to extract the radiation force on each bubble and the viscosity of the gel. The white arrow indicates the direction of wave propagation (left-right in all images). (a) Example deformation curve for a 2.0  $\mu\text{m}$  radius bubble indenting a gel with a Young's modulus of 2 kPa. Frame rate: 4,858 frames per second (fps). Parameters extracted from the model are radiation force = 19 nN and viscosity = 0.12 Pa s. (b) Bubble radius = 1.5  $\mu\text{m}$ . Gel Young's modulus = 2 kPa. Frame rate = 31,197 fps. Radiation force = 13 nN, viscosity = 0.18 Pa s. (c) Bubble radius = 1.5 mm. Gel Young's modulus = 4.5 kPa. Frame rate = 31,197 fps. Radiation force = 15 nN, viscosity = 0.12 Pa s. (d) Bubble radius = 1.6 mm. Gel Young's modulus = 8.7 kPa. Frame rate = 31,197 fps. Force = 4.5 nN, viscosity 0.2 Pa s. 79

Figure 2.13: Maximum indentation depth vs initial bubble radius for two different channel diameters and three different gel stiffnesses. The uncertainty in measurements of radius is approximately 0.2  $\mu\text{m}$ . The uncertainty in indentation depth is approximately 0.3  $\mu\text{m}$ . 82

Figure 2.14: Examples of non-spherical oscillations of a large microbubble (L: before and R: during a 10 ms pulse). Despite the low frame rates used here, it is clear in this video that the bubble is not spherically symmetric. 83

Figure 3.1: Size distribution of SonoVue, measured optically using the technique described in Chapter 2. 93

Figure 3.2: Feasibility of microinjecting a dye into a microvessel of a rat brain slice. A micropipette is inserted into a microvessel and dye is successfully injected with minimal leakage (Left: before; Right: after). Scale: 50  $\mu\text{m}$ . 95

---

Figure 3.3: Experimental setup for the slice experiments. a) Setup for 5.58 kfps imaging with parallel colour camera, illuminated with an LED gooseneck light. b) Ultra-high speed imaging apparatus using a single 10 Mfps camera, illuminated with a pulsed laser. 98

Figure 3.4: Chamber used for slice experiments, constructed of three pieces of Perspex with mylar sides. A cover slip is glued over the bottom to increase the passage of light through. During experiments, a layer of agarose is placed at the base of the chamber. 99

Figure 3.5: Pressure calibration taken without (blue) and inside (red) the slice box. The pressure amplitudes are indistinguishable, although there are some slight differences in the shapes of reflected pulses afterwards. This also highlights the rapid ramp-up time of the transducer, and stable maximum signal amplitude. 100

Figure 3.6: A) Colour image of microbubble in a microvessel B) Monochrome and equivalent colour image taken at 5,480 fps in a different slice. Scale: 10  $\mu\text{m}$  105

Figure 3.7: A microbubble in a microvessel, exposed to an 800 kPa, 1 MHz, 15 cycle pulse and imaged at 10 Mfps. The vessel walls oscillate with the bubble. The bubble oscillations are not temporally symmetric throughout the pulse, with a much longer expansion phase than collapse phase. The smallest size the bubble reaches is too small to be resolved by the camera used here as shown in the image at 14.2  $\mu\text{s}$ . The streak image below is taken along the dotted line 107

Figure 3.8: Asymmetric oscillations of a microbubble in a small microvessel. A) 4 example frames of bubble showing asymmetric oscillations within a microvessel. Scale = 10  $\mu\text{m}$  B) Radius-time curve of the bubble in A along (red) and perpendicular to the midline of the vessel 108

Figure 3.9: A) Frames from a video showing extravasation of a microbubble from a microvessel, when exposed to a 600 kPa, 10 ms ultrasound pulse. B) Extravasation of a microbubble during a 400 kPa, 10 ms pulse, showing penetration into the tissue. C) Frames of a video taken at 5 Mfps showing extravasation of a microbubble from a microvessel when exposed to a 1 MPa pulse. The shape of the vessel has changed after the pulse. D) Radius-time curve for the microbubble in C which extravasates, taken until the moment the bubble passes through the wall of the vessel and is no longer approximately spherical. 110

Figure 3.10: Coalescence of two microbubbles within a small microvessel, imaged at 10 Mfps. While it is difficult to define the exact moment of coalescence, the two bubbles coalesce in less than approximately 8 acoustic cycles. Scale = 10  $\mu\text{m}$ . 111

Figure 3.11: Motion of microbubbles within microvessels exposed to 10 ms pulses at different peak negative pressures. A) 400 kPa, B) 600 kPa, C) 400 kPa. Microbubbles generally move in the direction of wave propagation (Left – Right), but their motion can be very erratic. Scale = 10  $\mu\text{m}$ . 113

Figure 3.12: Deformation of surrounding tissues by microbubble oscillations over a 10 ms pulse. Slices were exposed to A) 200 kPa, B) 600 kPa (the red line shows the path of the microbubble during the pulse), and C) 400 kPa pulses. Even at quite low pressures, microbubbles can deform the surrounding tissue over quite a large area. Scale bars: 10  $\mu\text{m}$ . Colour bars are in micrometres, distance moved perpendicular to the vessel wall. 115

Figure 3.13: Vasoconstriction in a microvessel (likely to be an arteriole) after exposure to a single 600 kPa, 10 ms ultrasound pulse applied at 0 seconds (vertical line). A): frames from colour image taken (L-R) before, immediately after, and 30 seconds after the pulse. The vessel contains two large bubbles (arrows), one of which is out of the focal plane, and which both disappear after the pulse. Scale = 10  $\mu\text{m}$ . B): Vessel diameter over time, based on Full-width half maximum of the image intensity taken along the dotted line denoted in A. 116

Figure 3.14: A) Microstreaming in a microvessel around a large microbubble. Images taken at 0, 7 and 12 milliseconds after the start of a 10 ms pulse. The microbubble oscillations disturb the distribution of ink particles nearby. B) Dissolution of the bubble after microstreaming. Images shown are (L-R) before the pulse, immediately after the pulse, and 14 seconds after the pulse (at the point the large bubble is no longer visible). Scale = 10  $\mu\text{m}$ . 117

Figure 3.15: TTC staining results. All three groups of samples show some red staining, although this is considerably more pronounced in the 0 and 2h aCSF groups, which indicate the start and end of the typical recording periods. In both of these groups, there are regions which have not been stained, however. Scale: 5 mm. 119

Figure 3.16: Bar plot showing mean colour saturation for the cortex of each group of TTC stained slices. Error bars are standard deviations between slices. \*  $p=0.040$ , \*\*\*  $p=8.4e-5$  120

Figure 4.1: Beam profile of in-house manufactured 330 kHz transducer, measured at a centre frequency of 330 kHz, PNP of 100 kPa, and pulse length of 20 cycles. The focus is very close to the surface of the transducer (approximately 5 mm). 138

Figure 4.2: 330 kHz PZT transducer built in-house. Ruler scale is in centimetres. 138

Figure 4.3: Pulse shape for 5 cycle input pulses generated by 1 MHz Olympus (above) and 330 kHz in-house (below) transducers. Time measured from the start of the pulse output by the function generator to the transducer. The 1 MHz pulse has a short ramp up time and the peaks are approximately uniform. The 330 kHz transducer has significant ringing. 140

Figure 4.4: Predicted time-average radiation force on a bubble of different radii when exposed to an ultrasound pulse. at 1 MHz and 330 kHz at an MI of A) 0.2, B) 0.4, and C) 0.6. D) is the same as A but with a smaller y-scale. Red: 1MHz; Blue: 330 kHz at the same MI as 1 MHz; Cyan: 330 kHz at the same pressure as 1 MHz. The trends vary considerably at different pressures. However, by matching mechanical index across frequencies, the radiation force appears to be kept much more similar than by matching pressures. 142

Figure 4.5: Extravasation of a microbubble exposed to a 330 kHz. 0.6 MI, 10 ms ultrasound pulse. Top: Colour image from before the pulse, showing the bubble in the vessel. Bottom: Still images taken at (L-R) Before, 0.18, 0.91, 3.28 and 4.19 ms after the start of the pulse. The maximum expansion of the microbubble grows very significantly during the pulse. Scale: 10  $\mu\text{m}$ . 143

Figure 4.6: Extravasation of microbubbles at 1 MHz. A) Extravasation of microbubbles indicating bubble initial radius and ultrasound mechanical index. Red: extravasated; Green: Did not extravasate; Brown: unclear. B) Probability of microbubble extravasation at 1 MHz over mechanical indices. C) Angles of vessels containing microbubbles sonicated at each pressure. Radial axis indicates number of videos in each bin. 144

Figure 4.7: Extravasation of microbubbles at 330 kHz. A) Extravasation of microbubbles indicating bubble initial radius and ultrasound mechanical index of a 330 kHz, 10 ms pulse. Red: extravasated; Green: Did not extravasate; Brown: unclear. A mechanical index of 0.8 could not be tested, as in Figure 4.6, due to the

---

limitations of the transducer B) Probability of microbubble extravasation at 330 kHz over different mechanical indices. C) Angles of vessels containing microbubbles sonicated at each pressure 145

Figure 4.8: Examples of dissolution of microbubbles (highlighted with arrows) with (Top) 10 ms pulses (following extravasation) and (Bottom) RaSP, both at 400 kPa, 1 MHz. Scale: 10  $\mu$ m 147

Figure 4.9: Probability of dissolution of microbubbles over a 30 second period after exposure to RaSP or 10 ms tone bursts, at either 0.2 or 0.4 MPa at 1 MHz. There were 10 bubbles in each group. Grey: Did not dissolve, Blue: dissolved 148

Figure 4.10: Time to dissolution of microbubbles vs bubble diameter with RaSP vs 10 ms tone bursts at 0.2 and 0.4 MPa at 1 MHz. There is no clear trend in dissolution time with bubble diameter 148

## List of tables

Table 1: Parameters used in simulations 134





# Chapter 1: Introduction

## **1.1 Background and motivation**

Ultrasound is a common diagnostic tool in medicine. It is valued for enabling high spatial and temporal resolution images of internal anatomy and function to be obtained safely, quickly, and cost-effectively (Bushberg et al.). Ultrasound also has several therapeutic applications, particularly shock-wave lithotripsy to break up kidney and gall stones which is in common clinical use (Lingeman et al. 2009), but also many emerging techniques such as tissue fractionation, and thermal ablation via high intensity focussed ultrasound (HIFU), the latter of which is beginning to have more widespread clinical applications (ter Haar and Coussios 2007).

Both imaging and therapeutic applications of medical ultrasound have been expanded and enhanced by the introduction of microbubble contrast agents: small gas bubbles around 1 – 10  $\mu\text{m}$  in diameter, usually with a lipid coating, that can be administered intravenously. Microbubbles are a common tool in clinical imaging, as they scatter sound more effectively than tissue, generating greater contrast. Their size confines them to the vasculature, while being small enough to enable passage through even the narrowest microvessels. This makes them particularly valuable in diagnosing pathologies characterised by abnormal patterns of blood flow, such as cardiovascular disease and certain solid tumours (Cosgrove 2006; Shiina et al. 2015).

Microbubbles also have a range of potential therapeutic applications including drug delivery via drug-loaded microbubbles (Sirsi and Borden 2014); breaking up thromboses through cavitation (De Saint Victor et al. 2014); and enhancing vascular permeability to drugs (Burgess et al. 2014). When microbubbles are exposed to ultrasound, they exert forces on their surroundings, either through their oscillations, or through their translational motion. These forces are likely to play a major role in many therapeutic aspects of bubbles, such as blood-brain barrier opening and sonothrombolysis

(disruption of thromboses using ultrasound) (Roovers et al. 2019). These forces could also have applications in diagnostics, as the way bubbles respond to sound is intimately related to the mechanical properties of surrounding tissues (Qin et al. 2009; Qin and Ferrara 2006; Sassaroli and Hynynen 2005).

Most therapeutic effects of microbubbles in drug delivery, particularly blood-brain barrier permeabilisation, are believed to be achieved in capillaries and other small microvessels. The average capillary diameter is 3-4  $\mu\text{m}$  in mice (Steinman et al. 2017) and 6-7  $\mu\text{m}$  in humans (Karbowski 2011), only slightly larger than the majority of bubbles administered. This high degree of confinement can significantly affect the way bubbles respond to ultrasound compared to their dynamics in a free fluid, by constraining their oscillations, and introducing spatial asymmetry (Caskey et al. 2006).

A detailed understanding of how bubbles behave within small, compliant blood vessels, both in terms of the effects they have on tissue, and how their behaviour changes under confinement, is crucial as a way of enabling us to elucidate the mechanisms of many therapeutic applications. Better understanding single bubble dynamics in real tissue may also help us optimise their diagnostic and therapeutic roles while improving safety.

Previous theoretical research on the interactions between microbubbles and their surroundings has been relatively extensive, but has often lacked solid experimental comparisons of bubbles in physiologically relevant environments. Several papers have been published which predict the effect on a compliant vessel of the oscillations of a microbubble within, for instance (Doinikov et al. 2019; Wang et al. 2013). However, direct observations of bubbles interacting with blood vessels have been limited in previous literature, and most experimental studies on the effects of bubbles have focussed on whole animal effects, or changes in tissues analysed post mortem after ultrasound exposure (Sheikov et al. 2004; Sheikov et al. 2006).

This thesis aims to investigate the forces and mechanical effects that a microbubble exerts on its surroundings during ultrasound pulses typical of those used in blood-brain barrier opening, and in environments with similar properties to the brain microvasculature. This is achieved by direct observation of bubble and tissue motion under sonication, using high speed microscopy. Particular focus is given to the primary radiation force microbubbles exert on artificial microvessels, and the effects microbubble motion has on the displacement and deformation of brain tissue in response to typical ultrasound parameters used for blood-brain barrier permeabilisation. Observations are made of dynamics at both microsecond and millisecond time scales, incorporating microbubble and vessel wall oscillations at MHz-frequencies, and bubble and tissue movement over millisecond-long pulses.

## **1.2 Medical applications of ultrasound and microbubbles**

This section summarises a range of clinically established and emerging applications of ultrasound in medicine, including how ultrasound alone can be used, and especially how it can be combined with contrast agents and other acoustically active particles to enhance its diagnostic and therapeutic capabilities. This will provide broader context for where microbubble therapies sit within the applications of ultrasound.

### **1.2.1 Ultrasound in medicine**

Ultrasound imaging has been a widespread and important tool in diagnostic medicine for many decades. By forming images of internal anatomy using echoes from sound waves, ultrasound is particularly valued for its good soft-tissue contrast, excellent temporal resolution, and low cost. Importantly, it is regarded as very safe, without requiring tissue to be exposed to ionising radiation or intense magnetic fields (Wells 2006).

Ultrasound images are formed by generating a short ultrasound impulse from an array of transducer elements. This impulse propagates through the body and is reflected off surfaces where there is a change in acoustic impedance, such as the edges of organs or structures within organs. A B-mode image is reconstructed based on the intensity of the received pulse and its time of flight.

Transthoracic or transabdominal ultrasound imaging is typically performed at frequencies of 2-10 Megahertz. This provides an optimal balance between the need for high spatial resolution (requiring a high frequency), and tissue penetration depth (requiring a low frequency). In imaging applications requiring high spatial resolution, and where the probe can be placed very close to the structure of interest (such as in intravascular ultrasound or ophthalmologic applications), higher frequencies can be used (Wells 2006).

Ultrasound is not merely a passive imaging modality, however. With long duration pulses, attenuation of ultrasound can be used to exert a force on tissue, known as an Acoustic Radiation Force (ARF) (Nightingale 2012). ARF imaging is a way to determine relative tissue stiffness based on how far tissue displaces due to an applied acoustic force. These forces can also be used to generate perpendicularly propagating shear waves through tissue (Shiina et al. 2015). By measuring the speed of propagation of these waves, tissue stiffness can be objectively quantified. Measuring tissue stiffness is valuable, as changes in stiffness is associated with many pathologies, such as cancer and vascular disease (Ramnarine et al. 2014; Yeh et al. 2002).

Therapeutic applications include High Intensity Focused Ultrasound (HIFU), in which a focussed beam of ultrasound is delivered to a region of tissue, increasing its temperature and ablating regions of abnormal tissue. This technique has been quite widely applied clinically to treat specific conditions such as uterine fibroids (Zhang et al. 2015), and is also an emerging treatment for essential tremors and Parkinson's disease, by ablating the Vim nucleus of the thalamus in the brain (Dick and Gedroyc 2010; Martínez-Fernández et al. 2018). It has also been proposed as a treatment for a number of cancers, such as prostate cancer, as an alternative or adjunct to radiotherapy or surgery (ter Haar and Coussios 2007). The results of clinical trials have however shown uncertain efficacy of HIFU in cancer however, for instance in the treatment of prostate cancer (Lukka et al. 2011).

An alternative method of tissue ablation is histotripsy, in which extremely high amplitude, short duration ultrasound pulses are delivered to the tissue. This approach fractionates tissue into liquid purely through cavitation and expansion of bubbles formed in the tissue due to the large negative pressures; the short pulses mean the tissue does not heat up significantly. This technique is under clinical investigation for a number of pathologies (Khokhlova et al. 2015).

Using ultrasound to modify brain activity, a process known as neuromodulation, has also been widely studied in recent years. The majority of these studies have been performed without

microbubbles, or any other agents introduced externally. Merely applying ultrasound to specific brain regions can affect neural behaviour. The precise mechanisms are unclear (Fini and Tyler 2017; Tyler 2011).

### 1.2.2 Contrast enhanced ultrasound imaging

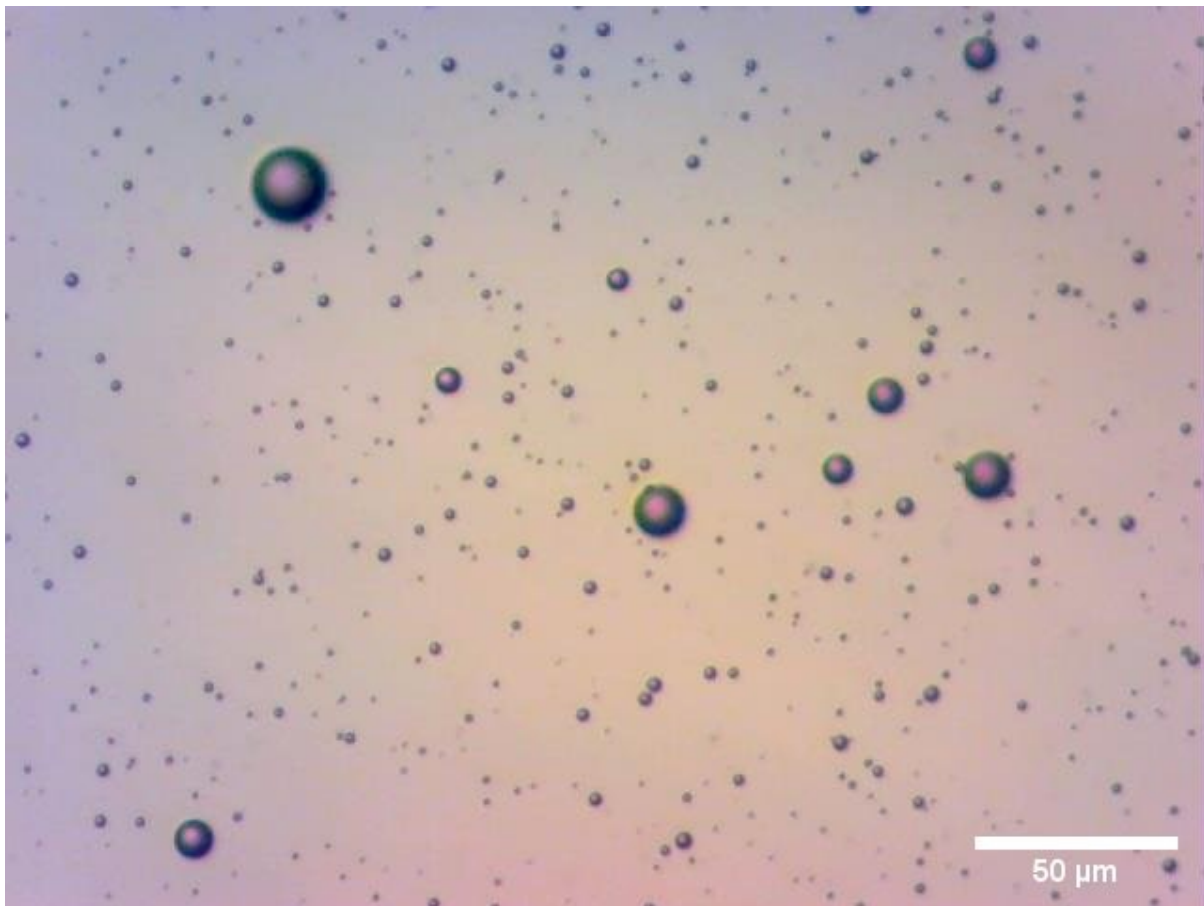


**Figure 1.1:** In-house manufactured lipid-shelled microbubbles under the microscope.

A major development in ultrasound imaging over the last few decades has been the widespread introduction of ultrasound contrast agents, or microbubbles. Microbubbles are small gas bubbles, around 1-10  $\mu\text{m}$  in diameter, coated with a shell. This shell is typically made of lipids, although proteins such as albumin, and polymer microbubbles have also been used. Lipid-shelled microbubbles are designed to remain stable in the blood (Figure 1.1), often featuring polyethylene

glycol derivatives within the shells to promote bubble formation, inhibit coalescence, and reduce adsorption of blood plasma proteins (Ferrara et al. 2009; Owen et al. 2019). Several different types of gas have been used as microbubble cores, although the most common gases used now are Perfluorobutane (for instance in Definity microbubbles) and sulphur hexafluoride (in SonoVue), both chosen due to their safety profile and high molecular weight (which reduces the rate of gas diffusion out of the bubble) (Faez et al. 2013).

Microbubbles are similar in size to red blood cells, and so they can flow freely through the bloodstream, including many of the smallest capillaries. Because of their size, microbubbles do not naturally extravasate and so remain within the vasculature. This makes them excellent tools for imaging patterns of blood flow (Cosgrove 2006). They have achieved widespread use in cardiac imaging, as a way of enhancing imaging of myocardial perfusion, and can also be used to increase the signal to noise ratio of blood flow in Doppler imaging (Kaufmann et al. 2007). They are also valuable in abdominal imaging, especially as a tool for investigating liver masses. Microbubbles also enable pathologies with abnormal vascularity, such as haematomas, to be more easily diagnosed and differentiated (Wilson and Burns 2010).

Microbubbles make effective contrast agents as they are highly compressible, and have a much higher acoustic impedance than surrounding tissues at ultrasound frequencies. When in an ultrasonic pressure wave, they expand and contract in response to the compressions and rarefactions of the sound wave. This means they produce far greater scattered signal than their surroundings, making them easy to identify on an ultrasound scan. Microbubbles resonate at frequencies typically used for ultrasound imaging. Microbubbles also respond to ultrasound highly nonlinearly, producing characteristic harmonic frequencies in their scattered acoustic spectrum that are not present in signal from tissue, which is approximately linear. This nonlinear response can also be exploited by using pulse inversion imaging techniques, by subtracting the scattered spectra received from an incident pulse and its mirror image (Helfield 2019; Wells 2006).

Microbubbles have a relatively short lifespan in the bloodstream. For instance, SonoVue™ microbubbles intravenously administered to human patients have a distribution half-life of about 1 minute and an elimination half-life of about 6 minutes. The gas inside the bubbles is quickly exhaled through the lungs: more than 80% of the administered gas is exhaled via the lungs after 11 minutes (Schneider 1999).

An emerging application of microbubbles in imaging has been ultrasound molecular imaging, where receptors are attached to the shells of microbubbles, which can bind to specific ligands on the surfaces of vascular endothelial cells. These have shown particular clinical interest as a way of monitoring expression of VEGFR2, a marker for angiogenesis in tumours (Abou-Elkacem et al. 2015).

### **1.2.3 Microbubbles in therapy**

A great deal of recent research has focussed on the potential applications of microbubbles in therapies. Microbubble cavitation can be used to enhance and target tissue fractionation, including as a method of disrupting thromboses (sonothrombolysis), which has been demonstrated *in vitro*, *in vivo*, and in clinical trials (Mathias et al. 2019).

Some of their most widely studied therapeutic applications have been their potential to enhance and target drug delivery to tissues. Many chemotherapy drugs suffer from high levels of systemic toxicity, resulting in significant side effects to patients when administered intravenously. Using ultrasound-sensitive particles, release of the drug can be targeted to specific locations, where ultrasound is applied, reducing systemic effects, and increasing the drug concentration in the diseased region. This has been achieved using functionalised microbubbles, in which drugs can be bound to the bubble shell, which are then released in specific locations where ultrasound is applied to fragment the bubbles as they undergo cavitation, releasing the drug (Sirsi and Borden 2014) .



As well as enabling targeted release of drugs, microbubbles have also been used as a method of enhancing the passage of drugs from the bloodstream into surrounding cells and tissues. There are several different approaches to this. One method is sonoporation, in which microbubbles can create pores in cell membranes to enable drugs to pass into them more easily (van Wamel et al. 2006). This technique has been proposed for treating conditions such as cancer and cardiovascular disease (Helfield et al. 2016; Lentacker et al. 2014). Another major technique using microbubbles to enhance drug delivery is in increasing the permeability of the blood brain barrier to drugs. This is a key focus of this thesis and is discussed in more detail in section 1.4.

#### **1.2.4 Ultrasound-sensitive particles**

While this thesis focusses on microbubbles, it is worth discussing a number of other ultrasound-sensitive particles currently under development. Many of these have similar physics to microbubbles, and so furthering our understanding of bubbles may be relevant to them.

Phase-change contrast agents (PCCA) or droplets are small packets of liquid encased within a lipid shell, which, like microbubbles, can be administered intravenously. When ultrasound is applied, however, the liquid inside the droplet vaporises in response to the reduction in ambient pressure, creating a bubble which responds to ultrasound like a microbubble. These have several advantages over microbubbles for certain applications. Because these droplets are smaller than microbubbles, many are able to extravasate, enabling seeded cavitation activity outside the vasculature (Sheeran and Dayton 2016). Because droplets are not echogenic until they vaporise, they offer a way to control the contrast signal, offering sparse and stochastic contrast, which is potentially valuable in super-resolution imaging (Zhang et al. 2018).

As well as microbubbles, numerous other ultrasound-sensitive therapeutic agents have been developed in recent years. One approach is to use liposomes to contain liquid drug solutions within

lipid shells, which fragment in response to heat generated by focussed ultrasound pulses aimed at a tumour (Lyon et al. 2018). While some ultrasound-triggered drug delivery particles are thermosensitive, most respond through cavitation.

A particularly important emerging treatment method involves acoustically active nanoparticles. One interesting example of using nanoparticles to enhance distribution of drugs is nanocups, which are bowl-shaped nanoparticles that trap a small pocket of gas inside them. Nanocups sustain cavitation activity far longer than microbubbles. They can also extravasate and enhance the distribution of drugs throughout the parenchyma due to cavitation activity (Bhatnagar et al. 2016; Kwan et al. 2015).

---

### **1.3 Physics of ultrasound-driven microbubbles**

Microbubbles exposed to ultrasound can exhibit a wide array of behaviours, including volumetric oscillations, shape changes, dissolution, fragmentation, and translational (radiation) forces. These physical phenomena are key to their utility in the applications described above.

#### **1.3.1 Physics of ultrasound**

Sound is a longitudinal wave, consisting of compressions and rarefactions, indicating regions of higher and lower pressure amplitude. Ultrasound is defined as sound with a frequency above the human hearing range (around 20 kHz), although for medical ultrasound, much higher frequencies are used, typically in the hundreds of kilohertz and megahertz range.

Ultrasound is defined in terms of several parameters. Firstly, the pressure amplitude, usually defined by the maximum negative pressure amplitude during the pulse (peak negative pressure or PNP). The negative pressure is used as this is most likely to generate cavitation events. Another important parameter is pulse duration, the length of each pulse, typically defined by the number of acoustic cycles. For imaging, this is usually very short (<10 cycles), whereas for therapy, this can be much longer (> 1,000).

Ultrasound is also defined in terms of the frequency of oscillations. Due to the time-bandwidth product, short imaging pulses contain a broad spectrum of frequencies, and so the centre frequency is usually taken as the key parameter. For long pulses, the spectrum is much more narrowband.

Finally, ultrasound is not delivered in a single pulse. In both imaging and therapy, many short pulses are delivered repeatedly over a short period. The pulse sequence is defined in terms of the Pulse repetition frequency (PRF), and the Duty Cycle, the latter defined as the proportion of time that the ultrasound is being emitted (Bushberg et al.).

---

One of the most commonly used parameters in medical ultrasound is the mechanical index (MI), a parameter based on both pressure and frequency defined as:

$$MI = \frac{PNP \text{ (MPa)}}{\sqrt{\text{Centre frequency (MHz)}}} \quad (1)$$

The mechanical index provides an indication of the mechanical effect on tissue due to the ultrasound. It is particularly used as a marker for the probability of adverse cavitation events in the tissue, which may cause biological harm. In general, the US Food and Drug Administration limits the maximum permitted MI in imaging to 1.9 (except in ophthalmic applications where the limit is much lower), so as to limit the potential for bio-effects caused by heating and cavitation (Barnett et al. 2000; Food and Drug Administration 2019; Şen et al. 2015). However, bio-effects can be generated in the tissue at a much lower MI when in the presence of contrast agents (ter Haar 2009).

Sound is reflected off boundaries between regions (such as organs) with different acoustic impedances. Acoustic impedance is defined as  $Z = \rho c$  (density x speed of sound). Sound can also scatter off particles within the tissue that are smaller than the wavelength of the sound used (such as microbubbles) (Bushberg et al.).

As sound propagates through tissue, it is attenuated exponentially. Attenuation is proportional to the frequency of the sound; higher frequencies attenuate more than low frequencies. Choice of frequency is therefore very important in medical applications. In imaging, a balance needs to be struck between penetration depth (requiring a low frequency) and spatial resolution (requiring a high frequency). In brain therapies, very low frequencies (typically < 500 kHz) are often used, as higher frequencies cannot be focussed through the skull (Yin and Hynynen 2005).

### 1.3.2 Radial oscillations of microbubbles

When a gas bubble is exposed to an oscillatory acoustic pressure wave, the increased compressibility of the gas inside compared to the surrounding liquid causes it to contract and expand in response to the wave.

The radial oscillations of a spherical bubble exposed to sound have undergone very significant theoretical investigation. By far the most common bubble model in ultrasound is the ubiquitous Rayleigh-Plesset Equation (RPE). This is used to model how the radius of a spherical bubble changes in response to an external pressure field. It assumes the pressure field is spherically symmetric around the bubble (in practice requiring the wavelength to be much larger than the bubble diameter). This equation can be derived in a number of ways, including from the Navier-Stokes equation (Apfel 1997; Leighton 1994).

To model microbubbles accurately, the Rayleigh-Plesset equation for a free bubble must be modified to account for the microbubble's shell. The most widely used modification of the RPE to describe lipid-shelled microbubble dynamics is the Marmottant model (Faez et al. 2013; Marmottant et al. 2005) :

$$\rho_l \left( R\ddot{R} + \frac{3}{2}\dot{R}^2 \right) = \left[ P_0 + \frac{2\sigma(R_0)}{R_0} \right] \left( \frac{R}{R_0} \right)^{-3\kappa} \left( 1 - \frac{3\kappa}{c} \dot{R} \right) - P_0 - \frac{2\sigma(R)}{R} - \frac{4\mu\dot{R}}{R} - \frac{4\kappa_s\dot{R}}{R^2} - P_{ac}(t) \quad (2)$$

In equation 2,  $R$  is the radius of the bubble, with over dots denoting time derivatives,  $\rho_l$  is the density of the surrounding liquid,  $P_0$  is the ambient atmospheric pressure,  $\kappa$  is the ratio of specific heats,  $c$  is the speed of sound in the liquid,  $\mu$  is the dynamic viscosity of the liquid,  $\kappa_s$  is the shell surface viscosity, and  $P_{ac}$  is the acoustic driving pressure.

This equation incorporates several different terms, describing different forces on the bubble surface, such as capillary pressure from surface tension, and viscous forces in the surrounding liquid. This particular form of the equation assumes the gas inside the bubble to be ideal; however, the

equation can be easily modified to model this as (eg) a van der Waals gas (Doinikov and Bouakaz 2011) .

The main modifications compared to the standard RPE for a free bubble are the penultimate term on the right hand side (accounting for viscous forces due to the bubble shell), and the variable surface tension parameter,  $\sigma(R)$ , given by:

$$\sigma(R) = \begin{cases} 0 & \text{if } R \leq R_{buckling} \\ \chi \left( \frac{R^2}{R_{buckling}^2} - 1 \right) & \text{if } R_{buckling} < R \leq R_{break-up} \\ \sigma_{water} & \text{if } R > R_{break-up} \end{cases} \quad (3)$$

This is shown graphically in Figure 1.2A. This arises from the nature of the single layer of phospholipids that make up the shell, which can only cover a small range of bubble surface areas. This means that at small bubble radii, the shell buckles, and at large radii, the shell (reversibly) ruptures, exposing the gas to the surrounding liquid directly, and leading to the surface tension of a gas-water interface.

This model has proven very valuable in providing significant insight into microbubble dynamics. At low acoustic driving pressures, microbubbles can oscillate linearly and stably, with the internal pressure inside the bubble being approximately equalled by the inertia of the surrounding fluid. At higher pressure, the inertial term dominates, causing highly nonlinear, high amplitude bouncing oscillations.

In particular, the model predicts a critical driving pressure above which the shelled microbubble behaves as a free bubble, and its maximum radial excursion increases very suddenly. This was confirmed experimentally in the original paper (Marmottant et al. 2005).

The nonlinear behaviour of the bubble causes the bubble's scattered sound waves to be very different to the incident wave. The Fourier transform of this signal contain harmonic frequencies of

the incident wave. The sudden collapse of the bubble, causing sharp ‘bouncing’ oscillations, can result in the emission of periodic shockwaves from the bubble (Johnston et al. 2014).

While the Rayleigh-Plesset equation has proved invaluable as a tool to predict bubble dynamics, its assumption of spherical symmetry limits the applicability of the model in a number of important scenarios, such as when the bubble is exposed to high acoustic pressure amplitudes.

Several studies have been published on modelling of microbubbles without assuming spherical symmetry, however. Accounting for non-spherical behaviour is much more important for the high acoustic pressure amplitudes used in therapy, than for imaging. A small number of studies have modified the RPE to incorporate some degree of asymmetry, for instance by incorporating surface modes described by the spherical harmonics (Versluis et al. 2010). However, these approaches are quite limited in scope, and are unable to capture the full dynamics of bubbles driven at high pressure amplitudes.

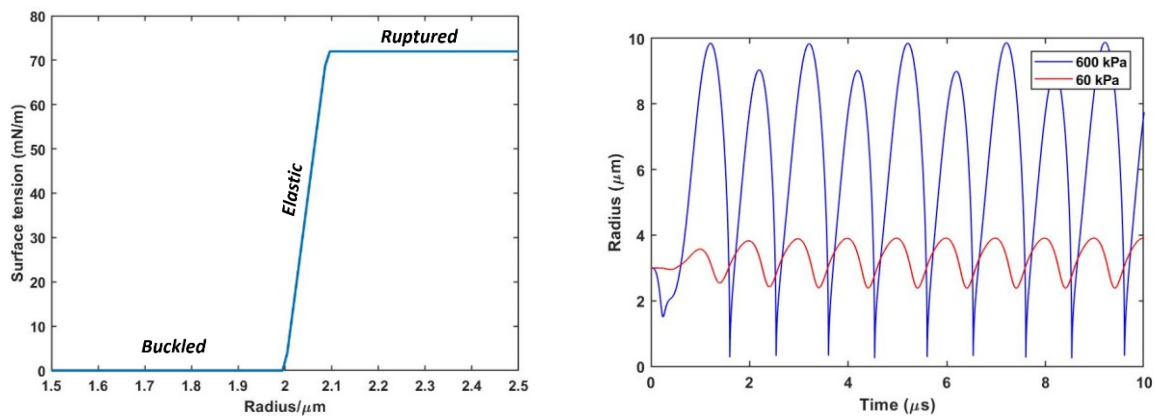


**Figure 1.2:** A) Demonstration of surface tension as a function of radius predicted by the Marmottant model for a microbubble with 2  $\mu\text{m}$  initial radius, using parameters from (Tu et al. 2009), showing buckled, elastic, and ruptured regimes. B) Radius-time curve predicted for a Sonovue microbubble from the Marmottant model for a microbubble driven with a 1 MHz ultrasound pulse at either 600 kPa (Blue) or 60 kPa (Red) PNP, at the same phase. The oscillations are approximately sinusoidal at low pressures, but become highly nonlinear at high pressures.

Modelling arbitrarily non-spherical bubbles is much more computationally intensive than using the RPE. It typically involves describing the bubble as a phase boundary and using finite element methods to solve the Navier-Stokes equation. Many approaches simplify this slightly by making simplifying assumption. By assuming the liquid to be incompressible, the Boundary Element Method can be used to solve for the location of the bubble wall, using potential flow theory, by solving the Laplace equation ( $\nabla^2 \phi = 0$ ) using boundary conditions for the bubble and vessel walls (Wang et al. 2019).

### 1.3.3 Translational motion

Not all phenomena microbubbles experience are due to volumetric oscillations, however. Microbubbles also experience translational forces when exposed to ultrasound, known as acoustic radiation forces (Dayton et al. 2002). Any material exposed to sound experiences a translational force in the direction of wave propagation. This is due to attenuation of the sound as it passes through, depositing energy. This force is the mechanism by which tissue displacements are generated in acoustic radiation force or shear wave elasticity imaging. Because of their compressibility, however, the radiation forces microbubbles experience are usually much more significant than those on bulk materials.

The force on a particle in a pressure wave is given by:

$$\mathbf{F} = -V(t)\nabla P \quad (4)$$

where  $V(t)$  is the Volume of the bubble as a function of time. Bubbles in a free fluid experience a translational force in response to an applied ultrasound field, which is non-zero when time averaged over an acoustic cycle. This is known as the primary acoustic radiation force. In the absence of attenuation, ultrasound is an oscillatory wave, meaning the time average of the gradient of the pressure wave is zero. However, because the bubble volume also changes over the cycle, the



product of these can be nonzero. The microbubble motion due to the primary radiation force is in the direction of propagation of the ultrasound wave (Dayton et al. 2002; Leighton 1994).

In addition to the primary radiation force, microbubbles close to each other also experience secondary radiation forces. This is because the microbubbles themselves emit sound waves which interact with other bubbles in the same way as the incident wave. Secondary forces between two bubbles can be either attractive or repulsive, depending on the sizes of the two bubbles (and therefore their resonance frequencies), and the frequency of the ultrasound.

In order to predict a bubble's motion, the radiation force must be solved alongside an equation of motion of the bubble. This incorporates a number of different terms including viscous drag, added mass, and the Basset or history force. A mathematical description of a spherical microbubble translating in an ultrasound pulse is given below (Dayton et al. 2002; Garbin et al. 2009):

$$0 = F_R + F_A + F_{QS} + F_H \quad (5)$$

In equation 4,  $F_R$  indicates the radiation force on the bubble,  $F_A$  is the added mass force,  $F_{QS}$  is the quasistatic drag force, and  $F_H$  is the history force. The full expression is given by:

$$0 = -\frac{4}{3}R^3 \frac{dP}{dx} - \frac{1}{2}\rho \frac{d}{dt} \left( \frac{4}{3}\pi R^3 U \right) - 6\pi\mu RU - 6\pi\sqrt{\frac{\mu\rho}{\pi}} \int_0^t \frac{d\tau}{\sqrt{\int_\tau^t R(s)^{-2} ds}} \frac{d(RU)}{d\tau} \quad (6)$$

This expression ignores the buoyancy of the bubble. In most experimental scenarios, including those in this thesis, the buoyancy force is perpendicular to the direction of ultrasound propagation. The effective mass of the bubble is taken to be the added mass term. In practice, the mass of the gas and shell will add to this, although this is very small compared to the mass of displaced liquid, and is ignored here. In many models, the history force is ignored to reduce computational time. However, experimental studies have shown that the history force can be very significant even at relatively low driving pressures (Garbin et al. 2009).

Experimental studies of the radiation force on bubbles in free fluids have shown it can cause very substantial displacements of bubbles during even quite short pulse lengths. Bubble velocities tend to be linked to bubble radius, peaking around the radius that corresponds to a resonance frequency that matches the driving frequency. The variance in bubble velocities is quite large however, even between bubbles of very similar sizes (Dayton et al. 2002).

#### **1.3.4 Effect of confinement**

The previous sections have focussed on the physics of a microbubble in a free, infinite fluid. This thesis focusses on how microbubbles interact with tissues, however, and so we must address how the presence of a boundary, or confinement of the bubble within a viscoelastic blood vessel, may affect its behaviour, as this is crucial to understand their behaviours within blood vessels (Martynov et al. 2009; Wiedemair et al. 2014).

Microbubbles expand and contract in response to ultrasound. At higher pressures, particularly those used in therapy, maximum radial excursions can be several times the initial bubble diameter. It is therefore intuitive that if a bubble is confined within a blood vessel only slightly larger than the bubble itself, its radial oscillations will be damped. This is seen experimentally in ultra-high-speed imaging of microbubbles. In a 12  $\mu\text{m}$  diameter vessel, maximum microbubble radial excursion is reduced several fold compared to its oscillations in a 200  $\mu\text{m}$  diameter vessel (Caskey et al. 2006).

In addition to a damping of oscillations, microbubbles also experience a shift in resonance frequency as a result of confinement within an elastic vessel (Jamburidze 2019), or when near a boundary.

When completely embedded in a viscoelastic material, the resonance frequency of a bubble has also been observed to increase (Jamburidze et al. 2017).

Theoretical efforts to predict the oscillations of a bubble under confinement include modifications to the Rayleigh-Plesset equation (Sassaroli and Hynynen 2005) to account for some degree of

asymmetry. For high driving pressures, it is necessary to model the bubble as an arbitrary phase boundary, allowing it to take on any shape. This can be achieved using potential flow theory, which can be solved using boundary element methods. The nature of the simulated confinement can be modified to predict bubble dynamics inside an elastic vessel (Wang et al. 2013).

### **1.3.5 Fragmentation, gas diffusion and dissolution**

Once activated, a vial of SonoVue can be used for up to 6 hours (Conversano et al. 2012). As mentioned previously, however, microbubbles have a relatively short lifespan in the bloodstream, with a half-life typically only a few minutes, even without applied ultrasound (Wu et al. 2017). This is likely due to gas dissolution (Kwan and Borden 2010b), excretion via the lungs (Tarnoki et al. 2021), and uptake of microbubbles by macrophages (Yanagisawa et al. 2007). When ultrasound is applied, however, particularly at high amplitudes, microbubbles are often destroyed very quickly. This occurs through a variety of mechanisms, which are summarised here.

While the presence of the shell, combined with the high molecular weight of the gas core, reduces the rate of gas diffusion out of the bubble, gas diffusion remains relatively significant. Applied ultrasound disrupts the bubble shell and causes diffusion of the gas over several milliseconds to seconds. This is the main mode of bubble destruction at the ultrasound parameters used in this thesis (MI 0.2-0.8), meaning that destruction of bubbles during a 10 ms pulse is unusual (Borden et al. 2005; Chomas et al. 2001a).

At slightly higher pressures, bubble fragmentation becomes a much more common mode of destruction. This is caused by microbubbles undergoing high amplitude asymmetrical oscillations. This is more common at pressures in excess of around 800 kPa, and at lower frequencies, as a longer Rarefactional phase enables larger amplitude radial excursions of the bubble. In addition to

fragmentation into smaller bubbles, it is also possible for bubbles to undergo lipid shedding, where parts of the shell break off without forming new bubbles (Borden et al. 2005; Chomas et al. 2001b; Chomas et al. 2001a).

In some instances, high amplitude asymmetric microbubble oscillations can cause the bubble to form a directional, high velocity jet of gas and shell material. This is usually associated with high pressure amplitudes and low frequencies (Cleve et al. 2019). Jetting has been associated with biological effects including sonoporation of cell membranes (Ohl et al. 2006; Postema and Gilja 2010; van Wamel et al. 2006).

Finally, a major mechanism of microbubble destruction in high concentration regions is coalescence. Because the secondary radiation force is usually attractive (especially at low ultrasound frequencies as used in therapy), microbubbles often attract each other and form clusters. The negative charge on their shells causes microbubbles to repel each other when at very close proximity, preventing coalescence at low driving pressures. At moderate to high pressures (in excess of a few hundred kPa), microbubbles often coalesce (Jamburidze 2019; Postema et al. 2004; Pouliopoulos 2017).

### **1.3.6 Other phenomena**

Microbubbles can generate a range of other effects on tissue. Microbubble oscillations can cause streaming of fluid around the bubble, causing substantial flow patterns tens of micrometres away. This has been hypothesised as a mechanism of enhancing the distribution of drugs. This is a mechanism by which physical effects on tissues can be generated without direct contact with the bubble (Collis et al. 2010). Microbubble cavitation can also cause local hyperthermia, significantly enhancing the heating effect of the ultrasound (Kaneko et al. 2005; Yu et al. 2004; Yu et al. 2006).

---

## **1.4 Blood-brain barrier opening**

As mentioned above, BBB opening using ultrasound and microbubbles is a valuable tool to enhance the passage of therapeutic agents from the blood to the brain parenchyma. This thesis is concerned with the fundamentals of how microbubbles interact with tissue, and potential mechanisms of therapeutic effects, with a focus on blood-brain barrier opening. This section describes in detail our current understanding of BBB opening. It covers, in sequence, the biology of the BBB, why approaches to deliver drugs across the BBB are needed, current methods used clinically and under development to deliver drugs through the BBB, and then looks at our existing experimental and theoretical understanding of how microbubbles may interact with brain tissue.

### **1.4.1 Structure of the blood-brain barrier**

The brain is supplied with blood via a dense network of vessels, ranging from mm-diameter arteries and veins, down to the microvasculature, consisting of venules, arterioles, and capillaries. Most exchange of substances occurs in the microvessels, especially the capillaries. While larger vessels have several layers of tissue surrounding their lumens, capillaries are much thinner, consisting of a single layer of endothelial cells, supported by a basement membrane of extracellular matrix. No brain cell is further than about 25  $\mu\text{m}$  from a capillary (Abbott et al. 2010), and a typical neuronal cell body is around 10  $\mu\text{m}$  from its nearest capillary (Abbott et al. 2006).

Many capillaries elsewhere in the body are either fenestrated or discontinuous. Fenestrated capillaries contain pores around 60–80 nm in diameter, often with a diaphragm that allows small molecules and some proteins to diffuse through. They are typically found in the digestive and endocrine systems, and within the kidney. Discontinuous capillaries have much larger openings, which allow even red blood cells to pass through. They are found primarily in the liver, bone marrow and spleen (Bennett et al. 1959).

Capillaries in the nervous system, muscles, and skin are continuous, with tight junctions between endothelial cells forming a continuous barrier, and lacking openings for molecules to diffuse through directly. Outside of the nervous system, vascular endothelial cells have many transport vesicles, which allow a wide array of molecules to pass through. Within the central nervous system however, transportation is far more selective (Abbott et al. 2010).

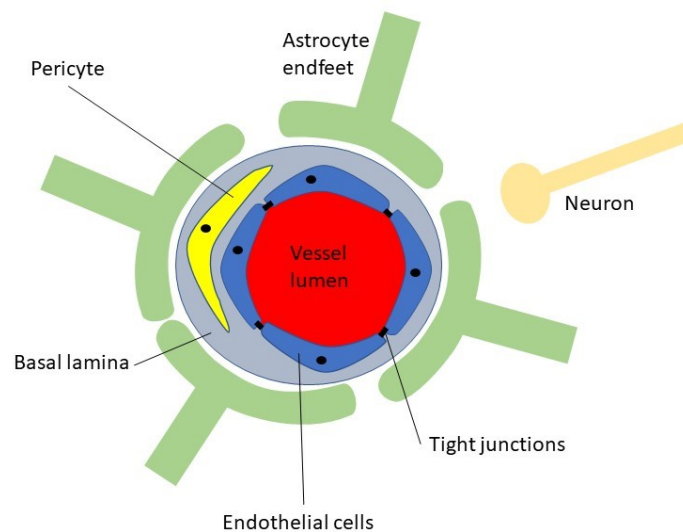


Figure 1.3: Cross-sectional view of the neurovascular unit.

The combination of characteristics, including tight junctions between cells, limiting the paracellular transport of molecules, and reduced density of transport vesicles, limiting transcellular pathways, place tight restrictions on the movement of substances from the vasculature to the brain parenchyma, forming what is known as the blood brain barrier (BBB). The BBB is present across the vast majority of the vasculature supplying the brain, except for those supplying the circumventricular organs such as the pineal gland. Blood vessels supplying the spinal cord also have similar properties, and form the Blood-Spinal Cord Barrier (BSCB) (Abbott et al. 2010; Bartanusz et al. 2011).

The BBB is important in maintaining homeostasis within the brain. Changes in the concentration of molecules in the blood, particularly ions or molecules that can act as neurotransmitters, could cause

unwanted changes to the activity of neurons if these changes were allowed to directly impact the extracellular fluids within the brain. The BBB also protects the brain from pathogens (Abbott et al. 2006; Cabezas et al. 2014).

The blood-brain barrier is based around the neurovascular unit, which is a combination of cells and structures that form the blood vessels of the brain. Around the lumen of a microvessel, the single layer of endothelial cells are joined together by a network of tight junctions. Tight junctions are transmembrane proteins (typically integrins and occludins) that bind the membranes of cells together. There are also Adherens junctions which bind adjacent cells by their cytoskeletons. In the brain, these junctions form an impermeable barrier between cells, ensuring that molecular transport happens only through cells. Surrounding the endothelial cell layer is the basement membrane: layers of extracellular matrix composed of the basal and reticular laminae. This helps to give the vessel its structure. Within the basement membrane are pericytes: cells which envelop the vessel. Finally, the outer surface of the vessel is covered with astrocyte endfeet (Hawkins and Davis 2005; Iadecola 2017).

Astrocytes are a common type of glial cell present throughout the whole of the central nervous system. They typically have many long processes extending from their cell body, deep into the surrounding brain tissue. These processes have endfeet that surround blood vessels, as well as synapses between neurones, providing a link between the vasculature and neuronal activity. They can secrete or absorb neurotransmitters or gliotransmitters at synapses, affecting neuronal signalling. Astrocyte membranes contain various ion channels, which make the cells electrically excitable (although, unlike neurons, they do not generate action potentials). They primarily signal through intracellular calcium waves (Scemes and Guame 2006).

Astrocyte-blood vessel interactions play a key role in many important biological phenomena.

Astrocytes can respond to mechanical stimuli applied to blood vessels by changing their transmembrane potential, or by stimulating calcium waves. Astrocytes also play a role in regulating

blood flow by secreting molecular mediators that cause vessel constriction or relaxation (Gordon et al. 2007).

Both astrocytes and pericytes have also been shown to play a key role in generating the blood brain barrier and in modulating its permeability. The BBB is not a static barrier, and its permeability can change depending on different conditions. Opening of tight junctions in the brain can occur in inflammation. For instance, expression of transmembrane transport proteins such as GLUT1 is increased in starvation and hypoxia (Abbott 2002; Abbott et al. 2006).

#### **1.2.4 Blood brain barrier permeabilisation**

This thesis has a particular focus on a novel application of ultrasound and microbubbles to treat brain diseases. Passage of molecules from the blood to the brain is significantly restricted by the Blood-Brain Barrier, which significantly impedes the movement of nonessential substances into the brain parenchyma, and is necessary to maintain homeostasis and protect neurones, which are highly sensitive to their external environment.

The Blood brain barrier is a major impediment to pharmacologic treatment of brain disorders. In most organs, capillaries are relatively permeable, meaning drugs administered systemically will usually diffuse or be transported from the bloodstream into body tissues. Passage of molecules into brain tissue, however, is very tightly restricted by the dense network of tight junctions between vascular endothelial cells, highly selective intracellular transport systems, and well developed efflux systems to remove unwanted molecules from the brain parenchyma (Abbott et al. 2010; Ballabh et al. 2004).

Drugs that pass well through the blood-brain barrier tend to have a combination of low molecular weight (<approx. 400 Da) and lipophilicity (non-polar), the latter enabling them to diffuse freely



through the lipid membranes of endothelial cells. Very highly lipophilic molecules have lower uptake however, due to increased plasma protein binding (Waterhouse 2003) .

These characteristics place very severe constraints on the design of drugs intended to treat brain diseases. Many modern therapeutics for example increasingly come in the form of large proteins or nucleic acid polymers.

This inability to efficiently transport novel drug molecules into the brain has had a severe impact on the treatment of many brain diseases. Glioblastoma multiforme is one of the most aggressive and common types of brain cancer. One of the few drug treatments for glioblastoma is temozolomide; however, because of the blood-brain barrier, the concentration of the drug in the brain is typically less than 20% of that in the blood (Karmur et al. 2020). While many diseases are associated with BBB degradation, such as glioblastomas and Alzheimer's, this is usually only partial, and is often not significant in regions most in need of treatment. In glioblastoma, the outer parts of the tumour that infiltrate healthy tissues usually have an intact BBB, meaning that, while drug therapies may reach some parts of the tumour, they cannot halt the disease's progress (Sarkaria et al. 2018).

Many methods to overcome the BBB have been proposed, and several are in clinical use. A simple, but invasive technique is direct injection into the brain, either via a single or repeat bolus, or through an implantable device, such as an Ommaya Reservoir, which allows for repeat doses without additional surgery. Drugs can be injected into the parenchyma, or the CSF. While CSF injection bypasses the BBB, diffusion of drugs from the CSF into the brain tissue is often slow and provides quite poor distribution (Patel et al. 2009). Convection-enhanced delivery (CED) is an alternative method of direct injection into the interstitial spaces of the brain. In CED, continuous pressure is applied to the fluid to force it further into the tissue, rather than relying solely on diffusion as is the case in a single bolus (Hunt Bobo et al. 1994).

These approaches require major neurosurgery, especially in deep-lying tumours, and are therefore associated with a risk of complications. Injection into the brain is also difficult to optimise to achieve

good distribution into the most important regions. Many of these techniques, including CED, have been tested clinically, but results in clinical trials have not generally been promising (Mehta et al. 2017).

Intravascular administration of mannitol (usually via the carotid artery) can temporarily disrupt the blood brain barrier. Mannitol is hyperosmolar, and so its presence in the brain vasculature draws water out of the brain's endothelial cells. This causes the cells to shrink slightly, placing pressure on the tight junctions, and temporarily opening up the barrier. This has been shown to be clinically feasible, and can improve outcomes for patients with certain conditions, such as primary central nervous system lymphoma (Angelov et al. 2009; Kuitunen et al. 2017). However, this method opens the blood brain barrier across the whole brain, which may be undesirable if the aim is to deliver particularly toxic chemotherapeutic drugs to a small lesion.

Another major approach to deliver drugs to the brain is to utilise endogenous receptor-mediated transport systems. This can be achieved in several different ways. One method, currently undergoing clinical trials for several diseases, is a type of immunotherapy based on Chimeric Antigen Receptor (CAR) T-Cells. The patient's own T-cells are modified to target an antigen expressed by the cancerous cells. Because T-cells are naturally transported across the BBB, these have the ability to directly treat brain diseases. CAR T-cells are not currently widely used as their clinical efficacy is unclear however. There is also evidence of neurotoxicity in many patients, likely arising from the induced immune response (Gust et al. 2017).

Delivering drug molecules has also been achieved using Carrier-Mediated Transport ('Trojan Horse' techniques), in which a drug is modified to piggy-back on an existing molecular transport pathway. The glucose transport receptor GLUT1, for instance, has been utilised to transport modified small molecule therapeutics into the brain (Patching 2017; Patel and Patel 2017).

Many of these approaches, however, require modifications of the drugs themselves, limiting the breadth of potential applications. They also cannot be well targeted to particular brain regions,

delivering the drug to large parts of the brain. There are significant limitations on drug properties and sizes that can be used; it is not possible for large proteins to share the same transport systems as single glucose molecules, for example (Patel and Patel 2017).

### **Focussed ultrasound and microbubble-induced Blood-Brain Barrier opening**

Blood-brain barrier opening using high intensity focussed ultrasound alone is possible, but has many significant problems with safety and reliability (Vykhodtseva et al. 1995). The first demonstration of the feasibility of blood brain barrier opening using ultrasound-driven microbubbles was published in 2001. In this study, extravasation of an MRI contrast agent into the brain parenchyma of rabbits was reliably achieved at relatively low ultrasound intensities, with no apparent safety concerns (Hynynen et al. 2001).

Ultrasound and microbubble technology has several key advantages over those mentioned above. Firstly, it can be very minimally invasive, requiring only an intravenous injection of microbubbles (although several techniques involve surgical implantation of ultrasound transducers (Carpentier et al. 2016; Idbaih et al. 2019)). It can also be targeted to specific regions, meaning disruption and drug delivery to healthy tissues can be limited. Finally, the opening is reversible, with the barrier closing again over a period of minutes to hours (Morse et al. 2019).

Since the technique was first proposed, a great deal of research has been performed into its refinement, application in different scenarios, and recently in its clinical translation. BBB permeabilisation using MR-guided focused ultrasound and microbubbles has been used in clinical trials in a wide range of diseases, including amyotrophic lateral sclerosis (ALS) (Abrahao et al. 2019), Alzheimer's disease (Lipsman et al. 2018), and glioma (Mainprize et al. 2019).

In clinical trials, pulses are typically 2-10 milisecond long, at a repetition frequency of approximately 1 Hz, and a centre frequency of 1 MHz or below. Peak negative pressures are typically moderate,

---

usually below 1 MPa (Carpentier et al. 2016; Idbaih et al. 2019; Lipsman et al. 2018). In rodents, BBB opening can be achieved at pressures of tens to a few hundred kPa (Burgess et al. 2012; Raymond et al. 2007). Pressures in human clinical trials are often not reported, as it is difficult to estimate accurate pressures within the brain, due to attenuation by the skull. Many trials use an acoustic feedback system, meaning the actual pressure output from the transducers can vary significantly between patients with varying skull thicknesses and shapes (O'Reilly and Hynynen 2012).

Further details on the biology of the blood-brain barrier, and proposed mechanisms of BBB opening, are covered in §1.4.2 and 1.4.3.

#### **1.4.2 Physical mechanisms of blood-brain barrier opening**

The physical behaviours of microbubbles described in §1.3 can have a number of different impacts on their surrounding environment. Volumetric oscillations can cause stresses on vessels, distending and invaginating them. Radiation forces on bubbles can also deform soft tissues. Microbubbles can also induce streaming of surrounding fluids, which can improve the distribution of drugs in the tissue.

Several different methods have been used to investigate potential physical effects of microbubbles on tissues. Using large, dilute populations of microbubbles exposed to long duration ultrasound pulses, displacements of several microns can be generated in soft tissue mimicking materials due to the primary radiation force. While the bulk mechanical properties are quite similar, the micron-scale structures are extremely different (Koruk et al. 2015; Saharkhiz et al. 2018).

While much theoretical work has been conducted, alongside controlled experimental observations of bubbles in free fluids or phantom environments, published experimental observations of microbubble forces exerted on real *in vivo* or *ex vivo* tissues has been quite limited, although several important studies have provided insight into specific phenomena.

Microbubble interactions with tissues have been observed experimentally *in vitro*. Microbubble interactions with *in vitro* thromboses have been directly observed, which have illustrated potential mechanisms of sonothrombolysis. When ultrasound is applied to bubbles within the thrombus, deformations and pits are generated both via inertial cavitation and acoustic radiation force (Chen et al. 2014). Significant research has been performed on microbubble interactions with layers of cultured endothelial cells. Using ultra high speed microscopy (>10 Mfps), microbubbles have been observed to create pores in cells (Prentice et al. 2005), which allow drugs inside (Helfield et al. 2016).

A small number of studies have been performed using *ex vivo* tissue samples where bubbles can be observed within the vasculature directly. Microbubbles have been observed within rat caecum and mesenteric microvessels. Confinement within microvessels significantly reduces the maximum radial excursion of microbubbles exposed to ultrasound, when compared to their dynamics in an infinite fluid (Caskey et al. 2007). When exposed to high amplitude (>1 MPa PNP), short pulse ultrasound, microbubbles within microvessels can generate significant local distention and invagination of nearby walls of blood vessels. Under these parameters, bubbles can experience shape changes, including jetting, where one side of the bubble collapses into the other, forming an intense fluid jet (Chen et al. 2011; Chen et al. 2012).

The direct optical observations of microbubbles interacting with tissues that are described here have so far only been achieved in either isolated thromboses or cell cultures, or within *in vivo* or *in vitro* mesentery or caecum, where small vessels can be easily identified among thin transparent tissues, enabling simpler optical observation. These scenarios offer limited relevance to most therapeutic applications of bubbles however, where their effects are deep within organ tissues. In particular, the dynamics of bubbles within brain tissue when exposed to ultrasound pulses typically used in blood brain barrier opening have never previously been observed.

### **1.4.3 Biological mechanisms of blood-brain barrier opening**

This section summarises our current understanding of how physical effects induced by bubbles on the vasculature can potentially generate biological responses, such as BBB opening.

Many of these mechanisms by which therapeutic effects are generated have not yet been fully elucidated. However, it appears likely that mechanical stresses exerted on tissues through the physical mechanisms outlined in the previous section, generate biological effects resulting in the opening of the BBB in a region local to the bubble. The biological nature of BBB opening has been investigated experimentally in a variety of ways.

One of the most important categories of experiment has been intravital multiphoton fluorescence microscopy. In these studies, the animal is injected with a fluorescent dye alongside the microbubbles, and the vessels of the brain are directly imaged during the sonication. In some instances this can even be achieved without removing part of the skull. This technique enables direct observations of the dye in real time, relatively deep (up to 100  $\mu\text{m}$  or so) below the brain surface.

There are several different types of opening observed. Fast, in which the vessel is opened immediately, with large volumes of dye leaking out, but reducing exponentially from the time of treatment. And slow, in which extravasation happens gradually over many seconds to minutes (Burgess et al. 2014; Burgess et al. 2015; Nhan et al. 2013; Raymond et al. 2007).

Real time observations of vessel movement and constriction can be observed, showing that vasoconstriction in response to the applied ultrasound is a common phenomenon in vessels such as arterioles. However, because fluorescence is required to image at such high penetration depths, this technique cannot image the microbubbles themselves, and is limited to quite low frame rates. It is therefore not possible to correlate extravasation of the dye with microbubble dynamics using this technique.

It was often assumed that mechanical stretching of tight junctions was the primary mechanism of BBB opening. This was based on observations of disruption of tight junctions in sections of treated tissue (Sheikov et al. 2008). Expression of the tight junction proteins ZO-1, occludin and claudin-5 is significantly reduced after treatment (Zhao et al. 2018). Studies on *In vitro* BBB models have shown that stretching of the cells can open the BBB through disrupting the basement membrane and tight junctions (Partyka et al. 2017).

However, there is growing evidence to suggest that BBB opening, at least at low pressures, is also an evoked response, and is significantly mediated through transcytosis, via the transcellular pathway, and not just through tight junction disruption, which opens up the paracellular pathway.

From histological examination of brain tissues acquired from rodents treated with ultrasound and microbubbles, it has been observed that brain arterioles show an increase in their numbers of transport vesicles in response to focussed ultrasound BBB opening (Sheikov et al. 2006). This is associated with increased expression of Caveolin-1, a protein required for the formation of caveolae, invaginations in the cell membrane that transport molecules in and out of the cell via vesicles (Deng et al. 2012). A recent paper using knockout mice that do not express caveolin-1 also showed the essential role of caveolin-mediated transcytosis in safe BBB opening, especially for large (> 500 Da) molecules (Pandit et al. 2020).

Aside from observations specific to BBB opening, many significant effects on cells due to microbubbles have been observed. These are mostly investigating sonoporation, but it is very plausible that some of the mechanisms induced in the endothelial cells could be similar.

Microbubbles have been shown to generate calcium transients and reactive oxygen species in cell cultures. ROS act as messengers in several key cellular pathways, but are associated with organelle and DNA damage at high concentrations (Jia et al. 2018; Kooiman et al. 2013).

---

#### 1.4.4 Ultrasound parameters used for therapy

The ultrasound parameters used in ultrasound therapy need to be carefully optimised to achieve the particular effects desired. For instance, in therapies involving thermal ablation using HIFU, very long, relatively high amplitude, high frequency pulses are used. This minimises thermal dissipation, ensuring maximum attenuation and energy deposition into the tissue. In histotripsy on the other hand, where cavitation is the primary mechanism of destruction, extremely high amplitude (>30 MPa), but very short ( $\mu$ s) pulses are used. This generates significant cavitation events, but the long periods between short pulses ensure enough time for heat to dissipate, avoiding heating of the tissues.

For blood-brain barrier permeabilization using microbubbles, it is important to ensure safe microbubble behaviours to generate the largest degree of opening for the smallest amount of damage. Determining safe parameters in animal studies has typically been achieved empirically, by testing a range of pressures and pulse lengths and observing the results. These parameter choices are therefore not based on a detailed knowledge of what particular bubble behaviours must be generated, because the precise mechanisms of BBB opening are unclear.

There are several different parameters that must be considered in any study, including centre frequency, pulse length, pulse repetition frequency, peak negative pressure, microbubble concentration, and microbubble type and composition.

Animal studies typically use centre frequencies of around 1 MHz, with pressure amplitudes around 0.2-1 MPa, and tone pulses typically around 2 – 10 ms in length. Pulse repetition frequencies are usually in the Hz range. Some studies have been successfully performed using short pulses (a few cycles); the results have been variable in comparison to the tone pulses (Choi et al. 2011; McMahon et al. 2020; Morse et al. 2019). Many recent *in vivo* studies use intravenous microbubble injections that achieve a similar serum concentration in the animals as the clinical concentration used in imaging and therapy.



In clinical trials involving transcranial ultrasound, lower frequencies must be used in order to pass through the skull, typically around 300 kHz. Implantable devices can use higher frequencies such as 1 MHz, which is similar to frequencies used in animals.

In transcranial ultrasound therapy, it is difficult to calibrate exact pressures within the brain due to unpredictable attenuation through the skull. In many clinical trials of transcranial ultrasound, a pressure ramping approach is used. The pressure is gradually increased until subharmonics are detected above a particular threshold. The pressure amplitude is then halved, and this final value is used for the rest of the treatment. This means that the particular pressure values experienced by the bubbles in many clinical trials is unknown (Jones and Hynynen 2019).

---

## **1.5 Aims and scope of this thesis**

This thesis aims to provide insight into the nature of interactions between microbubbles and soft tissues. The principal focus is on physical interactions, such as tissue displacement, vessel distension and vessel rupture. These experimental results aim to enhance our understanding of the underlying mechanisms of how microbubbles achieve therapeutic effects, and help identify a safe range of behaviours, and when they may be likely to cause damage. The thesis has a particular focus on blood brain barrier permeabilization, and this has determined the choice of tissue models and ultrasound parameters.

Microbubbles are directly observed under sonication *in situ* using high speed microscopy. In Chapter 2, they are investigated in tissue-mimicking hydrogels with similar mechanical properties to soft tissues. In Chapter 3, these experiments are transferred to an *ex vivo* setting to observe microbubbles in brain microvessels. Finally, in Chapter 4, the phenomena observed in Chapter 3 are investigated in more detail, to provide greater context for their potential significance in an *in vivo* setting.

The experiments in soft tissue-mimicking materials are used to investigate the primary radiation force bubbles exert on tissue. This is measured by tracking microbubbles as they reversibly penetrate into the gel. This approach offers a way to observe microbubble dynamics in a controlled environment, enabling trends with bubble size and ultrasound parameters to be elucidated while controlling for other variables.

The second part of the thesis transfers this to a real tissue setting. *Ex vivo* acute brain slices are chosen because they are highly relevant to BBB opening, and are relatively transparent, enabling clear images of bubbles within blood vessels to be obtained. This setting offers two key improvements on previous studies investigating microbubbles in real tissue. Firstly, microbubbles are observed in living brain tissue, not in caecum or mesentery. Secondly, typical BBB opening pulses

are used, and observed at high frame rates over at least 15 acoustic cycles, not just a few frames of a single high amplitude pulse.

Together, these experimental results help to explain what forces microbubbles exert on their surroundings during ultrasound therapy, and provide greater depth to our understanding of mechanisms of ultrasound therapies. This knowledge aims to help in the future to optimise particular bubble behaviours to ensure the safest and most efficacious therapies can be achieved in the clinic.

## **Chapter 2: Microbubble-induced elastic deformation of soft tissue mimicking materials using the primary radiation force**

### **2.1 Introduction**

The overall aim of this thesis is to investigate the response of tissues to microbubble-induced forces. This chapter focusses on understanding the mechanical effects that microbubbles have on tissue due to the primary radiation force, by observing bubble motion under controlled conditions in tissue-mimicking materials. The principal value of this is to improve our understanding of the mechanisms of microbubble therapies, which may inform ways to optimise them. This chapter also has a secondary aim of investigating the feasibility of using microbubble indentation due to the primary radiation force as a method of remote soft material characterisation on very small spatial and temporal scales.

As described in detail in Chapter 1, most of the biologically relevant effects that microbubbles are believed to have on tissue are due to mechanical stimulation of vascular endothelial cells, blood vessels, and surrounding tissues (Roovers et al. 2019). There are several different ways that microbubbles are able to exert forces on tissue, with some of the most important being volumetric oscillations, and radiation forces. Much previous work on microbubble-induced forces has focussed primarily on forces exerted via volumetric oscillations of microbubbles. For instance, microbubble expansion and contraction has been shown to deform the walls of blood vessels when exposed to high amplitude, short ultrasound pulses (Caskey et al. 2007; Chen et al. 2011; Chen et al. 2012).

Microbubbles exposed to ultrasound also experience a translational force, typically in the direction of sound propagation, known as the primary radiation force (Dayton et al. 2002; Leighton 1994). The primary radiation force on microbubbles has previously received theoretical and experimental attention, having been shown to displace bubbles in a free fluid by significant distances during

typical imaging pulses (Blue et al. 2018; Dayton et al. 2002), and to bring bubbles towards a boundary, as a way of enhancing the contrast of molecular imaging with ligand-targeted microbubbles (Frinking et al. 2012; Lum et al. 2006; Shortencarier et al. 2004).

Some research has also investigated how the radiation force on bubbles can impact soft materials with which the bubble is in contact, although this has been more limited. Many studies have been performed on large (tens of micrometres to millimetres in diameter) laser-induced bubbles embedded in a medium. This has been proposed as a method to estimate material mechanical properties, especially of very superficial tissues such as the cornea (Erpelding et al. 2005; Ilinskii et al. 2005; Shirota and Ando 2015; Yoon et al. 2011).

Some experimental attention has also previously been given to the effects that contrast agent microbubbles at interfaces driven by acoustic radiation forces may have on tissue. Radiation forces due to ultrasound have been shown to cause microbubbles to tunnel into agarose at pressures over 1.2 MPa at 1 MHz (Caskey et al. 2009). Using large, concentrated clouds of contrast agent microbubbles, the primary radiation force has been shown to reversibly deform soft gels (Koruk et al. 2015; Saharkhiz et al. 2018).

While these studies provide insight into general physical principles, there is a need to investigate how a single microbubble affects tissue under clinically relevant ultrasound parameters. The dynamics of a shelled microbubble are likely to be different to those of a much larger unshelled bubble. Studies of clouds of bubbles are also limited, as many of the most important effects of bubbles are in microvessels, where bubbles are well separated. There is also a need to understand physical forces on a micrometre scale experienced by individual cells, rather than millimetre scales.

This chapter focusses on the how a microbubble exposed to ultrasound physically interacts with its surroundings. The bulk of this chapter focusses on experimental results of how a microbubble can indent a soft material due to the primary radiation force. This is analysed with a mathematical model to demonstrate the potential of this technique to measure mechanical properties of tissues.

### Bubble-boundary interactions

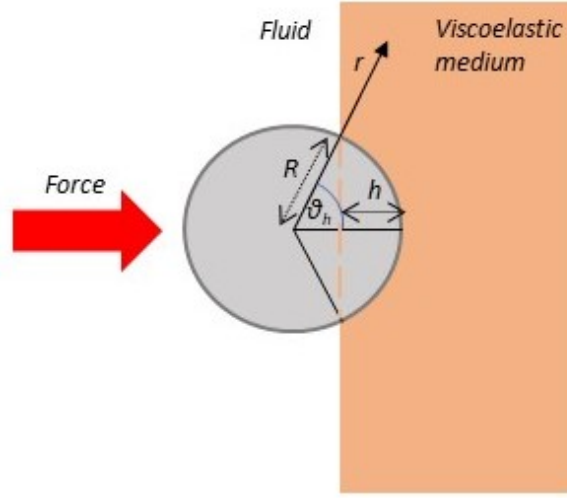


**Figure 2.1:** Schematic of the bubble indentation model used illustrating the impact of a bubble into a viscoelastic material

In order to investigate the interaction between a bubble and a viscoelastic medium quantitatively, this study uses a mathematical model to analyse the indentation curves of bubbles. This aims to allow estimation of parameters from experimental results, producing quantitative estimates of the radiation force on a microbubble, and determining an empirical description of bubble behaviour.

There are several ways an object, such as a bubble, impacting a soft boundary can be modelled. A very common and well-established model of a parabolic object non-adhesively impacting an elastic medium is the Hertz model. For a solid sphere of radius  $R$  indenting a distance  $\delta$  into a planar elastic medium with Young's Modulus  $E$  and Poisson's ratio  $\nu$ , the time averaged force is given as (Zhu et al. 2016) :

$$F = \frac{4\sqrt{R}}{3(1-\nu^2)} E \delta^{\frac{3}{2}} \quad (7)$$

The mechanical properties of the medium impacted by the bubble must be described mathematically. In the basic form of the Hertz model, the material is purely elastic and linear. The

Hertz model also assumes the surface area of contact is small. It is thus inaccurate in predicting large indentations

Hydrogels, like soft tissues, also have viscous properties. They can therefore be modelled as viscoelastic materials in terms of two principal parameters: the Young or Shear modulus and dynamic (or kinematic) viscosity. Viscoelasticity can be modelled in several ways. One of the most common models of viscoelasticity is the Kelvin-Voigt model. It describes a material mathematically in terms of a purely elastic spring in parallel with a purely dissipative viscous damper. The Hertz model can be modified to incorporate viscoelastic models of materials, and account for the viscosity of the medium, as well as its elasticity.

The model chosen for this study is a fully viscoelastic model. It is based on a previous model of a bubble completely embedded in a viscoelastic material, which is applicable for a large surface area of contact between the bubble and the boundary, and a specific boundary condition for a bubble-tissue interface (Ilinskii et al. 2005). The full derivation of the model is given in previous published works (Ilinskii et al. 2005; Koruk and Choi 2018; Koruk and Choi 2019) and is summarised here.

The model of displacement of a bubble into a medium is ultimately based on a form of the Navier-Stokes equation, incorporating the shear modulus,  $G$ , of the material :

$$-\nabla P + G\nabla^2 \mathbf{u} + \mu \nabla^2 \frac{\partial \mathbf{u}}{\partial t} = \rho \frac{\partial^2 \mathbf{u}}{\partial t^2} \quad (8)$$

where  $P$  is the pressure,  $u$  is displacement,  $\mu$  is dynamic viscosity and  $\rho$  is the density of the medium. Assuming an incompressible, homogeneous, medium, this gives the following :

$$\nabla \cdot \mathbf{u} = 0 \quad (9)$$

$$\mu \nabla^2 \mathbf{u} = \nabla P \quad (10)$$

These can be rewritten as:

$$\mathbf{u} = \nabla \times \nabla (g\mathbf{e}) \quad (11)$$

where  $\mathbf{e}$  is a unit vector in the direction of the displacement. For a purely elastic medium, experiencing dynamic loading due to an external impulse,  $g$  is a scalar function defined as:

$$g(r) = ar \frac{ae^{ikr}}{ikr} - \frac{b}{r} \quad (12)$$

$a$  and  $b$  are complex constants determined by the system's specific boundary conditions,  $k$  is a wavenumber for a shear wave of frequency  $k^2 = \rho\omega^2/G$ , and  $i$  is the imaginary unit. The pressure in the medium is defined as :

$$p = p_0 + G(\mathbf{e} \cdot \nabla)(\nabla^2 g + k^2 g) \quad (13)$$

The pressure term incorporates the external force given by:

$$f = -2\pi R^2 \int_0^{\theta_h} (-p \cos\theta + \sigma_{rr} \cos\theta - \sigma_{r\theta} \sin\theta) \sin\theta d\theta \quad (14)$$

where the force is integrated from 0 to the angle of contact at depth  $h$ . The boundary conditions are  $\sigma_{rr} = p_e - p_g$  and  $\sigma_{r\theta} = 0$  at the bubble-material boundary.  $p_e$  is the external pressure from acoustic radiation, and  $p_g$  is the internal gas pressure. Using expressions for the components of the shear modulus in terms of  $g$  and  $k$ , equations 12 and 13 can be used to generate an expression relating the force applied to the displacement of the bubble. In the frequency domain, the applied force is given by :

$$F_\omega = 2\pi GRU_\omega(1 - \cos^3\theta_h) \cdot \left(1 - ikR - \frac{1}{6}k^2R^2 + \frac{1}{18}ik^3R^3\right) \quad (15)$$

Viscoelasticity can be accounted for by replacing the shear modulus  $G$  with a complex shear modulus  $G - i\mu\omega$ , which incorporates the viscosity,  $\mu$  of the medium. Via inverse Fourier transform, the final expression for displacement,  $u$ , of a bubble of radius  $R$  at a viscoelastic interface (Figure 2.1), exposed to an external force with an amplitude  $f_0$  and duration  $\tau$  is given (in the time domain) by (Koruk and Choi 2018; Koruk and Choi 2019):



$$u = -\frac{if_0}{6\pi R\left[1-\left(1-\frac{u}{R}\right)^3\right]}\mathcal{F}^{-1}\left[\frac{(e^{i\omega\tau}-1)(3-ikR)}{\omega(G-i\mu\omega)\left(1-ikR-\frac{1}{6}k^2R^2+\frac{1}{18}ik^3R^3\right)}\right] \quad (16)$$

where  $k = \omega/\sqrt{(G/\rho)(1 - i\omega\mu/G)}$  is the wave number of the shear wave with frequency  $\omega$  and  $\mathcal{F}^{-1}$  represents the inverse Fourier transform. The shear modulus,  $G$  is related to the Young's modulus,  $E$ , by  $G = E/2(1 + \nu)$ , where  $\nu$  is the Poisson's ratio, taken as 0.45 for the gels (Engler et al. 2004; Frey et al. 2007). Here, the excitation duration  $\tau$  was divided into  $N$  points (e.g., 1000) and the calculations were repeated over the entire time period of interest using Matlab (MathWorks, MA, USA). The inverse Fourier transform generates four roots, of which one was chosen based on which solution is physically plausible (correct boundary conditions, with gradual indentation into the gel in direction of ultrasound propagation).

This model can account for a large surface area of contact, and uses specific boundary conditions for a bubble interface. The model still assumes linear elasticity, however, meaning it can only accurately account for relatively small indentation depths. It also does not account for surface tension or bubble radial oscillations.

For the above models, it is important to note that the maximum indentation depth is determined by the elasticity (and is independent of viscosity), and the rate of increase and relaxation is determined by the ratio of viscosity to elasticity. The behaviour of the model with different input parameters, chosen to be typical for a Sonovue microbubble during therapy, are shown in Figure 2.1.

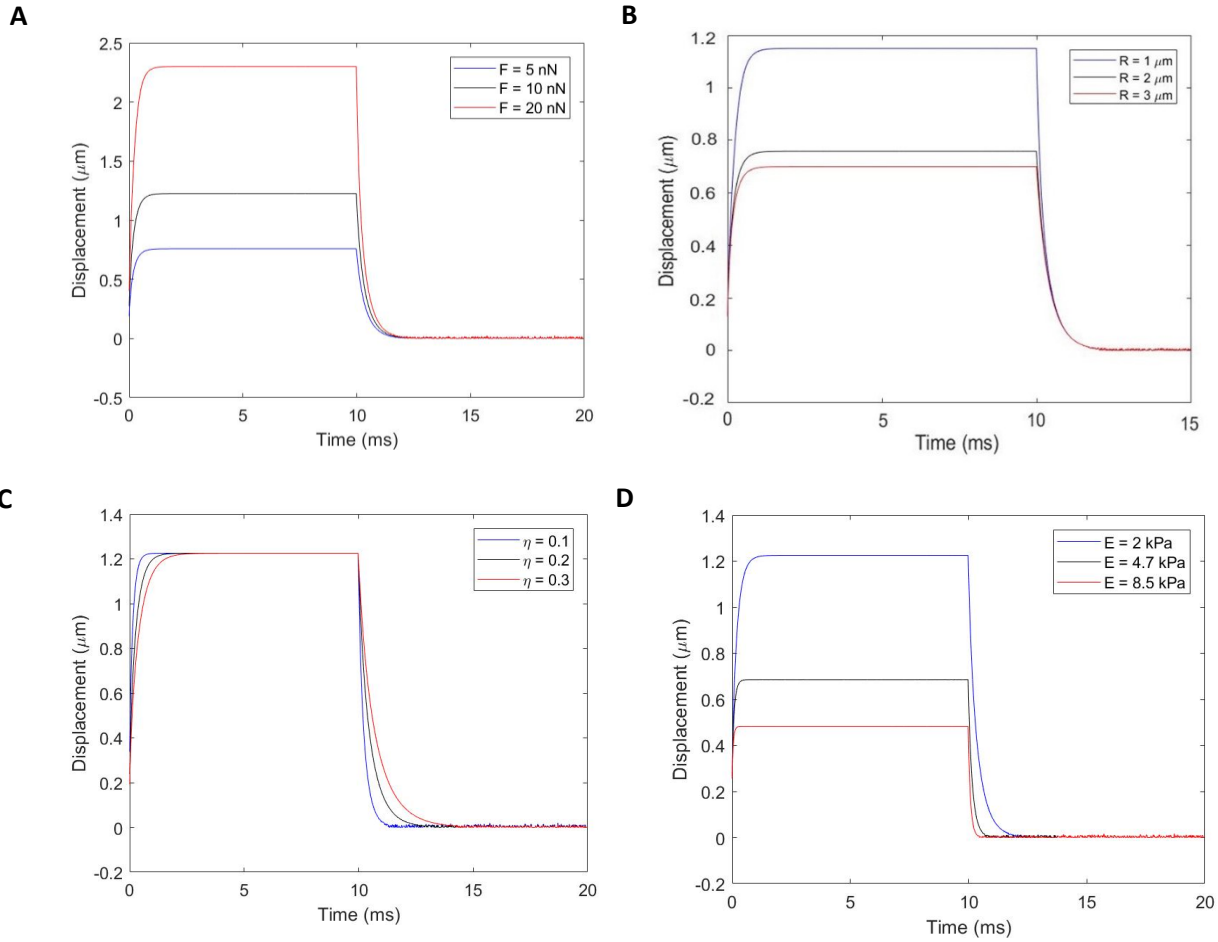


**Figure 2.2:** Model predictions of bubble indentation for a variety of parameters during exposure to a 10 ms continuous ultrasound pulse. A) Indentation of a  $2\text{ }\mu\text{m}$  radius bubble indenting into a  $2\text{ kPa}$ ,  $0.15\text{ Pa s}$  gel at three different force values. B) Indentation of three different bubble radii indenting into a  $2\text{ kPa}$ ,  $0.15\text{ Pa s}$  gel exposed to a radiation force of  $5\text{ nN}$ . C) Indentation of a  $2\text{ }\mu\text{m}$  radius bubble exposed to a  $10\text{ nN}$  force indenting into a  $2\text{ kPa}$  gel, with varying viscosity values. D) Indentation of a  $2\text{ }\mu\text{m}$  radius bubble exposed to a  $10\text{ nN}$  force indenting into gels with Young's Moduli of  $2\text{ kPa}$ ,  $4.7\text{ kPa}$  and  $8.5\text{ kPa}$ .

### Tissue-mimicking materials for ultrasound applications

Soft tissue is highly inhomogeneous. Many properties vary widely over small spatial scales, and high temporal frequencies, that can be difficult to measure or control for. This is especially true on the micrometre spatial scale, and microsecond temporal scale experienced by oscillating microbubbles.

To investigate how ultrasound driven microbubbles interact with tissue, it is helpful to use a controlled, homogeneous environment, with properties that can be accurately measured. A variety of materials have been used in previous studies to mimic soft tissues. These materials have very different properties, depending on the requirements of the particular study.

For the purposes of the present study, it is important for the chosen material to have similar mechanical properties to soft tissue (especially elastic modulus, but also viscosity). It should also be acoustically transparent (to ensure the pressure within the gel is the same as that measured when the gel is not present), optically transparent (to enable clear high-speed microscopy images to be acquired), and stable in water for long periods. Additional considerations include ease of manufacture, handling safety, and cost.

Three of the most common materials used to mimic soft tissues are gelatine, agarose and polyacrylamide (Cafarelli et al. 2017). Gelatine is very simple to produce (simply requiring dissolution in warm water), and completely non-toxic, as it is a common foodstuff. It is also relatively transparent both optically and acoustically (Bude and Adler 1995). Gelatine was tested as a medium for this study. However, when immersed for long periods in water, it was often found to break apart, making it unsuitable for acoustic experiments of the design used here.

Agarose is also extremely common in the laboratory, and similarly easy to produce, as well as being non-toxic. However, it is difficult to produce very soft gels (<20 kPa) that still retain their shape. Agarose is relatively transparent at low concentrations, but it is not perfectly colourless, meaning the quality of imaging through the gel is degraded slightly (Normand et al. 2000).

Polyacrylamide is a very optically transparent hydrogel, which can be made very soft (Young's modulus down to 1 kPa), without breaking apart (Tse and Engler 2010). It is also very stable in water and can be immersed for weeks without degrading, making it ideal for these experiments. The primary downside of polyacrylamide is its more complex production process. A major part of this difficulty is ensuring safety because, while polyacrylamide itself is nontoxic, the acrylamide

monomer is neurotoxic. The polymerisation process is never perfectly complete, meaning lots is left unpolymerised in the gel. Handled correctly, this risk can be minimised, but it is still unsuitable for use with very sensitive biological specimens without further refinement.

Mechanical properties of hydrogels can be measured using nanoindentation, atomic force microscopy (AFM) or oscillatory rheometry. These techniques measure the degree of deformation of the material due to an applied force. In nanoindentation and AFM, this force comes from a small probe which indents into the surface of the material, whereas rheometry uses two parallel plates that twist the whole sample by a given amount. These methods can give different values of elasticity depending on the type of material. Indentation tests are more similar geometrically to the indentation of a bubble investigated here. However, all three can only operate at very low frequencies (up to around 10 Hz) (Oyen 2014). Because material properties vary with applied frequency, these may or may not be relevant to the kHz-frequency indentations applied here by bubbles exposed to 10 ms pulses. It cannot therefore be conclusively predicted from these tests what the mechanical properties of a material would be from the perspective of a microbubble.

### **Summary of approach**

In this study, the effects a single microbubble can exert on its surroundings due to the primary acoustic radiation force are investigated using ultrasound parameters that are typical in therapeutic applications. This is achieved by tracking, with a high-speed camera linked to a microscope, the degree of reversible deformation induced in a soft hydrogel with Young's modulus of 2, 4.5 or 8.7 kPa. These are similar bulk properties to those of soft tissue such as brain (Kaster et al. 2011; Macé et al. 2011; McKee et al. 2011). The ultrasound parameters used here (1 MHz centre frequency, 10 millisecond continuous pulse length, peak rarefactional pressures 0.6 – 1 MPa) are well within the range of those used in applications such as blood brain barrier opening (Choi et al. 2011; McDannold et al. 2006).

The mathematical model described above is used to estimate the radiation force on the bubble and the gel viscosity based on the bubble displacement during each pulse tracked as a function of time.

The maximum indentation depth, and shape of the indentation curve, are used to infer properties of the gel, and the force exerted by the bubble. The maximum indentation depths into the gel of microbubbles exposed to ultrasound are compared for three gel stiffnesses and two channel diameters, to investigate effects due to confinement within a small blood vessel.

## 2.2 Methods

### 2.2.1 Microbubble preparation

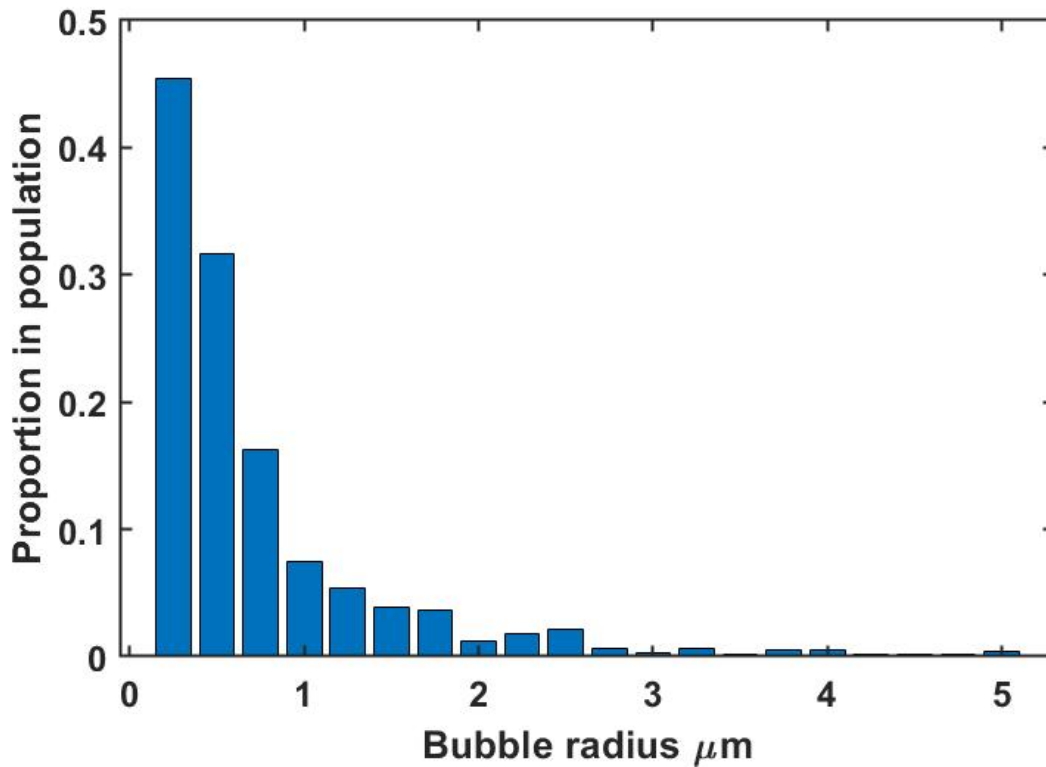


Figure 2.3: Size distribution of in-house manufactured microbubbles used in this study based on a sample of 1805 bubbles.

In-house manufactured microbubbles were made in accordance with a previously described protocol (Koruk et al. 2015; Shamout et al. 2015). The microbubble shell consisted of three lipids (Avanti Polar Lipids Inc., AL, USA) from powder: DPPC (Dipalmitoylphosphatidylcholine), DPPA (Dipalmitoylphosphatidic acid), and DPPE- PEG 2000 (dipalmitoylphosphatidylethanolamine–PEG2000) which were mixed and diluted with glycerol (5% v/v) and saline (80% v/v). Vial headspace was filled with Perfluorobutane and mechanically amalgamated for 45 seconds (Synergy Electronics, Scottsdale, AZ, USA). Microbubbles were extracted from the vial with a 20G syringe needle (with a second needle as a vent hole to allow pressure to equalise in the vial) and then diluted in 0.9% saline. Microbubble size distribution (Figure 2.3) was measured optically using a haemocytometer

and microscope. Images were analysed with open source Matlab software from a previous publication (Sennoga et al. 2010). Mean bubble radius was  $0.88 \pm 1.16 \mu\text{m}$ . Because of the difficulty in acquiring clear images of very small bubbles, only larger bubbles ( $>1 \mu\text{m}$ ) were chosen for imaging.

### **2.2.2 Gel channel preparation**

As described above, polyacrylamide is an ideal material for these experiments due to its high optical and acoustic transparency, and tuneable mechanical properties allowing soft gels to be produced with similar Young's modulus to soft tissues. Polyacrylamide gel was formed using powdered acrylamide monomer and powdered N,N'-methylene bis-acrylamide as a crosslinker. Gels with three different stiffnesses were produced, with acrylamide:bis ratios of 4 % : 0.1 %; 5 % : 0.15 %; and 5 % : 0.3 % (percentage by mass in deionised water). These give values of Young's modulus of  $2.01 \pm 0.75$ ,  $4.47 \pm 1.19$ , and  $8.73 \pm 0.79$  kPa respectively, according to a published protocol (Tse and Engler 2010), which measured gel properties using Atomic Force Microscopy. The solution was degassed by leaving in a vacuum chamber for 30 minutes, with the air inside pumped out to leave a pressure less than 0.2 atmospheres. The degassed solutions were then mixed at room temperature with 0.1 g/100 ml Ammonium Persulphate and 100  $\mu\text{l}$ /100 ml of TEMED and then immediately poured into a box to form the channel. All reagents were obtained from Sigma Aldrich (Dorset, UK).

Gels were formed in a U-shaped box (Figure 2.4). The box was 3D printed in VeroClear resin (Objet 30 Pro). The box had a thin (0.17-0.25 mm thick) plastic cover slip on top, to ensure a flat surface to image through without distortion. It was open to the water on two opposite sides, allowing a free acoustic path to minimise reflections. A glass cover slip was also glued over a hole in the bottom of the box, allowing the channel to be freely illuminated from below. The volume of the gel was 1.5 x 1.5 x 1 cm.

Wall-less channels in the gels were produced by forming the gels around a 25 or 100  $\mu\text{m}$  diameter Nickel/Chromium (80:20) wire, passed between two 30 gauge hypodermic needles, placed around 1 mm from the lower surface of the cover slip, to ensure the channel was close enough to the surface to be imaged clearly. The gel was left for 30 minutes to set. Once the gel had set, the wire was removed and a dilute solution of in-house manufactured microbubbles was introduced to the channel using a syringe pump (PHD Ultra, Harvard Apparatus, Holliston, MA, USA) at a flow rate of 0.1 mL/min. No flow was applied during the sonications to ensure no background motion of the bubbles relative to the channel. Several experiments were also conducted using 10  $\mu\text{m}$  diameter wires, to investigate the feasibility of generating extremely small channels with a similar diameter to a capillary.

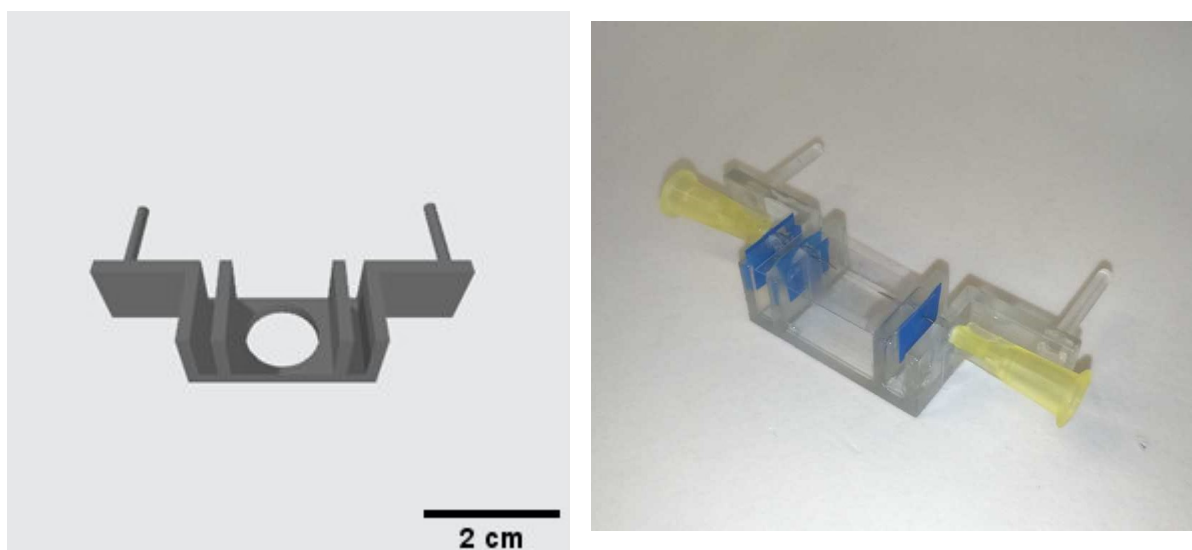


**Figure 2.4:** Scaffold used to construct the wall-less channel. Left) CAD file showing the key support structures of the channel's scaffold. Right) The scaffold was 3D-printed and assembled with a cover slip and needles. This final structure was used to form the channel and introduce the microbubble solution.

### 2.2.3 Gel channel characterisation

The gels were made from a published protocol based on the relative concentrations of acrylamide to bisacrylamide (Tse and Engler 2010). The authors tested the Young's modulus of polyacrylamide with atomic force microscopy, and the values published in this protocol are used here. It should be noted



that a wide variation (> 20%) in elasticity was reported between identically produced gels, and different regions of the same gel.

Polyacrylamide gel is a hydrogel, and properties of polymers and hydrogels vary at very high frequencies (Smyth et al. 2001), and so the relevance of low frequency indentation measurements to the high frequencies (kHz and MHz) of the bubble indentation and radial oscillations is therefore unclear. Hydrogels are often shear thinning, and so the effective viscosity at high frequencies may be lower than that measured at low (Hz) frequencies. This apparent mismatch between viscosity estimated from high frequency bubble dynamics and low frequency oscillatory rheometry has previously been observed (Jamburidze et al. 2017).

Attenuation spectra of the gels were produced to ensure there was minimal scattering and attenuation in the gels compared to water (Figure 2.5). This was important to ensure the pressure within the gel channel was approximately the same as measured by the hydrophone in that location when the gel was not present. This used a 22 mm diameter, plane wave, 1 MHz Olympus immersion transducer sending a short broadband pulse (DPR300 pulser/receiver, JSR Ultrasonics, USA) through a 2 cm thick sample of gel to an aluminium reflector and observing the reflected pulse. The gel must be placed in the far field of the transducer to avoid any nonlinear effects. The distance to the far field is defined as  $D^2/4\lambda$ , where  $D$  is the diameter of the transducer and  $\lambda$  is the wavelength of sound in the medium. For a 22 mm diameter transducer emitting into water ( $c = 1540$  m/s), the far field begins at around 18 cm from the transducer surface. The transducer was placed approximately 19 cm from the surface of the gel. The attenuation coefficient,  $\alpha$ , was calculated based on the following equation, using the sample thickness,  $d$ , of 2 cm:

$$\alpha = 10 \log_{10} \left( \frac{\text{Water FFT}}{\text{Sample FFT}} \right) \frac{1}{2d} \quad (17)$$

This formula assumes minimal reflection off the surface of the gel. 5 gels of each stiffness (2, 4.5 and 8.7 kPa) were tested. For each gel, 100 pulses were tested and averaged. A batch of acrylamide and

bisacrylamide solution was produced for each stiffness of gel, and stored at 4°C when not in use, so the ratio of these should not have varied between the gel samples within each stiffness. However, this approach enabled variations in gel/container position between samples to be accounted for, as well as random changes in gel structures during formation.

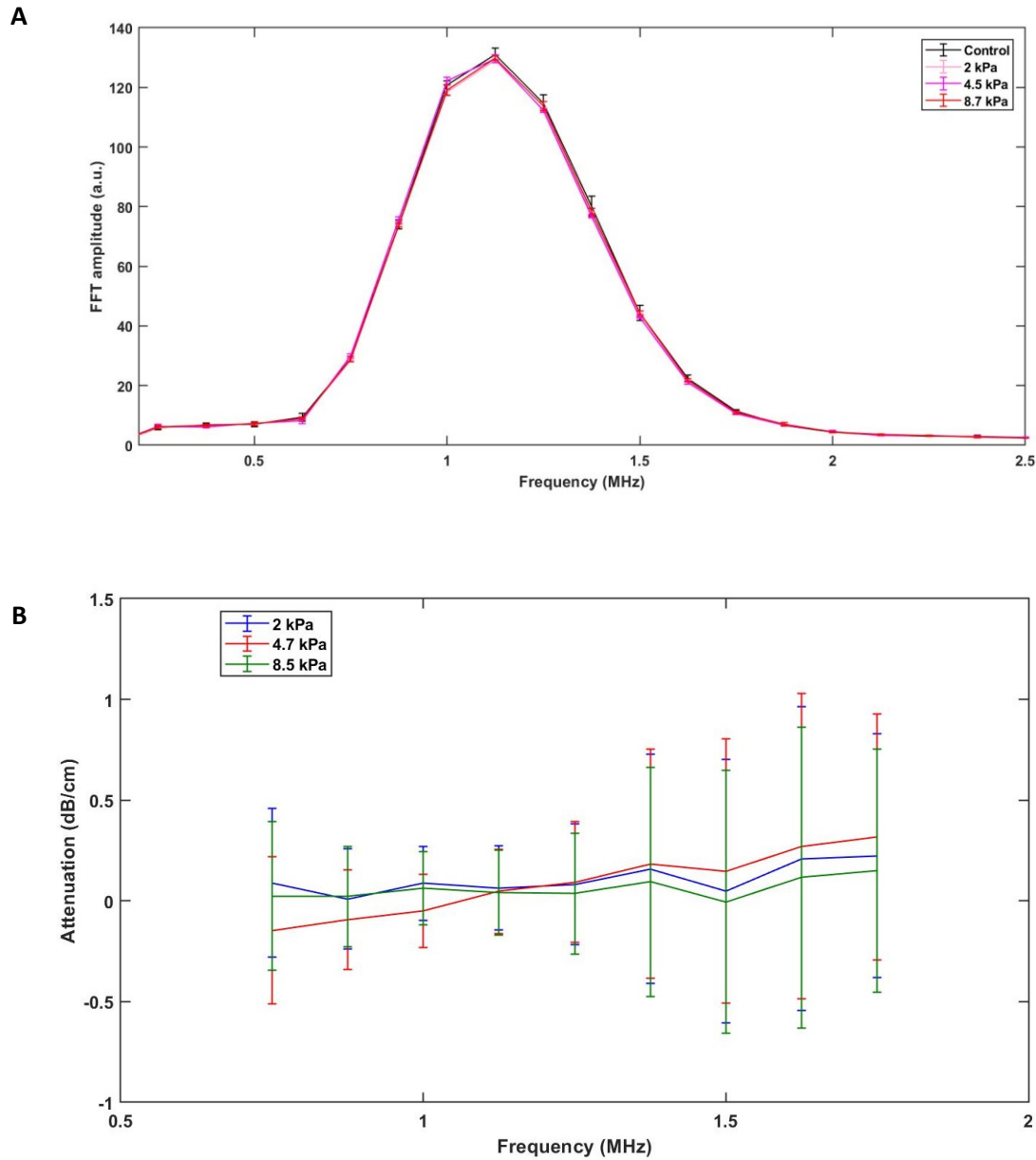


**Figure 2.5:** Attenuation of ultrasound by polyacrylamide gels A) Amplitude spectrum of reflected pulses through water, 2 kPa, 4.5 kPa, and 8.7 kPa gels. Error bars indicate standard deviation across 5 gels. B) Attenuation spectra of the three gels relative to water, demonstrating negligible attenuation at 1 MHz through any of the gels tested. The uncertainties are increased at high and low frequencies due to the lower signal amplitudes.

There was negligible attenuation by any of the three gels at 1 MHz (Figure 2.5), with the maximum value within the error bars for any of the gels being less than 0.3 dB/cm. For all gels at all frequencies, the error bars overlapped with zero. Variation between samples is likely due to electrical or background acoustic noise, or slight variations in the location of the chamber due to exchanging samples, when compared to the measurements for water.

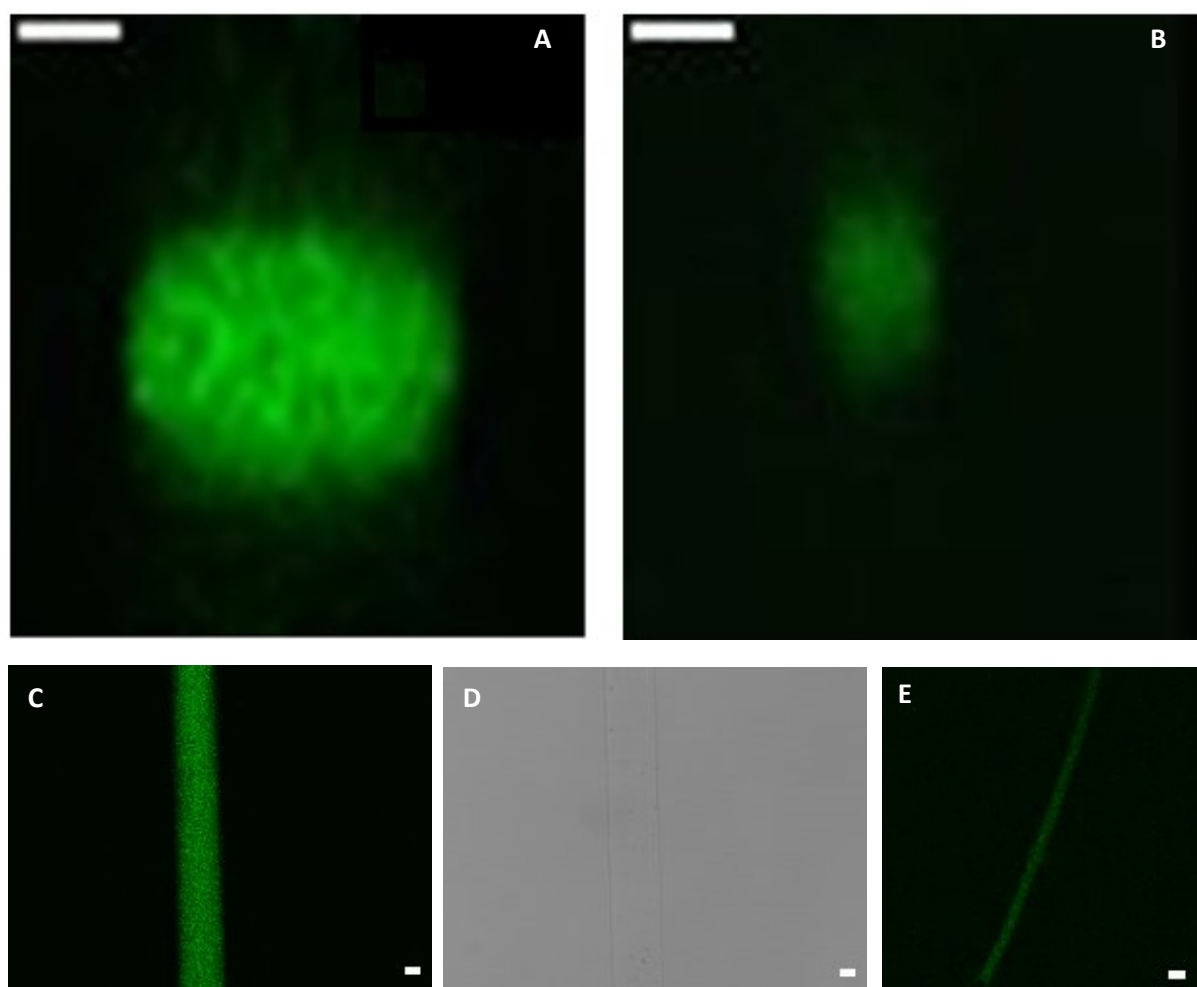


**Figure 2.6:** Confocal images of wall-less channels in 2 kPa Young's modulus polyacrylamide gel after introduction of quantum dots. A-B) Z-projections (vertical projection) of cross-sections through 100 (A) and 25 μm (B) diameter channels. C) Confocal maximum intensity projection and D) Brightfield image of the 100 μm channel. E) Maximum intensity projection of the 25 μm channel. The channel could not be clearly resolved on the equivalent brightfield image. Scale bars: 25μm

Because the gels are soft, there was a concern that the channels left in the gel could have collapsed when the wire was removed. It was difficult to tell the 3D shape of a channel using a brightfield microscope. To confirm their shape, the channels were imaged with a confocal microscope (Leica SP5 MP/FLIM upright). This acquires 3D images of the distribution of fluorescent tracers in a substance. CdSe/ZnS core-shell type quantum dots (Sigma Aldrich) were introduced to the channel to provide fluorescence. The emission wavelength of the quantum dots is  $540 \pm 10$  nm.

The quantum dots are coated with organic layers, consisting of a monolayer of oleic acid/octadecylamine and a monolayer of amphiphilic polymer. The total thickness of organic layers is approximately 4 nm. These extra organic layers reduced the diffusivity of the particles in polyacrylamide and therefore enabled them to function as a reliable marker of the boundary of the channel.

Cross sections of the 25 and 100  $\mu\text{m}$  channels in 2 kPa gels are shown in Figure 2.6. The channel boundaries are well delineated. While the resolution was limited with the 25  $\mu\text{m}$  channels, it was clear that the channel did not collapse and that the cross-section was approximately circular. The 100  $\mu\text{m}$  channel was still clearly patent, and approximately circular in cross-section, albeit with some slight distortion.

### 2.2.4 Optical setup

In order to generate images of individual microbubbles under sonication, a custom high-speed microscope was created using an optical cage system (ThorLabs, Newton, NJ, USA).

Samples were imaged near the top of a water tank using a 40x water-immersion infinity corrected objective lens (Olympus LUMPLFN, numerical aperture 0.8, working distance 3.3 mm, depth of field  $0.57 \mu\text{m}$ ). This was then linked to a 90-degree corner mirror to send the beam horizontally above the tank, through a 1x magnification widefield tube lens, which focussed the beam onto the sensor of a high speed camera (Chronos 1.4, KronTech, Burnaby, BC, Canada). The camera has a monochrome

CMOS sensor with a  $6.6\ \mu\text{m}$  pixel pitch, and is capable of imaging at up to 38,565 frames per second. The frame rate is inversely linked to the field of view of the camera, with the maximum resolution of  $1280 \times 1024$  pixels at 1057 frames per second. The pixel pitch of the images acquired (incorporating the magnification of the whole system) was confirmed to be  $0.16\ \mu\text{m}$  using a haemocytometer. An LED light source (Schott) provided illumination from below. The experimental setup is shown in Figure 2.6.

The whole setup was placed on an actively damped vibration isolation table (Vision IsoStation, Newport, USA). The primary advantage of limiting motion due to environmental vibrations was to increase the likelihood of the sample remaining in focus throughout the imaging period. As mentioned previously, the videos were also motion corrected after acquisition.

### 2.2.5 Ultrasound experiments

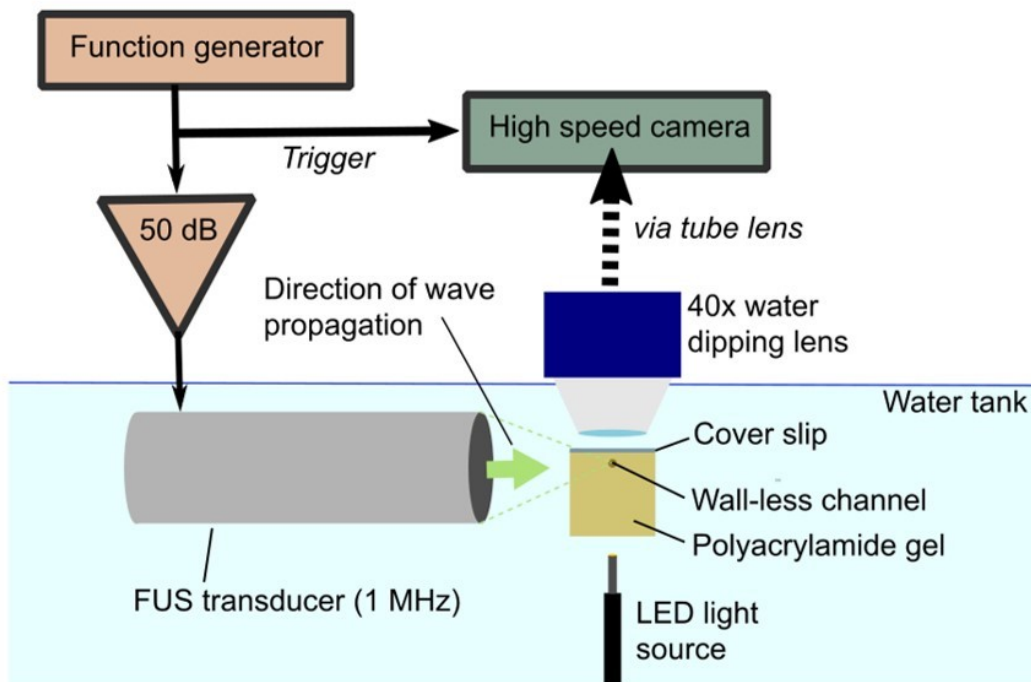


**Figure 2.7:** Setup used for acoustic experiments. The channel was formed in a 3D-printed chamber, and was placed in a water tank under an objective lens.

The channel was placed in a tank of degassed, deionised water under the objective lens. The focus of the transducer was targeted to align with the centre of the focal plane of the lens using a 0.2 mm needle hydrophone (Precision Acoustics). This was also used to calibrate the peak rarefactional pressure in situ. The uncertainty in the pressure values obtained from the hydrophone is approximately 17 %. The pressure calibration was also performed using a 1 mm hydrophone, to ensure the pressure readings were accurate. The pressure values from both the needles were approximately the same, within the uncertainty of the calibration certificates. The pressure readings with the larger hydrophone were expected to be less accurate than the 0.2 mm tip, because it was harder to align the needle to the focus of the lens, and because of spatial averaging of the focus. Pressure values used were therefore those measured with the 0.2 mm needle.

Each sample was sonicated with a single 10 ms tone pulse at 1 MHz centre frequency and 600 kPa PNP (peak negative pressure). 1 MHz was chosen as it is more relevant for therapeutic applications than higher frequencies used for imaging. Lower frequencies are more penetrating, allowing a higher peak pressure to be delivered deep within the body. For the stiffest gels ( $E = 8.7\text{kPa}$ ), a PRP of 1 MPa was used instead, as no deformation could be seen at lower pressures.

Most videos were captured at 4,858 fps using the high-speed camera, although some images of single bubbles were taken at 31,197 fps, to track the shape of the deformation curve in more detail.

### **2.2.6 Transducer calibration**

For these experiments, a 13 mm diameter, 15.2 mm focal distance, 1 MHz narrowband immersion transducer (A303S-SU, Olympus) was used. The beam profile of the transducer was measured using the 0.2 mm hydrophone and an automated 3D positioning system controlled via Matlab. The step size was 0.5 mm, limited by the hardware of the 3D positioning system. The x-y and x-z beam profiles are shown in Figure 2.8. The Full-Width Half Maximum of the beam in the x-y plane is 3.5

mm, measured by fitting a Gaussian curve to the focal region. This was small compared to the face of the gel the transducer is targeted at (1.5 x 1.5cm). The beam size was also small enough in comparison to the working distance of the objective lens (3.3 mm) so that any reflections should be very small. Some small side lobes were present. Their maximum amplitude was <10% of the main peak, and only slightly above the noise floor (Figure 2.8).

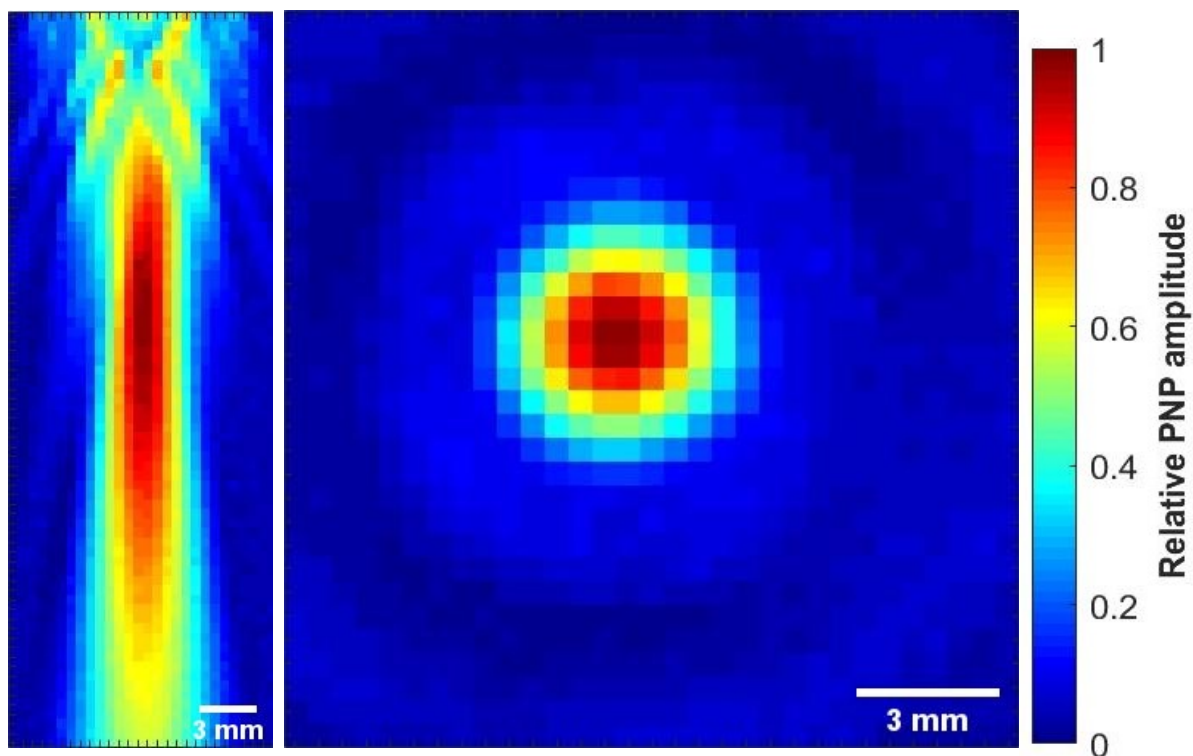


**Figure 2.8:** 1-MHz transducer beam profile. Left) Axial-lateral profile (transducer at the top of the image). Right) Horizontal beam profile at the focus. Step size 0.5 mm. The peak pressure at the focus was 400 kPa. The pulse length used was 10 cycles, chosen to avoid reflected pulses affecting the measurements, while being long enough to ensure a steady-state maximum pressure amplitude.

The objective lens used could not be immersed more than a few millimetres into the tank, and has a working distance of 3.3 mm. Because the transducer has a relatively small diameter, it could be placed horizontally relative to the imaging plane of the lens, remaining completely immersed in the water tank while its focus was aligned with that of the objective. This allowed the camera to image

horizontal motion of the bubbles throughout the pulse in the plane in which the force was being applied.

The focal distance of the transducer is also relatively small (FWHM of 3.5 mm). The combination of this and the small diameter creates a tight focus, reducing the amplitude of ultrasound in locations away from the channel, and thus limiting the impact of reflections off surrounding surfaces. The tight focus also allowed higher pressure amplitudes to be achieved in the focus for a given input power amplitude.

### **2.2.7 Image analysis**

Bubble motion was tracked in Matlab (MathWorks, MA, USA). Videos were first cropped to focus on the bubble, with as little background or pieces of dust/debris in the image as possible. In most videos, there was a degree of background motion present, primarily due to environmental vibrations. This was corrected for with a cross-correlation method. To do this, a region of the channel boundary well away from the bubble was manually identified. The approximate magnitude of motion over the pulse was estimated to determine how large a region in which this section should be compared against in each subsequent image. To enable sub-pixel resolution, the selected regions were first interpolated using a spline function (built-in 2D Matlab interpolation function). The region of the initial frame was compared against a corresponding region in each subsequent frame, using the built-in 2D cross correlation function in Matlab. This provided a robust method for background correction. It also enabled the shape of the deformation curves to be assessed more reliably. However, because the rapid relaxation of the bubble after the pulse occurred over far shorter timescales than vibrational motion of the background, this background motion did not significantly improve estimates of maximum indentation depth.



Once the videos had been motion-corrected, bubbles were identified automatically in each image using an arbitrary threshold method. The intensity threshold chosen was a global intensity threshold value, and was given as a decimal of the full 8-bit intensity range (0-256). As can be seen in Figures 2.9 and 2.10, bubbles generally had quite high contrast against the surrounding channel, with the bubble being much darker than the background (except for a bright spot in the centre), enabling the use of a simple threshold technique to form a binary image that separates out the bubble. Following a choice of threshold, small groups of pixels were removed from the binary image if they were too small to be a bubble. The value of the pixel area threshold was chosen manually, and was significantly smaller than the smallest microbubble imaged.

The radius obtained varied depending on the value of intensity threshold and Hough transform sensitivity used. A typical threshold of around 0.2-0.3 was used (as a decimal of the maximum intensity value), to select a region that was relatively insensitive to small intensity variations (Fig 2.9). However, this varied slightly depending on the video used, as the brightness levels varied somewhat between videos. The variation across the flat region from 0.1-0.5 is around 0.2  $\mu\text{m}$ , although extreme values of this are likely to be unreliable. This is therefore a conservative estimate of the uncertainty in the radius. A similar uncertainty was also measured with much larger bubbles, indicating this is an absolute error arising from the pixel resolution and not a percentage error in bubble size. As can be seen in Fig 2.8, the sensitivity value does not significantly affect the values of bubble radius. This value was therefore chosen simply to ensure the correct feature in each video was identified as a bubble.

Following thresholding and clutter removal, bubbles were identified in the binary images using a Hough transform built in to Matlab. This fits a circle to the bubbles, giving a value for initial radius, and the centroid of the bubble across each frame. The sensitivity of the Hough transform was adjusted manually for each image to ensure it identified only the one bubble being tracked.

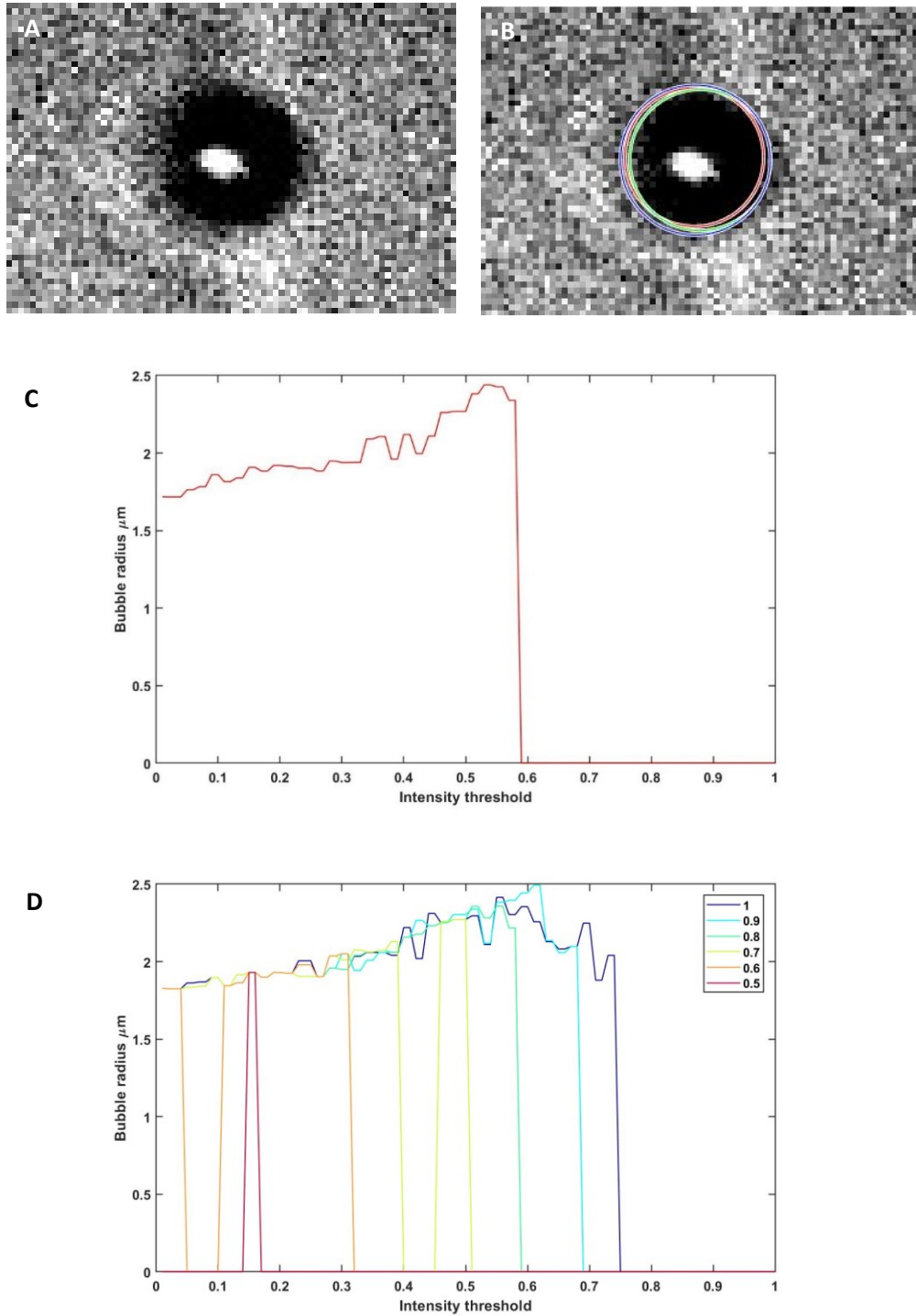


**Figure 2.9:** Automated segmentation of bubbles in high-speed video images. A) Example image of bubble used to generate plots in C and D. B) Bubble image overlaid with circles obtained from the code at intensity thresholds of 0.1 (red), 0.2 (green) and 0.3 (blue). C) Effect of intensity threshold on values of bubble radius for a sensitivity value of 0.8. D) Effect of sensitivity value and intensity threshold on measured bubble radius. Values of zero indicate that no bubble could be found in the image

It is important to measure the radius of each bubble from the images accurately and reliably for input into the model. The values of sensitivity and intensity threshold used can affect estimates of bubble radius. An example is shown in Figure 2.9 for estimates of bubble radius vs chosen intensity threshold. As this shows, the radius does not vary significantly until the threshold reaches a certain value, at which point the bubble can no longer be identified as circular in the image, and no bubble is found. Based on the variation in radius estimates across the flat region, the uncertainty in measurements of bubble radius is estimated to be approximately  $0.2\text{ }\mu\text{m}$ . The estimated radius as a function of threshold is plotted for sensitivities ranging from 0.5 (most sensitive) to 1. The sensitivity values do not significantly affect the estimated radii. However, if the sensitivity value is too low, the bubble is not found at all (indicated by the radius measured as zero on the graph). It is therefore important to choose an appropriate value of sensitivity for bubble tracking over multiple frames, to ensure the bubble is found in all frames.

Segmentation of every video was performed with manual oversight, to ensure bubbles were acquired correctly. For instance, an approximate bubble radius was estimated manually, so as to exclude values generated by the software which were significantly different from this value, indicating that the bubble had not been accurately captured. In each frame of the image, the estimate of bubble location and size was plotted over the video, to ensure the software was correctly identifying the correct feature in the image as the bubble.

While the transient displacement of the boundary in contact with the bubble will likely be slightly greater than the displacement of the centre of the bubble owing to the bubble's volumetric expansion during the pulse, tracking the centre was deemed to be the most reliable approach to tracking displacement at these frame rates. This is because the edge of the bubble cannot be accurately resolved as it is slightly blurred during the pulse due to the bubble's radial oscillations.

For the quantitative analysis in Figures 2.12 and 2.13, bubbles (or potential bubbles) were excluded under the following circumstances: they exhibited no clear response to ultrasound at all (as they

may not have been bubbles); if their diameter was  $< 1\ \mu\text{m}$  (as the resolution of the camera meant they could not then be reliably identified as spherical bubbles, as opposed to lipid droplets or solid fragments, and their radius could not be measured accurately); they did not return to within the channel after the pulse (indicative of gel disruption); the bubble was within  $50\ \mu\text{m}$  of another bubble or there was any obvious interaction with neighbouring bubbles; the bubble was nearby an obvious imperfection in the gel; or if they were out of focus in the initial or final frames (unable to reliably determine the initial bubble radius). Some videos of bubbles close to each other were obtained (such as in Figure 2.11) for general observations, but these were not included in the analysis shown in Figures 2.12 and 2.13.

### **2.2.8 Data analysis**

For each video, the maximum indentation depth was measured from the relaxation of the bubble after the pulse. This was taken as the difference between the position of the centre of the bubbles averaged between 9-10 ms from the start of the pulse, and between 2-3 ms from the end of the pulse. These points were chosen empirically to avoid the relaxation of the bubble, because the displacement was usually flat in those periods (see Figure 2.12). The relaxation of the bubble after the pulse was chosen as the bubble can be assumed to be in direct contact with the gel during this period. This may not necessarily be the case before the pulse. Because of their small size and consequently low Reynolds number, bubbles will generally not move unless driven directly by either the ultrasound or the elasticity of the gel (or any background fluid flow, which was avoided where possible). The indentation depths were compared between groups using a one-way MANOVA test.

The uncertainty of the measurements of indentation depth was determined by the standard deviation of the bubble displacements during the two reference time periods (9-10 ms from the start of the pulse, and between 2-3 ms from the end of the pulse). The standard deviations of the bubble centroids were generally around  $0.1 - 0.2\ \mu\text{m}$ . This is very close to the pixel size (around  $0.16\ \mu\text{m}$ ). This variation did not vary substantially with indentation depth. The standard deviation was

generally slightly larger in the period during the pulse, as bubbles could experience some random motion driven by the ultrasound. Unless otherwise specified, the uncertainty in measurements of indentation depth was taken as  $0.3\text{ }\mu\text{m}$  (approximately double the uncertainty in each location due to the difference between the two measurements).

### **2.2.9 Modelling**

The motion of each bubble extracted from the videos was fitted to a viscoelastic model of a bubble penetrating a tissue interface, which was described in detail in §2.1 (equation 15). In this model, the gel was modelled as a linear viscoelastic medium, and was assumed to be isotropic, homogeneous and incompressible. The model does not account for bubble radial oscillations, which would be present in reality.

The model assumes the bubble is indenting a plane boundary. In this case, the bubbles were in a cylindrical channel, meaning the boundary is slightly curved. Because the bubble diameter of a few micrometres is significantly less than the channel radius of  $100\text{ }\mu\text{m}$ , this was assumed to be of minimal significance in modelling.

For every bubble, the time averaged force was estimated based on the maximum indentation depth, bubble initial radius and gel Young's modulus. For a small sample of bubbles which were imaged at higher frame rates, the viscosity of the gel was also inferred from the rate of relaxation after the pulse.

Parts of the Matlab code used to implement the model here were written by Dr Hasan Koruk, who also generated the simulation results in Figure 2.12.

## **2.3 Results**

The study aimed to observe and analyse the reversible indentation of single bubbles into a gel boundary under a range of different bubble sizes, gel properties and ultrasound parameters.

### **2.3.1 Selection of channel diameter**

The feasibility of introducing bubbles to the channels, and observing indentation was first addressed. Several examples of channels of 10  $\mu\text{m}$  diameter were successfully created in 8.7 kPa gels, and microbubbles could be introduced as shown in Figure 2.9. These channels are potentially valuable as their diameter is much closer to that of a capillary than for the larger channels. However, introducing bubbles to a channel of this size was very unreliable, and could not be achieved in the softer gels.

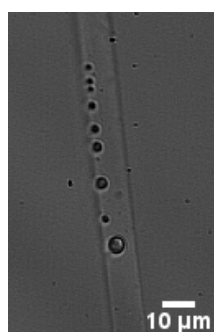


Figure 2.10: Brightfield image of microbubbles within a 10  $\mu\text{m}$  diameter channel in 8.5 kPa Young's modulus polyacrylamide gel

The ultrasound experiments were therefore performed with the larger (25 and 100  $\mu\text{m}$ ) channels mentioned previously. Despite the very soft material, both the 25 and 100  $\mu\text{m}$  diameter channels remained patent after the wire was removed, and microbubbles could be reliably introduced to the channels for clear brightfield imaging.

### **2.3.2. Feasibility of elastic indentation with a single microbubble**

Once the channels had been created, the feasibility of elastic indentation of single microbubbles was investigated under a range of ultrasound parameters. In Figure 2.11, three bubbles in 25  $\mu\text{m}$  channels in 2 kPa gels are exposed to a 2 millisecond pulse at PNP of 600 kPa. All three bubbles indent into the gel by several micrometres and then return to within the channel at the end of the

pulse. Here, it is very clear that the bubbles have passed beyond the initial boundary of the vessel, indicating the movement of the bubble is due to deformation of the material. The three bubbles are of similar sizes and move similar distances, indicating the material properties and acoustic parameters within the channel are relatively homogeneous over these spatial scales, assuming the bubbles respond similarly to the ultrasound.

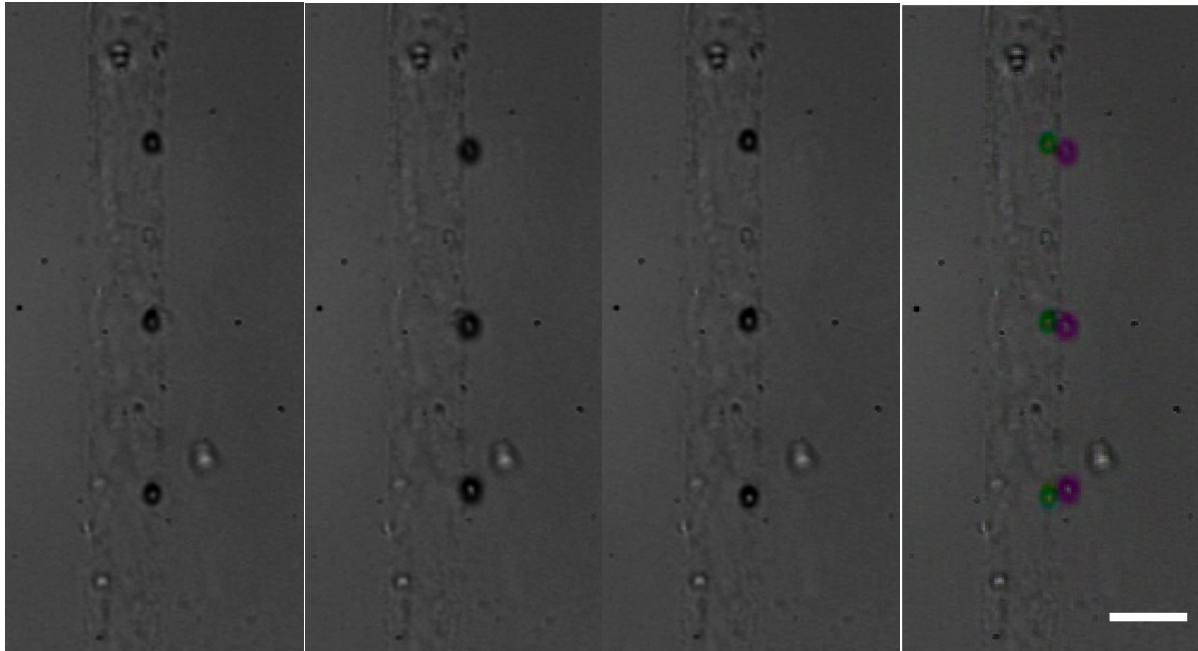


**Figure 2.11:** Feasibility of elastic indentation with a single microbubble. Microbubbles in a 25  $\mu\text{m}$  diameter channel (highlighted) in 2 kPa polyacrylamide gel, exposed to a 2 ms, 600 kPa PNP, 1 MHz pulse. The bubbles indent into the gel by around 2  $\mu\text{m}$ , before relaxing back to within the channel. Left-to-Right: Before (0 ms), maximum indentation (2 ms), after (5 ms), colour image with the before (green) and maximum indentation (magenta) images overlaid. The bubbles move slightly towards each other during the sonication due to secondary radiation forces. Ultrasound propagates from left to right. Scale: 25  $\mu\text{m}$

For the remaining experiments, 10 millisecond, 600 kPa pulses were used for the 2 kPa gels. These pulses were chosen, based on trial and error, to be long enough to ensure the bubbles reach a clear steady-state displacement within the gel, and of a pressure high enough to ensure the bubbles would indent a measurable amount into the gel, but not so much as to disrupt the gel and tunnel into it.

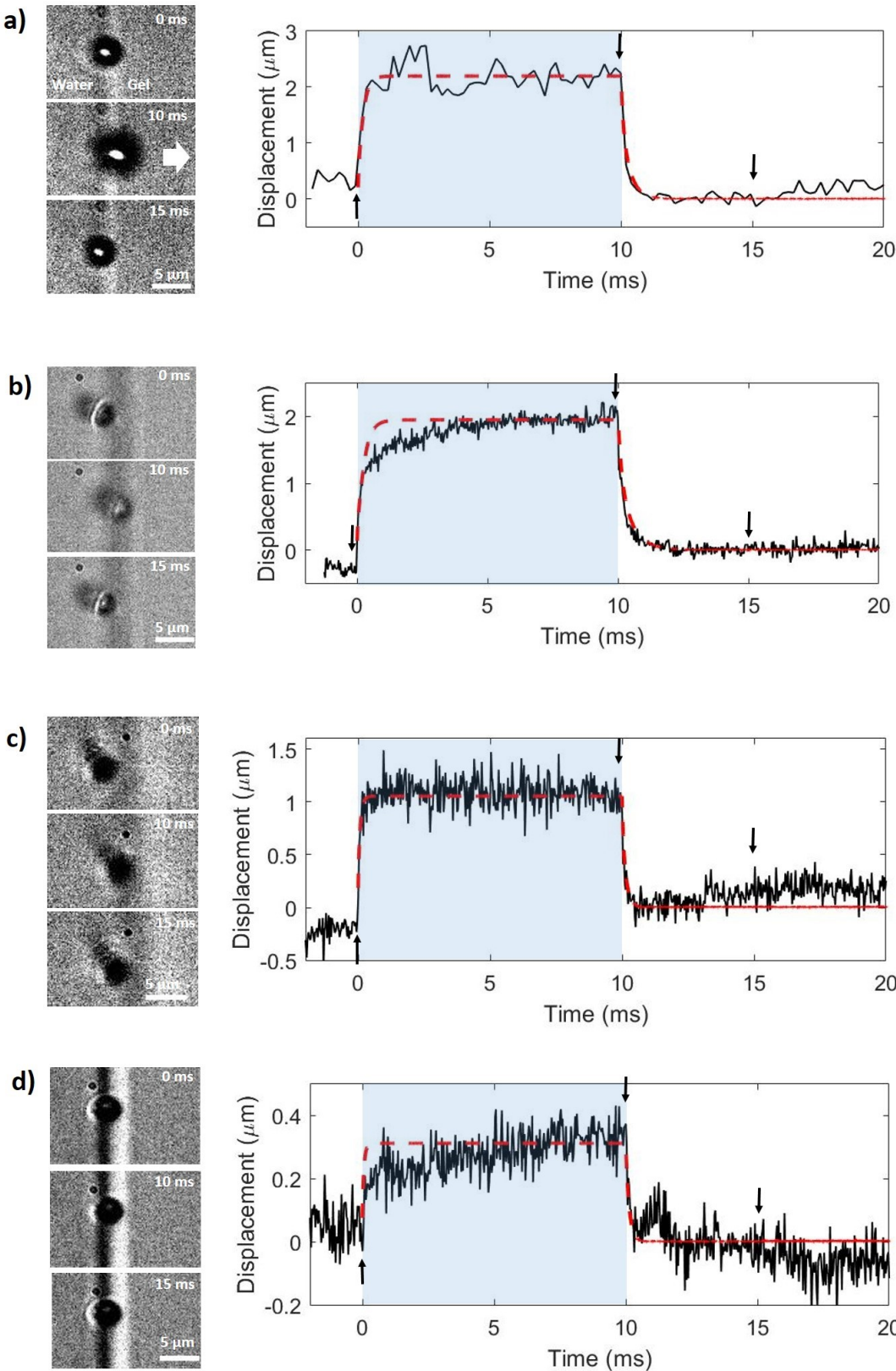




**Figure 2.12:** Example indentation curves for four individual bubbles impacting gels with different stiffnesses.

Frames from each video are shown on the left, with the x-coordinate of the centre of the bubble shown over time in a plot on the right. Arrows indicate the points at which each still was taken. The duration of the pulse is shaded in blue. Curves fitted to the data based on the mathematical model are represented by dashed lines in red. These curves were used to extract the radiation force on each bubble and the viscosity of the gel. The white arrow indicates the direction of wave propagation (left-right in all images). (a) Example deformation curve for a 2.0  $\mu\text{m}$  radius bubble indenting a gel with a Young's modulus of 2 kPa. Frame rate: 4,858 frames per second (fps). Parameters extracted from the model are radiation force = 19 nN and viscosity = 0.12 Pa s. (b) Bubble radius = 1.5  $\mu\text{m}$ . Gel Young's modulus = 2 kPa. Frame rate = 31,197 fps. Radiation force = 13 nN, viscosity = 0.18 Pa s. (c) Bubble radius = 1.5 mm. Gel Young's modulus = 4.5 kPa. Frame rate = 31,197 fps. Radiation force = 15 nN, viscosity = 0.12 Pa s. (d) Bubble radius = 1.6 mm. Gel Young's modulus = 8.7 kPa. Frame rate = 31,197 fps. Force = 4.5 nN, viscosity 0.2 Pa s.

A total of around 150 videos of single bubbles were identified as being suitable for analysis. These were across four different scenarios: 25  $\mu\text{m}$  channels in 2 kPa gels, and 100  $\mu\text{m}$  channels in 2, 4.7 and 8.5 kPa gels.

The results for four different test cases in Figure 2.11 show that microbubbles (1.5-2.0  $\mu\text{m}$  in radius) reversibly deformed the soft ( $E = 2, 4.5$  and 8.7 kPa) gels (exposed to ultrasound of 1 MHz centre frequency and 0.6 or 1 MPa peak rarefactional pressure). Bubbles typically reached a maximum indentation depth of several micrometres after a few milliseconds, and remained in this position until relaxing to close to their initial state at the end of the pulse, again over a few milliseconds. Microbubbles almost always clearly returned to within the channel after the pulse, indicating the gel had not been significantly plastically deformed. However, the final location was often slightly different to the initial location.

The results in Figure 2.11, showing the model fitted to the experimental results, demonstrate that the model is capable of accurately describing the qualitative shape of the indentation curve of a bubble into a viscoelastic material. Various quantitative parameters were extracted from the

experimental data using the model, although the validity of these numbers cannot be verified with an independent method.

### **2.3.3 Estimates of applied force**

When exposed to a 600 kPa PRP ultrasound pulse, the force on a 2  $\mu\text{m}$  radius bubble experiencing a maximum displacement of around 2  $\mu\text{m}$  was estimated to be 19 nN (Figure 3a). The force level decreased to 13 nN for a 1.5  $\mu\text{m}$  radius bubble and a maximum displacement of around 2  $\mu\text{m}$  (Figure 3b) for 2 kPa gel. The force level was estimated to be 15 nN for a 1.5  $\mu\text{m}$  radius bubble and a maximum displacement of around 1  $\mu\text{m}$  for 4.5 kPa gel (Figure 3c). Both displacement and force were estimated to decrease as gel stiffness increases, even when the ultrasound pressure is increased in 8.7 kPa gels. The force level is 4.5 nN for a 1.6  $\mu\text{m}$  radius bubble and a maximum displacement of around 0.3  $\mu\text{m}$  for 8.7 kPa gel, when exposed to 1 MPa PRP ultrasound pulse. Overall, the time-averaged radiation force on a microbubble under these ultrasound parameters is estimated to typically be of the order of tens of nN (Figure 2.13)

The viscosities of all three gels were estimated at between 0.1 - 0.2 Pa s. A bubble responds faster as the Young's modulus of the gel increases and its viscosity decreases. The maximum displacements into the gel of over 150 individual bubbles were measured (Figure 4). The size distribution of these bubbles was typical for the population, with the majority being between 1-3  $\mu\text{m}$  in radius. The number of larger bubbles tested was very small due to their scarcity in the population. Maximum indentation depths for these bubbles were typically less than 4  $\mu\text{m}$ , although this varied significantly, even between bubbles of very similar size. The initial and final locations of each bubble were often slightly different. This may be because the bubble was not initially in contact with the wall before the pulse, or because of some movement along the curved channel wall in the vertical direction parallel to the imaging plane.

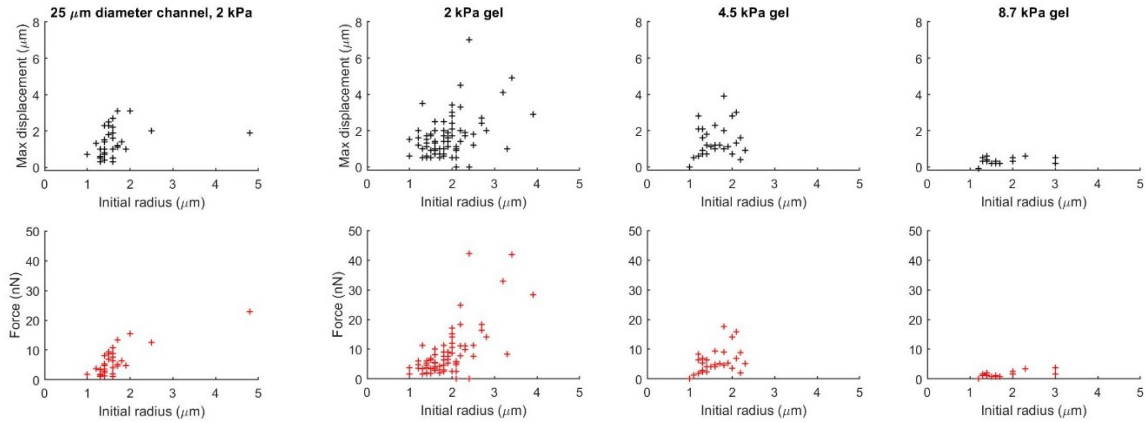


**Figure 2.13:** Maximum indentation depth vs initial bubble radius for two different channel diameters and three different gel stiffnesses. The uncertainty in measurements of radius is approximately  $0.2 \mu\text{m}$ . The uncertainty in indentation depth is approximately  $0.3 \mu\text{m}$ .

There was a statistically significant difference between indentation depths of bubbles in the  $100 \mu\text{m}$ ,  $2 \text{ kPa}$  channel at  $600 \text{ kPa}$ , and in the  $100 \mu\text{m}$ ,  $8.7 \text{ kPa}$  channel at  $1 \text{ MPa}$  (p-value:  $1.5\text{e-}4$ ), with the stiffer gels showing much smaller indentation depths, even with the higher pressures. There was no statistically significant difference between bubbles in  $100 \mu\text{m}$  channels in  $2 \text{ kPa}$  and  $4.5 \text{ kPa}$  gels (p:  $0.12$ ). There was no statistically significant difference between the  $25 \mu\text{m}$  and  $100 \mu\text{m}$   $2 \text{ kPa}$  channels (p:  $0.26$ ). The bubble radii were compared between the four groups and no significant differences were observed between any pair of groups, indicating this was not the source of the variance between the samples.

### 2.3.4 Qualitative observations

In addition to the bubble indentation results presented above, a number of bubble behaviours were observed which are important to note. Many of the largest bubbles (Radius  $> 5 \mu\text{m}$ ) exhibited surface modes or non-spherical behaviours, which could clearly be seen even at the low frame rates and long exposure times used here (Figure 2.14). These surface modes may have been present in smaller bubbles, but the spatial resolution made this impossible to verify. Bubbles occasionally

fragmented during the pulse, or (more commonly) dissolved shortly ( $< 1$  second) after. Dissolution was especially observed as a result of the 1 MPa pulses used in the stiffest gel.

Several control videos were obtained of gels without any bubbles, to track the motion of the channel wall due to the radiation force on the gel alone. No local gel wall motion could be identified as being due to the pulse, beyond some slight background vibrations of the whole sample. These were largely present without the ultrasound, also some motion of the whole channel was caused by the ultrasound. This did not affect the data analysis, however, as bubble motion was measured relative to the channel.

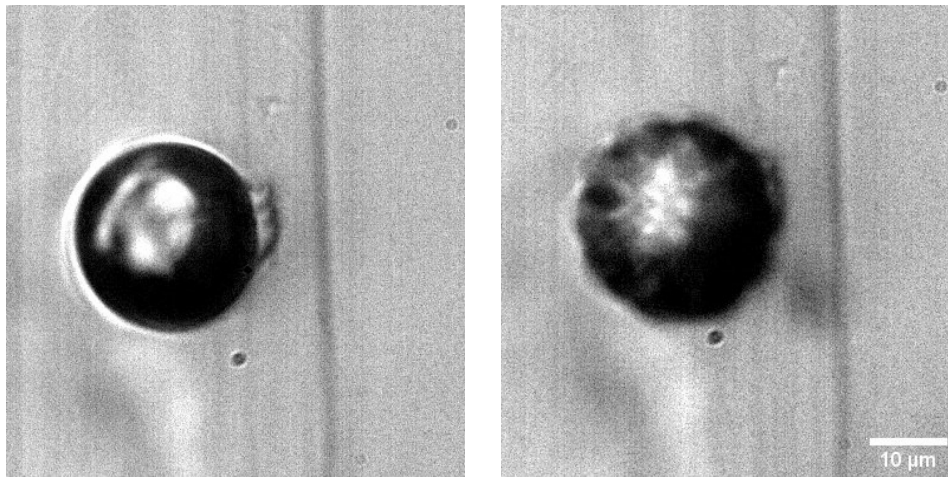


**Figure 2.14:** Examples of non-spherical oscillations of a large microbubble (L: before and R: during a 10 ms pulse). Despite the low frame rates used here, it is clear in this video that the bubble is not spherically symmetric.

## **2.4 Discussion**

As shown in the results presented here, individual microbubbles can reversibly deform soft gels using the primary radiation force. This indicates that, under the acoustic parameters tested, which are typical of those used in many therapies, especially blood-brain barrier opening, the radiation force on a bubble is likely to generate significant local tissue stresses, and potentially micron-scale displacements, in very soft tissues, such as brain tissue.

Very little deformation was observed in stiffer gels ( $E = 8.7$  kPa). At 1 MHz, no deformation was observed at 600 kPa, and small deformations could only be observed at high pressure ( $> 1$  MPa). However, many lipid shelled microbubbles rapidly dissolve or fragment at these pressures, as has been reported previously (Borden et al. 2005; Cox and Thomas 2010; Cox and Thomas 2013; Kwan and Borden 2010a). Enabling microbubble-induced indentation of stiffer tissues may therefore require microbubbles that are more resilient to high acoustic pressures. In stiffer tissues therefore, such as arteries and muscles, direct mechanical effects of lipid shelled microbubbles due to radiation force are therefore likely to be confined to close to the vascular wall.

We have also demonstrated the potential to use the indentation of a bubble into a soft gel to estimate the radiation force on a single bubble, and the viscosity of the surrounding medium. This provides a tool to quantify or empirically model the forces microbubbles exert on their surroundings. This could help to refine modelling of microbubbles' effects on tissue. Additionally, if the radius of a microbubble is known, and its radiation force can be independently calibrated from the ultrasound parameters, the elasticity of the medium could be estimated from the bubble's maximum indentation depth.

The shape of the deformation curves predicted by the model approximately matched those observed experimentally, demonstrating the qualitative validity of the model. The values of radiation

force estimated from the model could not be verified with an independent method, however, and so these results cannot conclusively establish the quantitative validity of the model.

The forces estimated from the model were typically of the order of a few tens of nanonewtons in the 2 and 4.5 kPa gels. For the 8.7 kPa gel however, these forces were estimated at around 5x lower. This is despite the bubbles in the stiffer gel being exposed to significantly higher ultrasound pressures (1 MPa vs 0.6 MPa). This may be due to confinement effects related to the proximity of the more rigid boundary. When a bubble is in contact with a very soft boundary, the effect of its acoustic response is relatively small (Helfield et al. 2014), compared to very significant damping of oscillations when a bubble is in contact with a rigid boundary (Garbin et al. 2007; Overvelde et al. 2011). The difference could also be due to the 8.7 kPa gel being much stiffer than expected at high frequencies, as its elasticity was only measured at low frequencies using AFM.

There was significant variation in the amplitudes of deformation between apparently almost identical bubbles, and it was difficult to observe a clear trend with bubble resting radius. There are many potential reasons for this. The stiffness of each gel measured via AFM can vary significantly in different regions (Tse and Engler 2010). Previous studies on acoustic radiation force in a free fluid have also shown similar degrees of variation (Dayton et al. 2002), suggesting intrinsic variation in acoustic response between bubbles of similar size. This could be due to variation in shell structure between bubbles (Borden et al. 2006). Other reasons may include variable formation of standing waves around the lens, and inhomogeneities in the directionality of the acoustic pressure field due to scattering between different surfaces near the channel.

At the pressures tested here, almost all bubbles appeared to return to within the channel after the pulse, and so we assume no permanent structural changes were imparted to the gel, as has previously been reported in agarose at higher pressures (Caskey et al. 2009). In some instances, the final location of the bubble was slightly different to the initial location. This may be due to the

bubbles not being in contact with the gel surface initially, but may also indicate slight plastic deformation.

For very small deformations, it is unclear whether the bubble motion is due to the elasticity of the gel, or to deformation of the bubble itself, without much higher spatial and temporal resolution than used here. Vertical motion of the bubble is also an issue, as it can cause it to move in and out of focus. This was minimised by selecting only bubbles that were close to the focal plane of the lens throughout the pulse.

Much larger pressures ( $>1$  MPa) were not tested. It may therefore have been possible to generate more substantial displacements in the 8.7 kPa gels (and stiffer media) if higher pressures had been used. However, while bubble breakup was rare at 600 kPa, it became increasingly common at 1 MPa, making it likely that the bubbles used here would not be able to survive long enough at much higher pressures to reach a stable maximum equilibrium displacement in the gel.

The ultrasound parameters used here are comparable to those used in therapies such as ultrasound blood-brain barrier opening. This research therefore provides a deeper understanding of the forces the bubbles are exerting when generating these effects. It may also have relevance to radiation-force targeting in molecular ultrasound imaging, as a way of estimating any potential mechanical effects on tissue.

These results also clearly demonstrate that the primary radiation force is also a significant contributor to the mechanical effects in addition to volumetric oscillations that are more widely studied. In comparison to volumetric oscillations, the primary radiation force is applied in only one direction. This therefore may be valuable as a way to manipulate microbubbles or tissue.

This study provides further insight into the potential for the radiation force on a microbubble to be used to probe tissue mechanical properties at micron-scale spatial resolution. While the range of displacements induced by bubbles was extremely variable, the significantly lower displacements in

the 8.7 kPa gel compared to the softer gels indicate this technique may be able to generate a source of contrast between different tissue elasticities. Bubbles rapidly reach a stable maximum depth, which is dependent on tissue stiffness. This potentially enables micron-scale tissue stiffness variation to be measured from individual bubble dynamics acoustically tracked with super-resolution imaging at achievable frame rates ( $<1$  kfps).

## **2.5 Conclusions**

Sustained, localised, and reversible tissue indentation due to the primary radiation force on single microbubbles has been observed in soft tissue-mimicking materials, when exposed to typical therapeutic ultrasound pulses. The degree of displacement varies widely, even for similarly sized bubbles interacting with gels of the same stiffness. However, the degree of deformation is linked to the stiffness of the gel.

This research provides insight into the nature of the forces that microbubbles may exert on tissues during therapy, and the degree of tissue displacement that may be induced by single microbubbles within the microvasculature.

While the large variation in results currently restricts the potential of this to provide precise estimates of tissue properties, the difference in displacements between different gels shows microbubble-induced primary radiation force could provide a source of contrast between regions of different tissue elasticities.

However, the significantly lower radiation forces inferred for the tests with the 8.7 kPa gels compared with the softer gels are surprising, given the radiation force should likely be higher because of the higher ultrasound pressures used. This could be refined in future by experimentally evaluating the validity of the model used, investigating the impact of a stiffer wall on bubble dynamics, and through more detailed testing of the properties of the polyacrylamide gels, and especially how these vary at high frequencies.



# Chapter 3: Microbubble interactions with brain microvessels

## 3.1 Introduction

In the previous chapter, microbubble behaviours are investigated in wall-less vessels within tissue-mimicking materials. Artificial vessels in hydrogels provide controlled conditions in which to analyse and quantify bubble-tissue interactions. However, the relevance of these to biomedical applications is limited due to significant differences between the properties of hydrogel channels and those likely of the microvasculature of living tissue. Hydrogels are very homogeneous compared to brain tissue, and the channels created, while still quite small, and comparable to some microvessels, were considerably larger than the typical diameter of a capillary. While bulk properties of tissue can be easily determined and replicated, the microscopic properties of the brain microvasculature in an artificial setting are extremely challenging to measure and reproduce artificially.

In this chapter, microbubbles are observed during ultrasound exposure in a more physiologically relevant setting. This chapter has several aims. Firstly, to develop a technique to directly observe microbubbles in living brain tissue. Secondly, to use this technique to observe how microbubbles behave within and interact with brain tissue during ultrasound pulses typical of those used in blood-brain opening. Finally, to investigate the physical phenomena which may be involved in the process of delivering drugs across the blood-brain barrier. This could provide insight into the physical and biological mechanisms of ultrasound and microbubble-mediated blood brain barrier opening.

### 3.1.1 Tissue models for observation of microbubbles

To understand how microbubbles behave in brain microvessels, a suitable experimental platform must first be chosen. There are many different approaches to observing microbubbles in biological tissue, each of which has advantages and disadvantages. There are several key criteria in determining suitability for this study.

Firstly, the platform used must be a good approximation to the properties of brain. This includes mechanical properties such as stiffness and viscosity, and microvessel size. It should also have good biological similarity to the blood-brain barrier (BBB), and should be as biologically similar as possible to *in vivo* settings during experiments.

In order to image microbubbles clearly, the sample needs relatively high optical transparency. Because of the high frame rates needed, and lack of fluorescence imaging apparatus, the sample should be able to be backlit, enabling brightfield microscopy with high image contrast. The experimental setup should also be acoustically transparent, and designed in a way that avoids reflections or other artifacts, that could introduce standing waves or uncertainties in the nature of the pressure field in the imaging region. There are also several practical constraints. The experiments must be performed using equipment that can be obtained. Compliance with Home Office regulations and licences must also be considered for any experiments involving animals or animal tissue.

An obvious method to investigate microbubbles in live brain tissue is to perform *in vivo* experiments on animals such as mice. Direct observations of drug extravasation using intravital microscopy have been performed *in vivo* previously (Burgess et al. 2014; Raymond et al. 2007). However, these techniques are extremely limited in their ability to capture microbubble activity directly. These approaches typically require multiphoton fluorescence microscopy, as the imaging region cannot be backlit for brightfield imaging, meaning fluorescent tags would have to be attached to microbubbles to observe their locations (Crake et al. 2016). The frame rates achieved using multiphoton imaging

are low, typically no more than a few tens of frames per second: too low to image microbubble behaviour over a typical 10 millisecond pulse. In the future though, it may be possible to increase this to kHz rates with emerging technologies (Karpf et al. 2020). Finally, intravital fluorescence microscopy is limited to very superficial regions of the cortex, making it impossible to investigate behaviours in deeper tissues using current technologies.

In previous studies, microbubbles under sonication have been observed *in vivo* outside the brain in very thin and transparent organs, such as mesentery (Chen et al. 2011) and caecum (Caskey et al. 2007), and in the chorioallantoic membrane of chick embryos (Meijlink et al. 2021). These tissues are used because of their high optical transparency, enabling ultra-high frame rate bright field microscopy of microbubbles within microvessels. However, these tissues are very different to the microvasculature of the brain, and it is therefore difficult to tell how relevant they are to brain therapies (Abbott et al. 2010).

Studying the behaviour of brain cells can be performed using isolated cell cultures. These have formed the basis of various *in vitro* BBB models. These models vary in complexity, often incorporating only a brain endothelial cell monolayer on a microfluidic device (Lelu et al. 2017), although many more complex models also include pericytes, astrocytes (or a substitute cell type) and even neurons (Lyu et al. 2021; Sivandzade and Cucullo 2018; Wang et al. 2016). While *in vitro* BBB models may be useful to investigate the biology of BBB opening, they cannot replicate the full biological environment, and a flat layer of cells is a poor approximation to the confined physical environment of the brain microvasculature, meaning microbubble behaviours may be very different.

*Ex vivo* brain slices obtained from rats or mice are a common tool which have been used to investigate neurophysiology for many decades (Dingledine et al. 1980). By sectioning the brain into thin (typically 200-400  $\mu\text{m}$  thick) slices, cells can be patched or imaged with either brightfield or fluorescence microscopy. If obtained rapidly post-mortem, the tissue can be kept alive and functional in growth medium for several hours. Juvenile slices in particular have very high viability

after sectioning. Acute slices are valuable in comparison to cultured cells as they preserve local tissue structures, enabling interactions between cells to be investigated in a physiologically relevant environment (Papouin and Haydon 2018). They also enable investigation of any region of the brain, not just the edge of the cortex as in *in vivo* intravital microscopy studies.

While slices have mainly been used to investigate neuronal and glial activity, a small number of studies have used slices to investigate the BBB, and have demonstrated that the BBB can remain intact in slices. Because the vessels at the edge of the slices have been severed, transport of markers into the vessels of acute slices cannot be reliably investigated by simply immersing the slice in a medium containing the markers. However, by microinjecting dyes into vessels or nearby, transport in and out of vessels can be observed (Kovacs et al. 2011; Nuriya et al. 2013).

### **3.1.2 Aims and outline of study**

This chapter aims to understand the different ways microbubbles behave within, and interact with, brain tissue. This is achieved through observing and analysing microbubble behaviours in the microvasculature of living brain tissue while exposed to ultrasound.

Because of their high viability, transparency and biological relevance, acute brain slices were chosen as the tissue model. Methods of introducing microbubbles to the brain slices were investigated, as well as how appropriate the slices were as a model system. The slices were exposed to ultrasound pulses typical of those used in BBB opening, in terms of centre frequency, peak negative pressure and pulse length, while imaged using high-speed brightfield microscopy at two different frame rates, capturing microbubble dynamics at microsecond time scales (over individual acoustic cycles), and at millisecond scales (over 10 millisecond tone bursts). Bubble oscillations and translational movements were investigated, as well as physical effects on the tissue such as structural changes and deformations.

## **3.2 Methods**

The overarching aim of this set of experiments was to develop methods to observe microbubble dynamics in brain microvessels, and then use the methods to investigate their behaviour and effects on the tissue. This may inform our understanding of the mechanisms of therapies, especially BBB opening.

Significant development took place on these methods over the course of the experiments. Firstly, the value of acute slices as a platform was investigated, in terms of image quality (optical transparency), and viability. Secondly, an effective method was developed to reliably introduce microbubbles to the slices at appropriate concentrations. An optical setup was constructed to generate high spatial and temporal resolution images of microbubbles within brain microvessels, with good image contrast of the bubbles and vessels. Once microbubbles could be reliably observed in brain microvessels, the microbubbles were imaged using high-speed microscopy over a wide range of time scales, while exposed to typical therapeutic ultrasound pulses, to observe their physical effects on the brain tissue.

### **3.2.1 Preparation of slices**

Experiments on rat pups were limited by our Home Office Project Licence, which does not cover rats, and so no regulated procedures could be performed. Wild-type animals were therefore used for tissue, having been culled, and all experiments were performed on carcasses.

Wild-type Wistar IGS rat pups, postnatal day 5 – 15, were euthanised via intraperitoneal injection of pentobarbital, followed by femoral exsanguination, in accordance with Schedule 1 of the Home Office Animals (Scientific Procedures) Act 1986. All animals were acquired from Charles River. Shortly (< 15 minutes) after cessation of circulation, the carcass was transcardially perfused with 3-5 ml of a concentrated solution of microbubbles (40% v/v, approximately  $10^8$ /ml) and heparin sodium (0.05mg/ml). For many studies, either Evans Blue (4% w/v) or Blue India ink (40% v/v) was also

incorporated into the solution, to delineate the blood vessel lumens more clearly. The microbubbles used were SonoVue™ (Bracco, Switzerland), which is a clinically approved ultrasound contrast agent, comprising a lipid shell and sulphur hexafluoride core. SonoVue™ was chosen as it is used in several clinical trials for BBB opening in Europe. It also has a much higher average size than the in-house manufactured bubbles used in Chapter 2, making the bubbles easier to identify against a complex tissue background. The size distribution of SonoVue was measured optically using brightfield microscopy and a Matlab script (Sennoga et al. 2010), and is shown in Figure 3.1. The mean radius of bubbles (excluding bubbles  $< 0.3\mu\text{m}$ , and  $> 5\mu\text{m}$  in image post-processing) was measured at  $1.84 \pm 0.83\mu\text{m}$ , which is similar to published values (Schneider 1999).

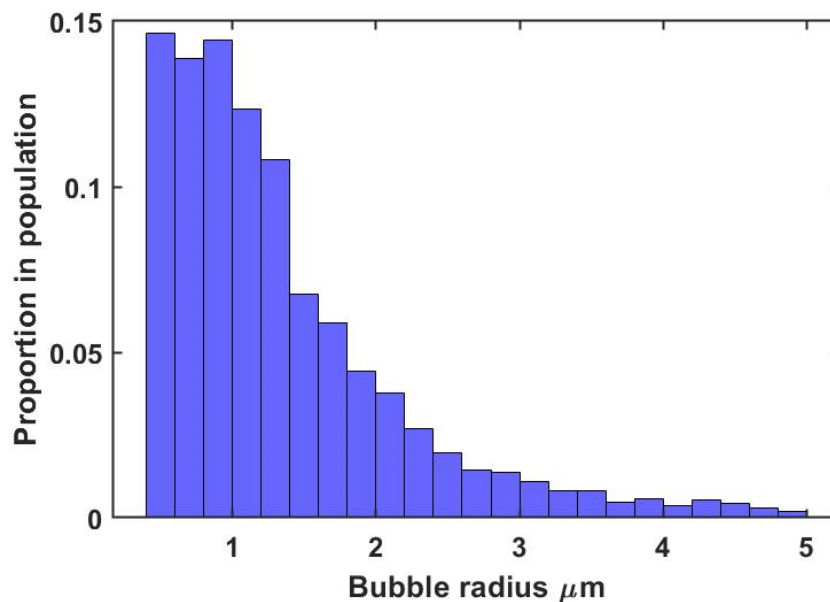


**Figure 3.1:** Size distribution of SonoVue, measured optically using the technique described in Chapter 2

Post-mortem perfusion was chosen as this was not a Home Office regulated procedure when performed on a carcass. For the purposes of this study, where we were investigating single bubbles found within each slice, a perfect perfusion of the whole brain was not critical, provided most of the tissue was reasonably well perfused, and several suitable vessels could be found in each slice.

After perfusion, the brain was then removed and the frontal lobe isolated. The frontal lobe was sectioned into 250- $\mu$ m-thick slices with a Leica 1000 vibratome and a steel razor blade (Campden Instruments), having been fixed in place with super glue.

Slicing was performed under ice-cold artificial cerebrospinal fluid (aCSF). The aCSF solution contained the following materials: 126 mM NaCl, 2.5 mM KCl, 1.25 mM  $\text{NaH}_2\text{PO}_4$ , 2 mM  $\text{CaCl}_2$ , 1 mM  $\text{MgCl}_2$ , 26 mM  $\text{NaHCO}_3$ , 15 mM glucose, and 5 mM pyruvate. Between sectioning and the ultrasound experiments, the slices were kept in aCSF at room temperature.

### 3.2.1 Microinjection of microbubbles

Several approaches were attempted to observe microbubbles in brain tissue. Firstly, the feasibility of microinjection of bubbles directly into microvessels in slices was investigated. The olfactory bulbs of rat pups were sectioned and imaged under the microscope. The olfactory bulbs were chosen because of their dense vascular network.

This was challenging due to the difficulties in inserting a glass micropipette into the microvessel, because of its relative stiffness and small size. It is also challenging to create a pipette sharp enough to penetrate the vessel, while being large enough to pass a bubble through. Microinjecting into vessels that were not very close to the surface of the slice was also very challenging, as the pipette was often blocked by passing through the upper tissue layers.

As shown in Figure 3.2, it was possible to inject dye into the vessels using this technique. However, injecting microbubbles could not be done reliably. Once the pipette had been inserted, it was difficult to inject microbubbles because of the angle of the pipette, as the bubbles float up, away from the injection site. Because of these difficulties, microbubbles were introduced to the brain via perfusion of the whole carcass before sectioning.

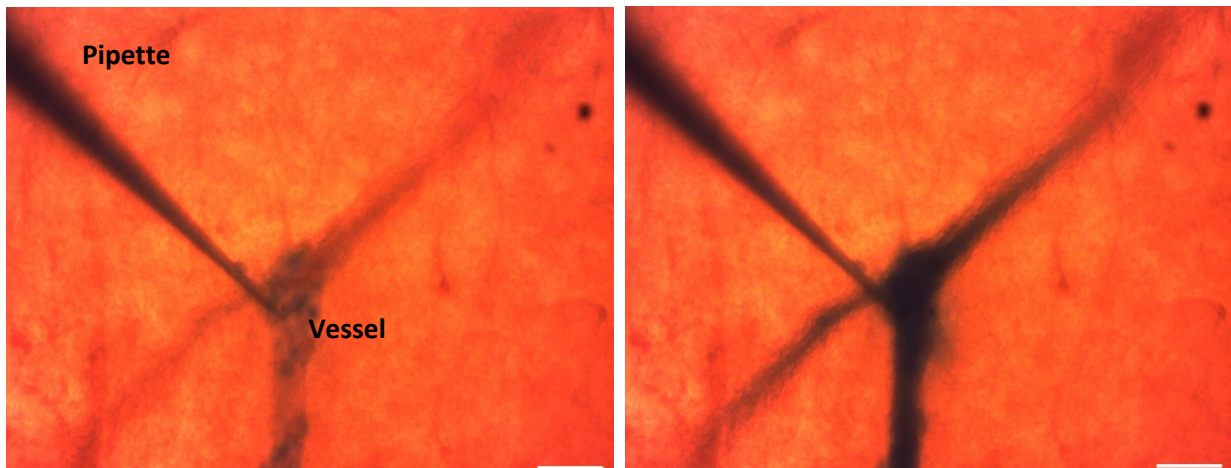


Figure 3.2: Feasibility of microinjecting a dye into a microvessel of a rat brain slice. A micropipette is inserted into a microvessel and dye is successfully injected with minimal leakage (Left: before; Right: after). Scale: 50  $\mu\text{m}$

### 3.2.2 Vessel contrast and markers of extravasation

Because the perfusion process replaced the blood with microbubbles in saline, the contrast of the vessels against the tissue background was poor. To improve this, the SonoVue™ solution used for perfusion was mixed with a coloured dye. An additional aim of this study was to assess vessel permeability in response to the microbubbles, and so the dyes had a secondary role as a marker of extravasation of vessel contents.

In order to investigate BBB disruption, it is necessary to have a reliable indicator of whether the BBB had been breached. Identifying BBB disruption *in vivo* usually involved the use of a contrast agent or dye, although several novel methods have been proposed, such as Diffusion Tensor Imaging



(Karakatsani et al. 2020) and the measurement of electrical activity across the skull (Kiviniemi et al. 2017).

Gadolinium-based MRI contrast agents are used in clinical trials and in many *in vivo* studies, as there is an immediate measurement of the degree and location of BBB opening without requiring extraction of tissue samples (Hynynen et al. 2001; Lipsman et al. 2018). In many *in vivo* studies, coloured or fluorescent dyes, such as FITC- dextran, are used (Choi et al. 2011; Pandit et al. 2020). These have a practical advantage of not requiring access to an MRI scanner.

A good dye needs to be of an appropriately high molecular weight, meaning that it will not normally pass through the BBB. Using a smaller molecule will provide greater sensitivity to BBB opening, but is not valuable if the aim is to identify whether proteins will pass through. Another consideration is the tendency of molecules to bind to plasma proteins such as Albumins, which account for approximately 50% of all blood proteins. A molecule that binds very strongly may not have a high enough free concentration to pass through the BBB unless it is also permeable to proteins more generally (Saunders et al. 2015).

For the purposes of this study, two dyes were chosen for investigation: Evans Blue (4% w/w) and Blue India Ink. Evans Blue was selected as it is a well-established method of tracking BBB permeability. Evans Blue is cheap, relatively non-toxic, highly water soluble, and its rich blue colour is very obviously visible to the naked eye, giving a clear indication of dye distribution in sectioned tissue without needing fluorescence microscopy or other advanced equipment which was not available in the experimental setup.

However, Evans Blue has several disadvantages. It has high albumin-binding affinity, meaning high concentrations are required to ensure that there are free Evans Blue in the plasma. It is also alkaline and binds to acidic parts of cells, staining the nucleus in particular (Saunders et al. 2015).

Unwanted staining of regions of the slice beyond the vessels was found to be a persistent problem, degrading the quality of images and vessel contrast, and so an alternative dye was chosen. Blue India Ink was used as it does not stain tissues, and free ink released onto the surface of the slice during sectioning can be washed off easily. India ink is a colloidal suspension of fine soot (carbon particles) in water. The range of particle sizes is extremely wide, meaning it is not a reliable indicator for a size threshold of BBB opening.

One issue to address is the osmolarity of the vessel contents. Because very high concentrations of dye were needed, it was likely that the osmolarity of the vessel contents would no longer be perfectly isotonic. As mentioned in §1, introduction of a hyperosmolar fluid to the vessels can in itself open the BBB, and potentially damage the blood vessels.

We can estimate the osmolarity of a 4% Evans Blue solution, based on its Relative Molecular mass of 981. The molar concentration was therefore 30 mM. When dissolved in water, each molecule releases 4 Na<sup>+</sup> ions, giving an osmolarity of 150 mOs. This compares to the Osmolarity of a 0.9% NaCl solution, used because it was isotonic, at 300 mOs. While dissolving Evans Blue in saline would increase its osmolarity, it would not do so dramatically. Mannitol for instance usually needs to increase the intravascular osmolarity to about 600 mOs in order to disrupt tight junctions (Högman et al. 2002).

Because India Ink is made up of carbon particles of widely varying sizes, it is difficult to estimate the osmolarity. However, its particulate nature likely suggests that it is hypotonic compared to saline, as most of the particles were not dissolved, but are merely suspended.

Because the slices were thin and placed in an isotonic bath, we expect minimal effects on the overall tissue due to the osmolarity of the vessel contents. When perfused slices were left for several hours without ultrasound exposure, extravasation was minimal. However, the unknown osmolarity of the vessel contents does place questions on the utility of the present setup for monitoring small or gradual extravasation of dye, and this is something that may need refinement in future studies, to

ensure the overall osmolality of the perfusate was isotonic. This should be tested directly with an osmometer.

### 3.2.3 Ultrasound experiments

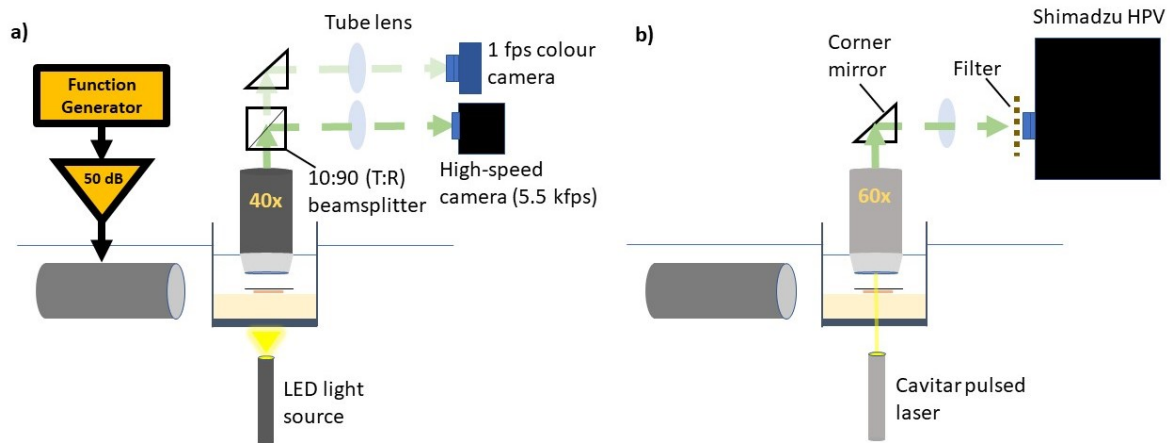


**Figure 3.3:** Experimental setup for the slice experiments. a) Setup for 5.58 kfps imaging with parallel colour camera, illuminated with an LED gooseneck light. b) Ultra-high speed imaging apparatus using a single 10 Mfps camera, illuminated with a pulsed laser.

The experimental setup was similar to those used in Chapter 2, and was shown in Figure 3.3. Instead of a 3D-printed scaffold containing polyacrylamide, the slices were placed in a perspex box, 2 cm deep (in the direction of wave propagation), 3 cm in vertical height, and 5 cm in diameter, with thin mylar windows on the sides parallel to the direction of ultrasound propagation. The box was filled with aCSF, which was kept separate from the rest of the water tank by the height of the box. The slices were placed on a bed of 1% agarose, around 5 mm thick. This kept the slice in the centre of the box and further from the solid perspex at the base of the box which may reflect sound or create standing waves, causing uncertainty in the pressure values or ultrasound propagation direction. Agarose was chosen due to its acoustic and optical transparency, ease of preparation, and low toxicity. At the bottom of the box, a window was cut out of the Perspex and a glass cover slip glued on top, allowing a clearer path for light to travel.

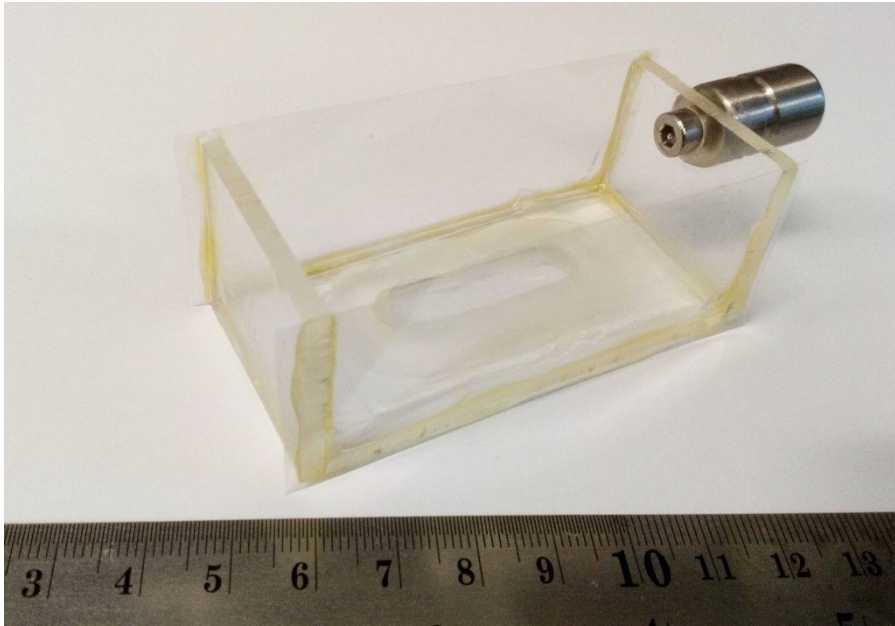
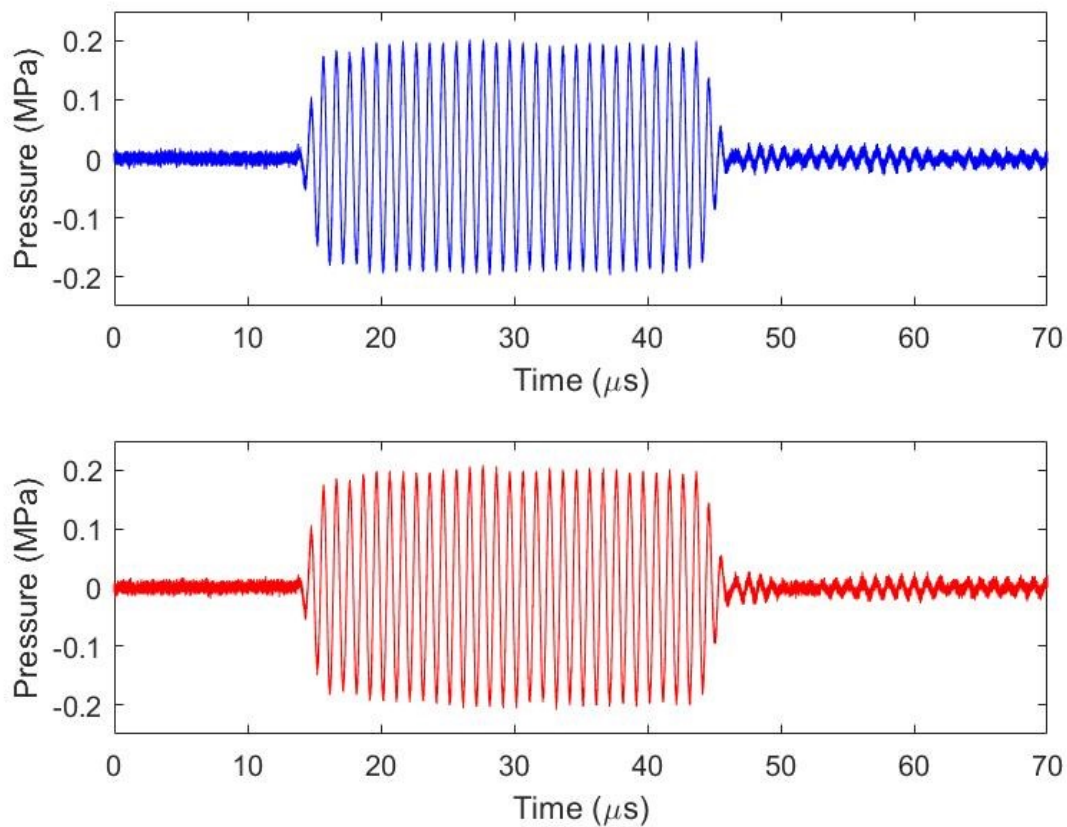


Figure 3.4: Chamber used for slice experiments, constructed of three pieces of Perspex with mylar sides. A cover slip is glued over the bottom to increase the passage of light through. During experiments, a layer of agarose is placed at the base of the chamber

The pressure under the lens was calibrated in the same manner as shown in section 2.2. After all experiments were completed, a small hole was created in one side of the mylar, to allow the hydrophone to pass through, and be placed on top of the agarose at the same position as the slice. This enabled true *in situ* pressure measurements to be compared with those acquired in that location without the slice box. As shown in Figure 3.5, the pressure compared to the values acquired without the box was the same, to within the level of noise. The shape of the reflected pulse present after the main pulse was very slightly different, although in both cases this was less than 10% of the initial pressure amplitude. This indicates that, while reflection or standing waves may have been present in the much longer pulses, their amplitudes are likely to be considerably lower than the primary incident wave.



**Figure 3.5:** Pressure calibration taken without (blue) and inside (red) the slice box. The pressure amplitudes are indistinguishable, showing negligible attenuation of the ultrasound by the mylar box. There are some slight differences in the shapes of reflected pulses afterwards. This figure also highlights the rapid ramp-up time of the transducer, and stable maximum signal amplitude.

### 3.2.4 Optics — High-speed imaging

The apparatus used to observe microbubbles over millisecond time scales was similar to that used in §2, with the same objective lens and Chronos 1.4 high-speed camera. Several key modifications were performed, however. The 90° lens was replaced with a 10:90 (Transmit:Reflect) beamsplitter, with 90% of the light from the sample being sent to the high speed camera. 10% was sent through to a 90° mirror and second tube lens, to a lower frame rate (1 or 20 fps) colour camera. This was used to provide good image contrast of the blue dye in the vessels, and of the microbubbles relative to other structures. The colour camera enables more reliable identification of bubbles from similarly sized

and shaped objects such as red blood cells. It also enables acquisition of clearer images of dye leaving the vessels. Videos were acquired at 1 fps, starting shortly before the pulse and for 1 minute after, although some were recorded at 20 fps, to provide better tracking of the timescale of bubble dissolution after the pulse. Two colour cameras were used, initially a ThorLabs DCC1645C CMOS camera, and then an IDS U3-3070CP CMOS, the latter offering superior light sensitivity, resolution and resilience to background motion artifacts due to its global shutter.

The Chronos 1.4 camera captured videos at 5,480 fps for 150 frames. This gives a total recording time of 27 ms. The Field of View was 608x400 pixels; with the pixel pitch of 0.16  $\mu\text{m}$ , this equates to 97x64  $\mu\text{m}$ . These parameters provided an optimal balance between frame rate, image quality and field of view.

### 3.2.5 Optics — Ultra-high-speed imaging

In order to image bubble volumetric oscillations, much higher frame rates are required, significantly in excess of the ultrasound driving frequency. To achieve this, an HPV-X2 (Shimadzu, Kyoto, Japan) ultra-high-speed camera was used. The Shimadzu can record at either 5 Million fps or 10 Mfps for 256 frames. This gives either 5 or 10 frames per acoustic cycle at 1 MHz, significantly above the Nyquist sampling threshold, and thus enabling a general trend in bubble radius to be measured over each pulse. This includes enabling a good estimate of the maximum radial expansion of the bubble, as well as observing any shape changes of the bubble. The camera has a fixed Field of View of 400x250 pixels. The optical setup gives a pixel pitch of 0.61  $\mu\text{m}$ , and thus a FOV of 244x153  $\mu\text{m}$ .

A pulsed laser (CAVILUX Smart, Cavitar, Tampere, Finland) was used for illumination instead of the LED light source. The laser emits 640 nm wavelength, 10 ns duration laser pulses synchronous with the camera. This pulse length determines the exposure time of each frame, as it is much shorter than the exposure time of the camera.

The beamsplitter was removed from the previous optical setup, ensuring all the light passed into the camera, but losing the simultaneous colour imaging. A filter was placed in front of the camera sensor. The 40x lens was replaced with a 60x lens to improve the spatial resolution.

### 3.2.6 Analysis of videos

For the ultra-high speed videos, the diameters of the vessels were measured manually by three independent observers using Fiji (Schindelin et al. 2012). The initial, final, maximum and minimum diameters were measured, and the uncertainty in these measurements was taken as either the range of the three measurements or the pixel pitch, whichever was greater.

In addition to the displacement of the walls at microsecond timescales, bubbles also caused displacement of the surrounding tissue. This was analysed using digital image correlation, to measure the magnitude and direction of tissue motion. This was mainly performed to track deformations across the 10 ms tone bursts, as the tissue background was clearer than in the ultra-high frame rate images

Open source software (Ncorr) was used (Blaber et al. 2015), which compares two chosen frames to determine sub-pixel resolution material deformation across a chosen region of interest using 2D cross correlation. Two frames were chosen in each video, an image before the start of the pulse, and one at the maximum deformation.

### 3.2.7 Tissue viability assay

One of the key advantages of using acute brain slices is that the tissue can be kept alive for several hours outside the body. While the present study is mostly focussed on observing physical responses, meaning phenomena such as neuronal activity are less critical than electrophysiological studies

involving patching, for instance, it is still valuable to investigate how viable the tissues are during the video recordings. Living tissue may have different physical properties to inactive tissue, for instance, and this also helps to investigate the future potential of this technique in investigating biological effects of microbubbles.

The approach taken here was to use 2,3,5-Triphenyltetrazolium chloride (TTC) staining. TTC is a marker for cellular respiration within cells. TTC acts as a proton acceptor for pyridine nucleotide-linked dehydrogenases that form a part of the electron transport chain in the mitochondria. The tetrazolium salt is reduced by the enzymes into a red, lipid-soluble formazan. This stains viable tissue deep red, and is commonly used to identify infarcts in brain slices (Joshi et al. 2004). This technique is convenient as results are obvious by eye and can be imaged immediately without requiring a fluorescence microscope.

The slices were prepared in the same way as those used in the optical experiments. Three different groups of 5 samples from the same animal were obtained, with each sample being one slice from one hemisphere. All 5 slices of each were kept in the same dish containing 5 ml of medium.

A positive control was obtained of tissue stained shortly after sectioning. This correlates with the start of the experimental time. A second set of samples were maintained at room temperature in 5 ml of aCSF, open to room air, for 2 hours. This corresponds to the end of the period of optical experiments. A negative control was also obtained of samples kept in 5 ml of PBS for 2 hours with the solution covered.

At the appropriate point, the slices of each set were placed in a 5 ml dish of 0.05% TTC dissolved in PBS and incubated at 37°C for 30 minutes. The slices were then washed three times in PBS and fixed in 4% formaldehyde in PBS for 1-2 hours.

Images of the slices were obtained using an RGB camera attached to a stereo microscope (StereoBlue, Euromex, The Netherlands), while lit from above the sample. The slices were all imaged



within 1 hour of fixation, and the magnification and light settings on the microscope remained constant throughout. The staining intensity remains constant for several days after fixing, and so a variation of a few hours should not cause major variation in staining intensity (Joshi et al. 2004).

For each of the images, the cortex was manually segmented using ImageJ, and the intensity of the red staining was compared between the three sets of samples. This was performed in Matlab, by converting the image from RGB (Red, Green, Blue) to HSV (Hue, Saturation, Value) format, and comparing the saturation values across the three different sets of samples. The standard deviations of the saturation values within each slice were also compared to evaluate how evenly the tissues were stained, indicating whether some regions were more or less viable than others.

### 3.3 Results

#### 3.3.1 Feasibility of direct observation of microbubble dynamics in acute brain slices

Before investigating the response to ultrasound of microbubbles in brain slices, the effectiveness of the experimental approach described above in generating high quality images of microbubbles in intact vessels was investigated. The method of introducing microbubbles to the slices was assessed, as well as the utility of the slices as a way of observing microbubbles, and the ability of the optical setup to image microbubbles clearly at high frame rates.

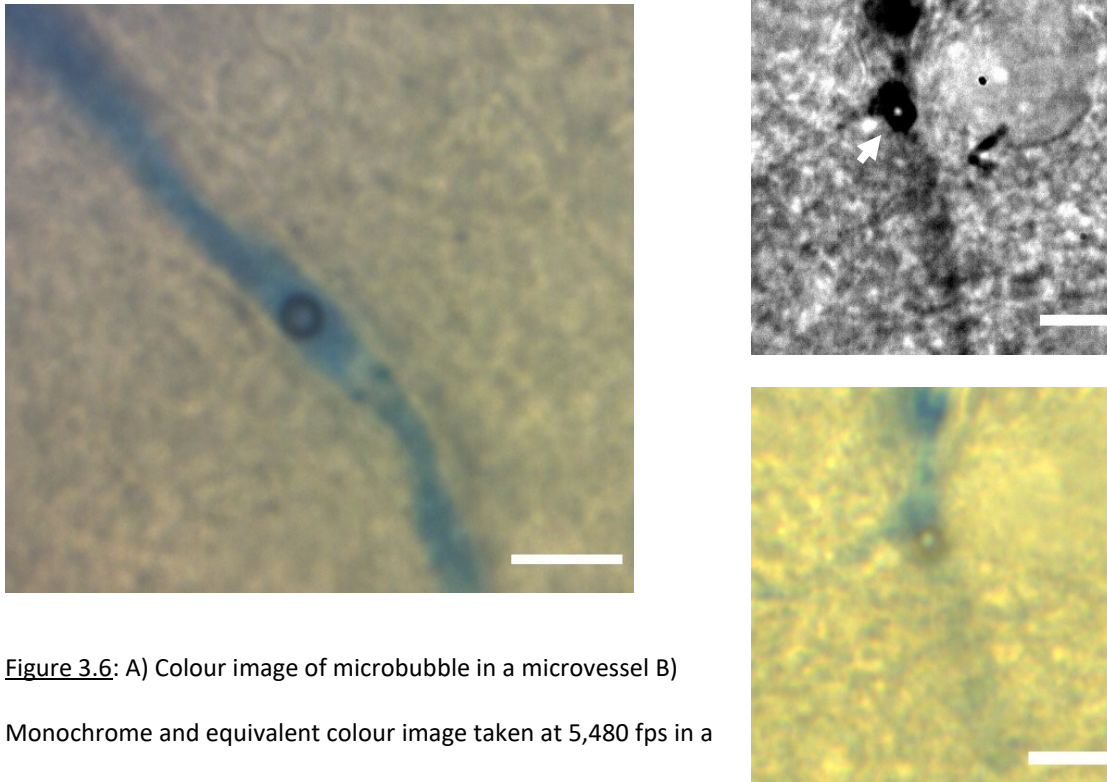


**Figure 3.6:** A) Colour image of microbubble in a microvessel B) Monochrome and equivalent colour image taken at 5,480 fps in a different slice. Scale: 10  $\mu$ m

To clearly observe bubble dynamics, it is important to be able to image microbubbles with good contrast against the tissue background. Figure 3.6 shows an image taken at 5,480 fps using the monochrome high-speed camera. The microbubble is highlighted. In this image, the microbubble is very clear against the tissue background, and can be easily identified by its characteristic circular shape, dark halo, and bright spot in the centre. The presence of the dye also aids clear visibility of the vessels. Other tissue structures can also be identified.

However, in some videos, the bubbles were less obvious. Sometimes this is because the bubbles are deeper in the tissue, and therefore can be seen less clearly. In other videos, the presence of the dye obscures the edges of bubbles making them harder to identify. In some instances, on the monochrome camera, it is difficult to conclusively identify a microbubble from other objects, such as red blood cells.

The addition of the colour camera overcame many of these problems. Figure 3.6 also shows an example colour image of a microbubble in a brain microvessel. The bubbles can be clearly distinguished from the dye and from red blood cells by their colour.

The in-house manufactured microbubbles used in Chapter 2 were tested as part of the perfusion. However, their very small average diameter ( $<1\ \mu\text{m}$ ) meant that most of the bubbles were very difficult to observe against the complex tissue background, and it was difficult therefore to identify single bubbles. In all of the results presented here, SonoVue was used instead, which has a much larger mean diameter of around  $2.5\ \mu\text{m}$  (Schneider 1999).

Several different microbubble concentrations were attempted. At first, a typical clinical concentration was used ( $2 \times 10^6$  microbubbles/ml) (Pouliopoulos et al. 2020a). However, no microbubbles could be found in most slices. When completely undiluted SonoVue was used (around  $2\text{--}6 \times 10^8$ /ml), many microbubbles could be found in the slice, but it was common to find bubbles in clusters or very close to each other. A final concentration of 40% SonoVue by volume provided a good distribution of microbubbles, with a selection of well isolated bubbles in almost every slice.

Some trial experiments were conducted in mice brain slices, and in hippocampal slices of rat pups, but these were less effective due to the opacity of the tissue. Cortical slices of rat pups were therefore used for the results presented here.

These results demonstrate that acute cortical slices from perfused juvenile rats offer a reliable method to create high resolution brightfield images of microbubbles in the microvasculature of the

brain, with good contrast between the bubbles, vessels, and surrounding tissue. Microbubbles can be introduced reliably, and at an appropriate concentration and distribution to enable single bubbles to be identified as suitable for imaging in almost every slice.

### 3.3.2 Microsecond time scales

Once a reliable method of introducing microbubbles to the slices had been developed, microbubbles in slices were observed at 10 Mfps for 256 frames. This frame rate is high enough to observe their oscillations over an acoustic cycle, when driven with 1 MHz ultrasound, as well as observing periodic behaviour over several successive cycles.

#### Microbubble volumetric oscillations

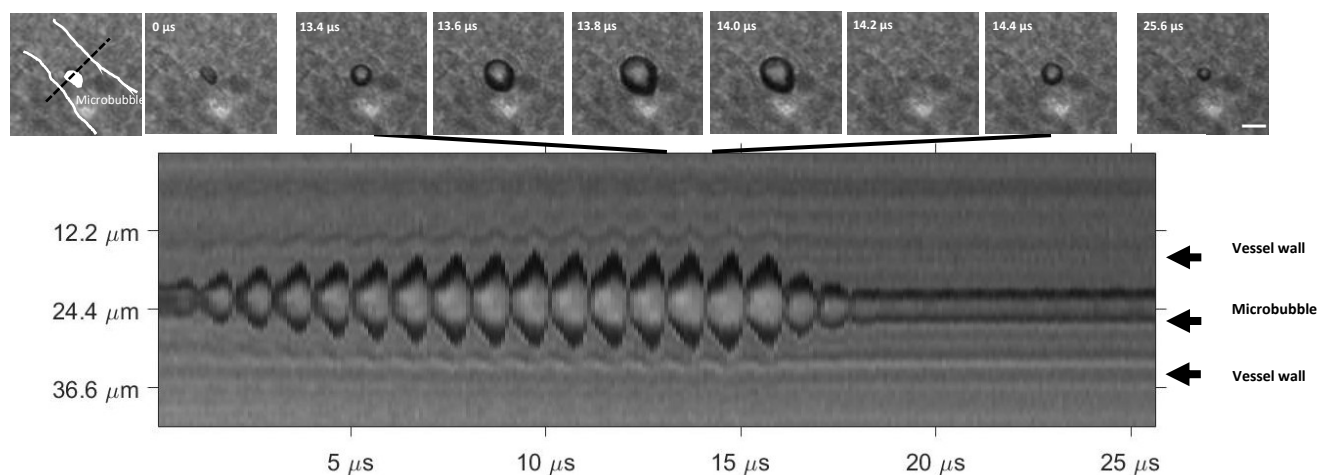


**Figure 3.7:** A microbubble in a microvessel, exposed to an 800 kPa, 1 MHz, 15 cycle pulse and imaged at 10 Mfps. The vessel walls oscillate with the bubble. The bubble oscillations are not temporally symmetric throughout the pulse, with a much longer expansion phase than collapse phase. The smallest size the bubble reaches is too small to be resolved by the camera used here as shown in the image at 14.2  $\mu\text{s}$ . The streak image below is taken along the dotted line

Microbubbles were exposed to a 15 cycle ultrasound pulse and imaged at 10 Mfps. Microbubbles in cortical microvessels exposed to ultrasound expand and contract in response to the ultrasound pulse (Figure 3.7). These oscillations caused the vascular wall to move at the same rate as the bubble

oscillation. It is likely that the surrounding liquid was being displaced by the bubble oscillations, although the nature of this motion could not be resolved in the images.

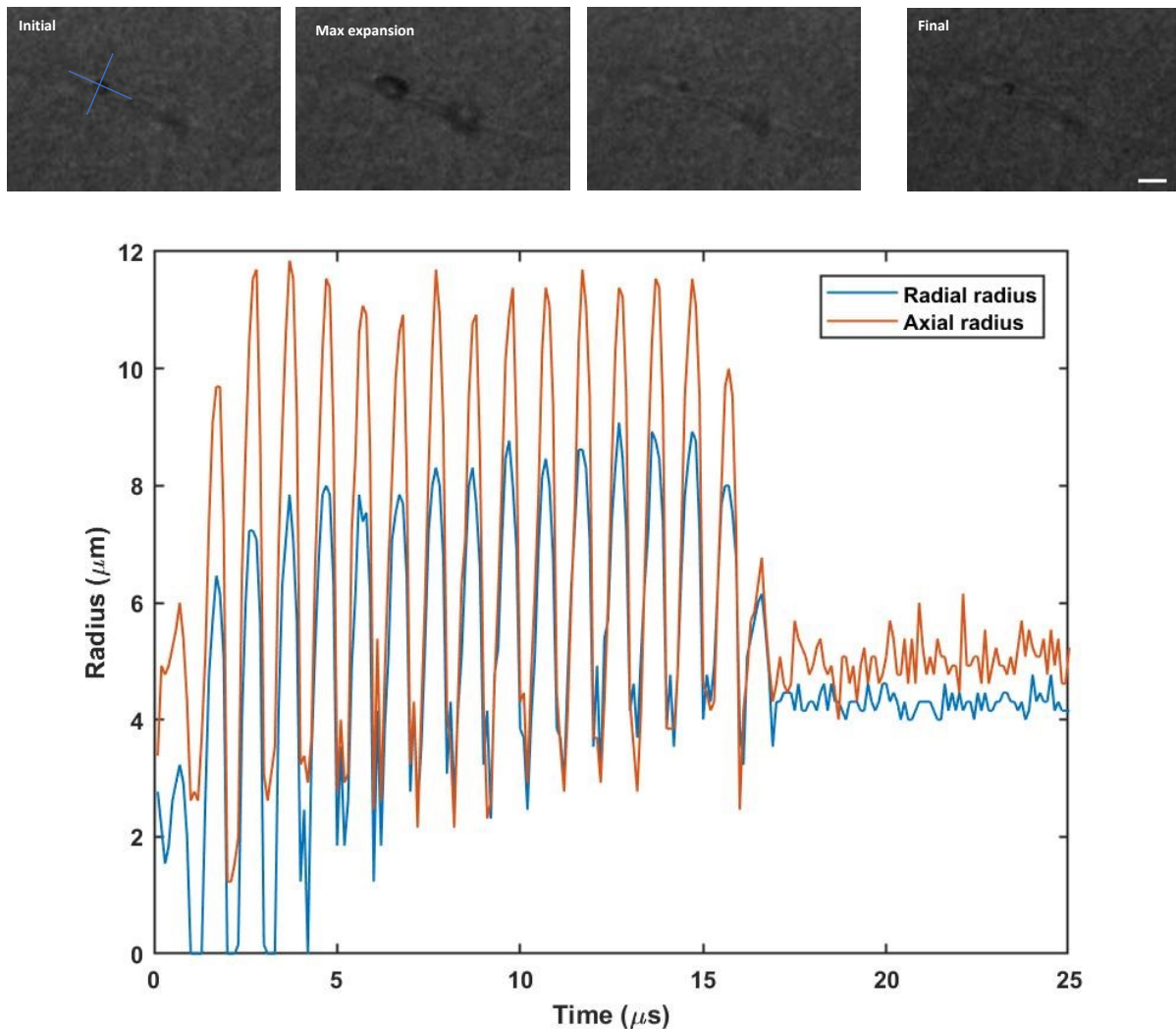


**Figure 3.8:** Asymmetric oscillations of a microbubble in a small microvessel. A) 4 example frames of bubble showing asymmetric oscillations within a microvessel. Scale = 10  $\mu\text{m}$  B) Radius-time curve of the bubble in A along (red) and perpendicular to the midline of the vessel.

At very high frequencies, the mechanical properties of vessels are unclear, but these observations demonstrate that the vessel wall remains sufficiently elastic to oscillate periodically over microsecond timescales. In the example shown in Figure 3.7, a microbubble with a diameter of approximately 5  $\mu\text{m}$  was found in a microvessel with a diameter of  $16.7 \pm 0.6 \mu\text{m}$  was exposed to a 0.8-MPa pulse. Distension was greater than invagination: the maximum and minimum vessel

diameters after 10 cycles of oscillations were  $19.4 \pm 0.6 \mu\text{m}$  and  $16.2 \pm 0.6 \mu\text{m}$ , respectively. The vessel diameter at the end of the recording, shortly after the end of the pulse was  $16.9 \pm 0.9 \mu\text{m}$ ; in comparison with the initial diameter, the ranges overlap significantly, showing the vessel has not changed diameter by a significant amount. The uncertainty in these measurements is the standard deviation of the three values measured, or the pixel pitch, whichever was larger.

When confined in small microvessels, microbubbles often oscillated asymmetrically. For instance, several examples were observed of microbubbles expanded in an ellipsoidal shape, with more expansion along the axis of the vessel than radially. This was most commonly seen when bubbles were quite close to another bubble in the same vessel. In one example, the vessel experienced a min to max diameter ratio of around 1.3 (perpendicular and parallel to the central axis of the vessel) (Figure 3.8). No instances of jetting (penetration of one side of the bubble through the other) were observed, as was demonstrated in previous studies in other scenarios (Chen et al. 2010; Cleve et al. 2019).

### **Microbubble extravasation**

Microbubbles are generally assumed to remain confined to the vasculature because of their size. However, here, microbubbles themselves sometimes extravasated, passing through the microvessel walls. This was sometimes associated with extravasation of the dye within the vessels (Figure 3.9A), clearly indicating a puncture to the vessel. As shown in Figure 3.9B, after leaving the vessel, microbubbles can penetrate tens of micrometres into the brain tissue.

second time scales

Microsecond time

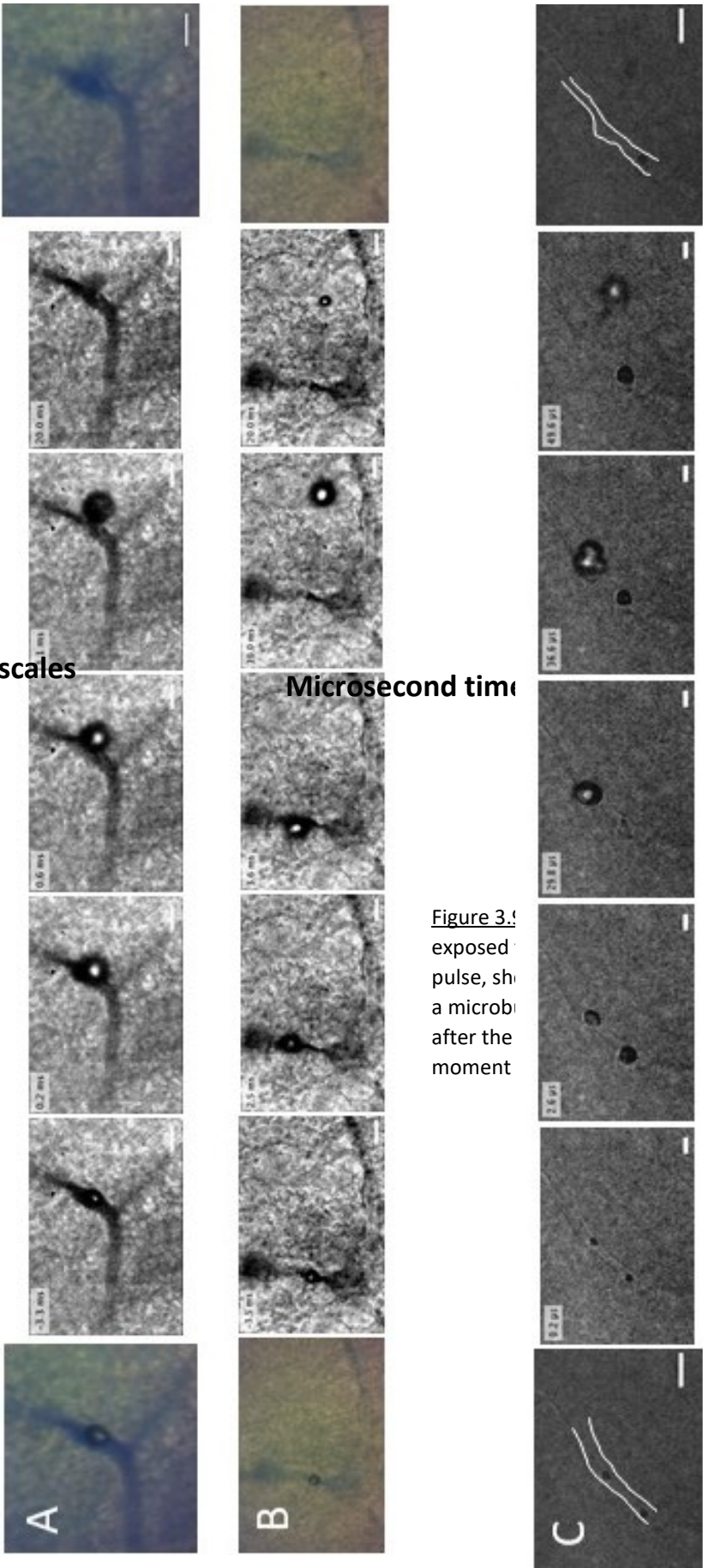


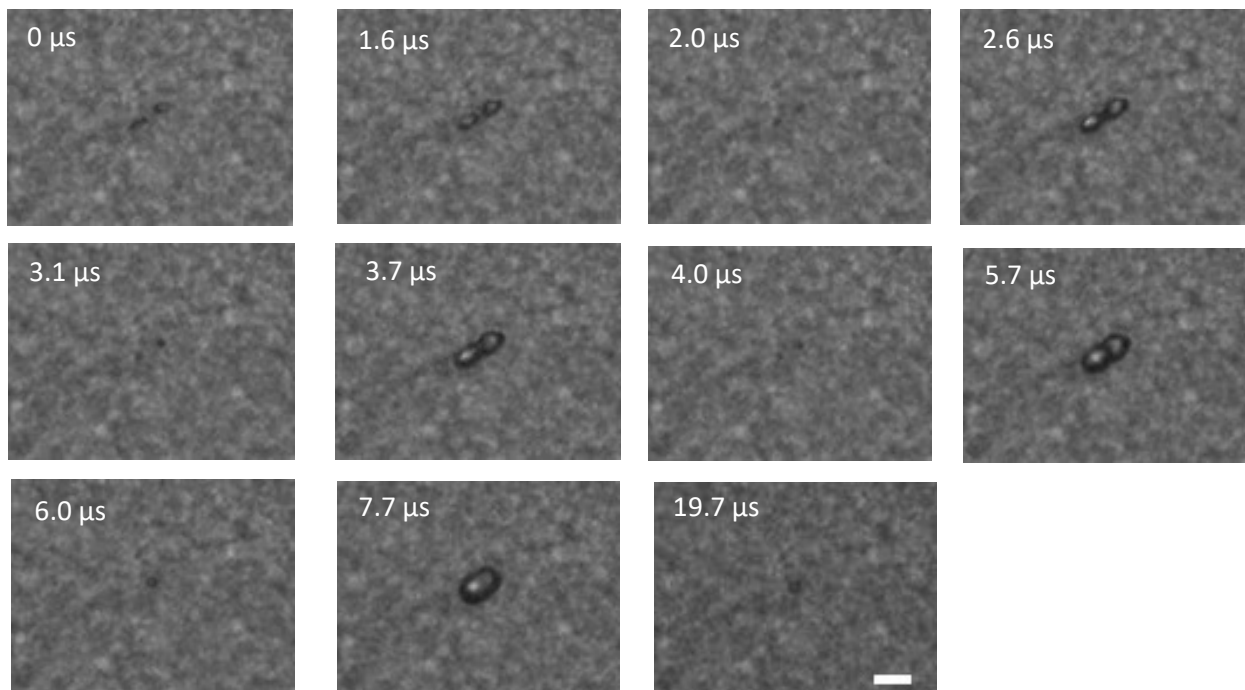
Figure 3. A) Extravasation of a microbubble from a vessel when exposed to a 1 MPa pulse. B) Extravasation of a microbubble from a vessel when exposed to a 1 MPa pulse. C) Frames of a video taken at 5 Mfps showing a microbubble interacting with a vessel when exposed to a 1 MPa pulse. The shape of the microbubble changes as it interacts with the vessel wall and is no longer approximately spherical.

Figure 3. A) Extravasation of a microbubble from a vessel when exposed to a 1 MPa pulse. B) Extravasation of a microbubble from a vessel when exposed to a 1 MPa pulse. C) Frames of a video taken at 5 Mfps showing a microbubble interacting with a vessel when exposed to a 1 MPa pulse. The shape of the microbubble changes as it interacts with the vessel wall and is no longer approximately spherical.

Extravasation of microbubbles often caused structural changes to the microvessels (Figure 3.9D).

Figure 3.9D shows the radius-time curve of a bubble exposed to a 1 MPa ultrasound pulse and imaged at 5 Mfps. Towards the end of the pulse, this bubble left the confines of the vessel. Over the first 15-20 cycles, the bubble initially oscillated with stable, moderate amplitude oscillations ( $R_{\max}/R_0$  of around 3), before gradually increasing in amplitude (up to  $R_{\max}/R_0$  of around 5) as the vessel is deformed, and the bubble completely breaks free of the confines of the vessel. The maximum amplitude of oscillation before extravasation quite closely matches the predicted maximum radial excursion of a free SonoVue microbubble exposed to these ultrasound parameters. Around the point that the bubble leaves the vessel, it becomes obviously asymmetrical (Fig 4C), showing several lobes. The bubble appears to fragment at this point, with the fragments continuing to move into the tissue. Extravasation of microbubbles is investigated in more detail in Chapter 4.

### Ultrasound-induced microbubble coalescence



**Figure 3.10:** Coalescence of two microbubbles within a small microvessel, imaged at 10 Mfps. While it is difficult to define the exact moment of coalescence, the two bubbles coalesce in less than approximately 8 acoustic cycles. Scale = 10  $\mu\text{m}$ .



While the shells of microbubbles are designed to reduce the probability of coalescence, this can still occur when bubbles are exposed to ultrasound. Several instances of microbubble coalescence in very small microvessels of brain tissue were observed here. Coalescence is very rapid, occurring over only a few acoustic cycles (Figure 3.10).

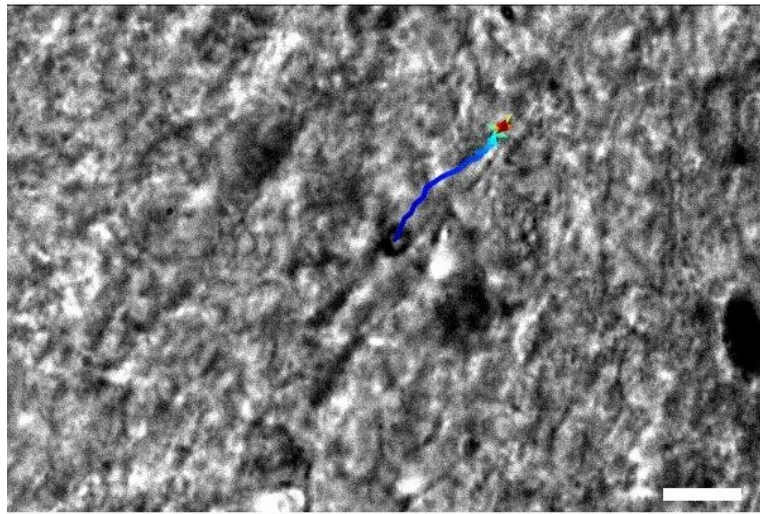
### 3.3.3 Millisecond time scales

As well as observing microbubble behaviours over single cycles, bubbles were also observed over 10 millisecond pulses. These are typical of those used *in vivo*. Over this time period, bubbles were imaged at 5,548 fps. This is too low to capture bubble dynamics over single cycles, but can capture bubble motion, fragmentation, and longer-time scale effects on the surrounding tissues.

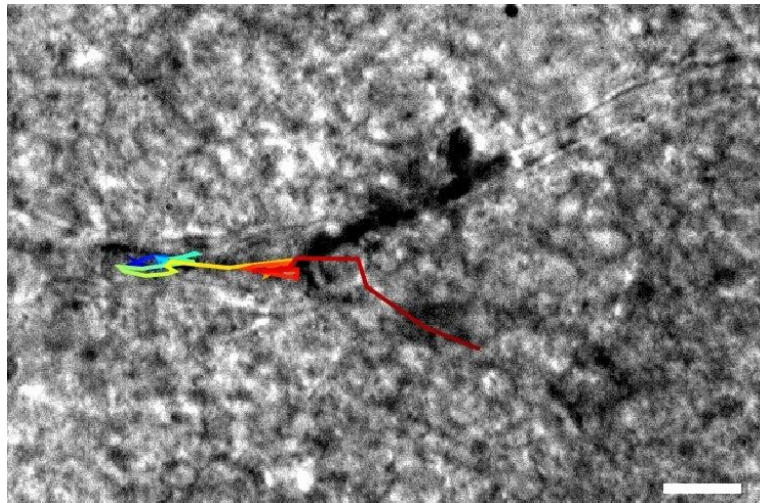
#### Motion of microbubbles within microvessels

At millisecond time scales, the primary radiation force on microbubbles is prolonged enough to generate quite significant displacements of the microbubbles, even when confined to very small microvessels. During the 10-ms pulse, microbubbles could be driven significant distances (tens of micrometres) within the vessels. The bubbles typically moved along the vessels in the direction of propagation of the ultrasound, although this motion was often highly erratic. Even when confined within vessels, microbubbles exposed to a 600 kPa pulse can achieve instantaneous speeds of up to around 50 mm/s, as measured by the distance travelled between successive frames of the video (Figure 3.11).

A



B



C

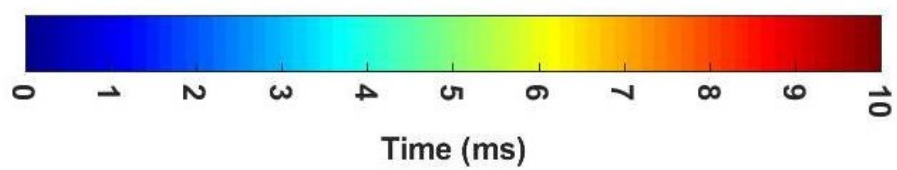
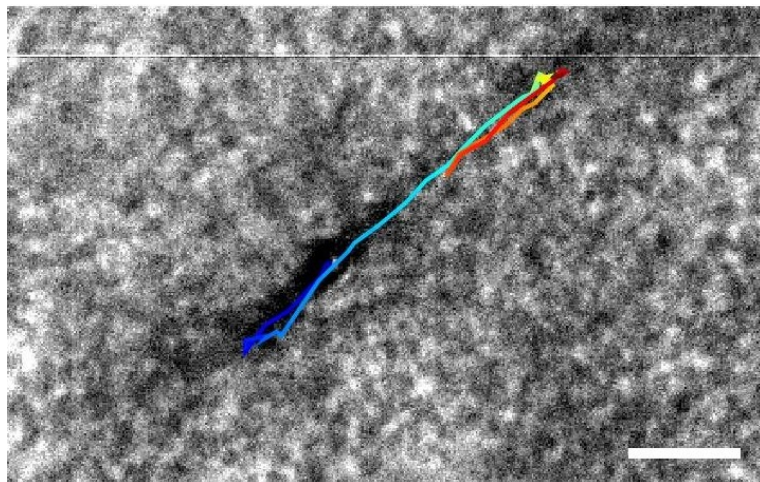
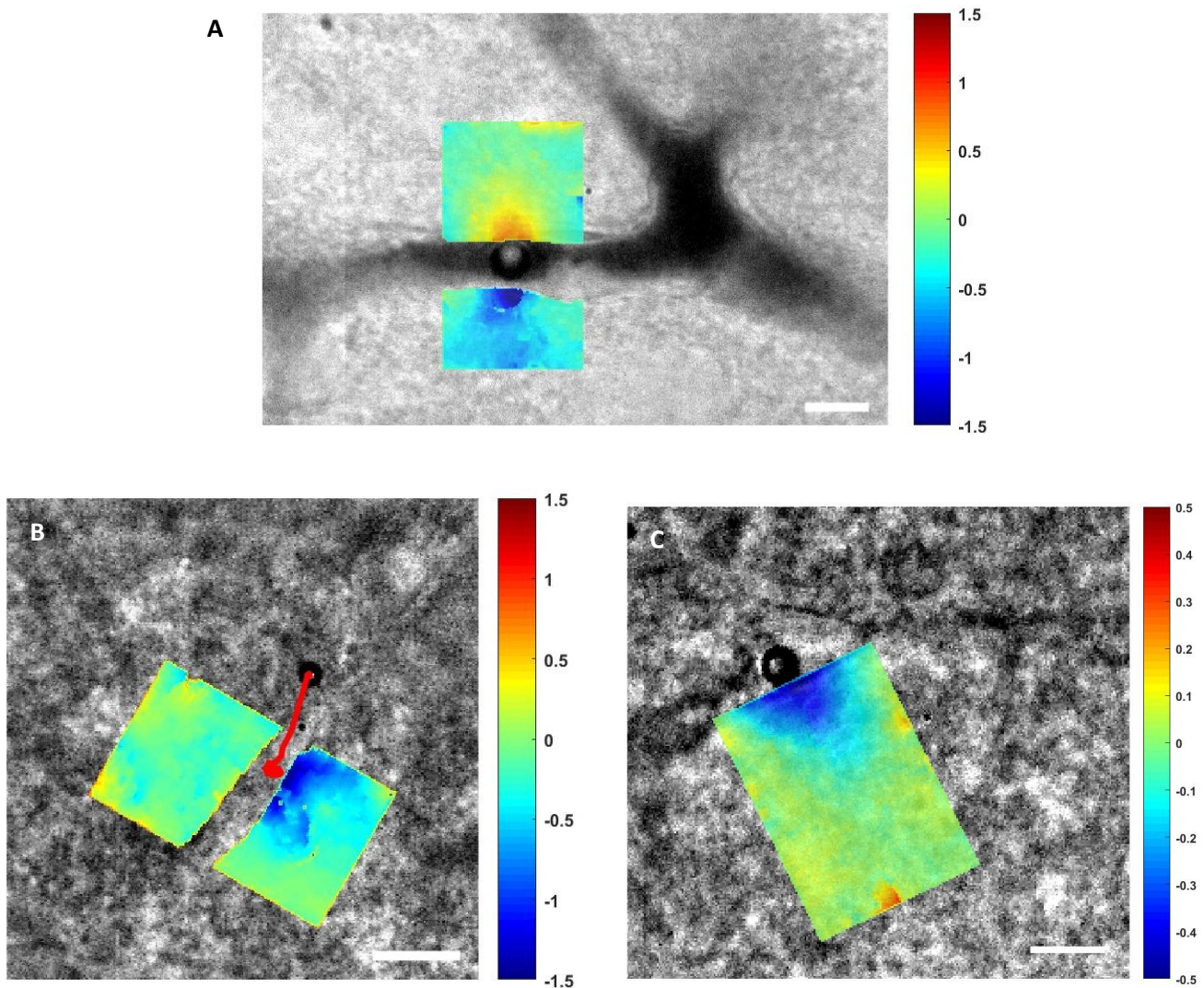


Figure 3.11: Motion of microbubbles within microvessels exposed to 10 ms pulses at different peak negative pressures. A) 400 kPa, B) 600 kPa, C) 400 kPa. Microbubbles generally move in the direction of wave propagation (Left – Right), but their motion can be very erratic. Scale = 10  $\mu\text{m}$ .

### **Tissue deformation**

In addition to the vessel wall oscillations observed at microsecond time scales (Figure 3.7), significant tissue displacements were also observed over millisecond time scales. Displacements often affected a wide range of the tissue surrounding the vessel, and were not constrained to the vessel wall. Displacements were quantified using digital image correlation (Blaber et al. 2015), by comparing the points in the tissue at their maximum displacement with an image from before the ultrasound pulse. As shown in Fig 3.12, microbubbles could displace tissue located over 5  $\mu\text{m}$  from the vessel lumen by up to around 0.5  $\mu\text{m}$ .



**Figure 3.12:** Deformation of surrounding tissues by microbubble oscillations over a 10 ms pulse. Slices were exposed to A) 200 kPa, B) 600 kPa (the red line shows the path of the microbubble during the pulse), and C) 400 kPa pulses. Even at quite low pressures, microbubbles can deform the surrounding tissue over quite a large area. Scale bars: 10  $\mu\text{m}$ . Colour bars are in micrometres, distance moved perpendicular to the vessel wall.

### Vasoconstriction

It has previously been shown that ultrasound and microbubble blood brain barrier opening can induce vasoconstriction *in vivo*. A small number of examples of vasoconstriction were observed in response to microbubbles in larger vessels. In the example shown in Figure 3.13, a relatively large



microvessel around 12  $\mu\text{m}$  in initial diameter constricts by almost 50% over a period of 20 seconds following the pulse

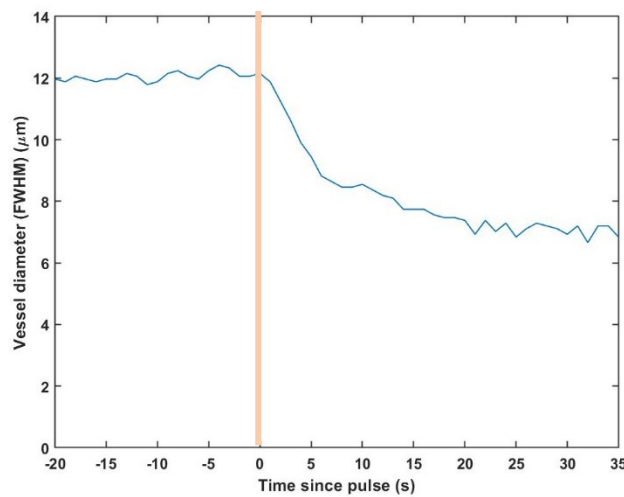


**Figure 3.13:** Vasoconstriction in a microvessel (likely to be an arteriole) after exposure to a single 600 kPa, 10 ms ultrasound pulse applied at 0 seconds (vertical line). A): frames from colour image taken (L-R) before, immediately after, and 30 seconds after the pulse. The vessel contains two large bubbles (arrows), one of which is out of the focal plane, and which both disappear after the pulse. Scale = 10  $\mu\text{m}$ . B): Vessel diameter over time, based on Full-width half maximum of the image intensity taken along the dotted line denoted in A.

### Streaming

Oscillating microbubbles have previously been shown to cause streaming of fluid surrounding them when studied in hydrogels (Jamburidze 2019). This may have implications for drug delivery by forcing fluid against the vessel walls, or improving the distribution of drugs.

Several instances of microstreaming in brain microvessels were observed in our experimental conditions. The oscillating bubble had quite a well-defined boundary of influence over which the ink circulated and was cleared after the pulse.

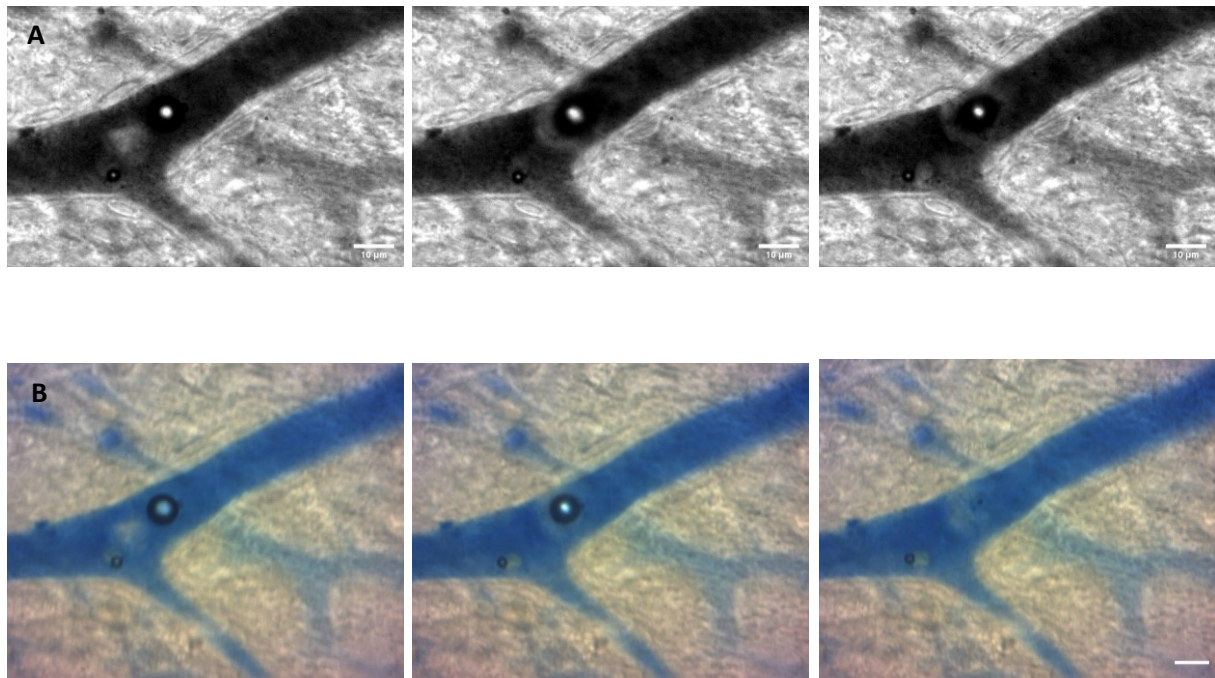


**Figure 3.14:** A) Microstreaming in a microvessel around a large microbubble. Images taken at 0, 7 and 12 milliseconds after the start of a 10 ms pulse. The microbubble oscillations disturb the distribution of ink particles nearby, but the boundary of influence is relatively well defined. B) Dissolution of the bubble after microstreaming. Images shown are (L-R) before the pulse, immediately after the pulse, and 14 seconds after the pulse (at the point the large bubble is no longer visible). Scale = 10 µm.

### Microbubble dissolution

It was very common for microbubbles to dissolve after the pulse. This typically occurred over a few hundred milliseconds for an average-sized bubble. In Fig 3.14, a large bubble is shown to dissolve over 14 seconds after the pulse. Another smaller bubble in the field of view retains its size, however.

Except at the highest pressures used here (800 kPa and 1 MPa), fragmentation of the bubbles during the pulse was very rarely observed. The primary modes of destruction were gas diffusion after the pulse, and coalescence of very close microbubbles. This is covered in more detail in Chapter 4.

### 3.3.4 Tissue viability

It is important to assess the levels of cellular activity in the slices to understand the relevance of these observations to an *in vivo* setting, and the potential for this platform to be used in future to investigate microbubble-induced bioeffects.

The viability of the slices was assessed using TTC staining, which stains tissue undergoing active aerobic respiration deep red. As shown in Figure 3.15, large regions of the slices used in the experiments are stained red, in comparison to the negative control of samples covered and kept in PBS.

Mean intensity values were significantly higher ( $p < 0.05$ ) in both the aCSF samples than the PBS sample. There was no significant difference between the samples tested immediately, and those which had spent 2 hours in aCSF. This indicates a good degree of viability of the slices at both the start and end of the recording period. However, there was variation in intensity, and small regions in most slices remained white.

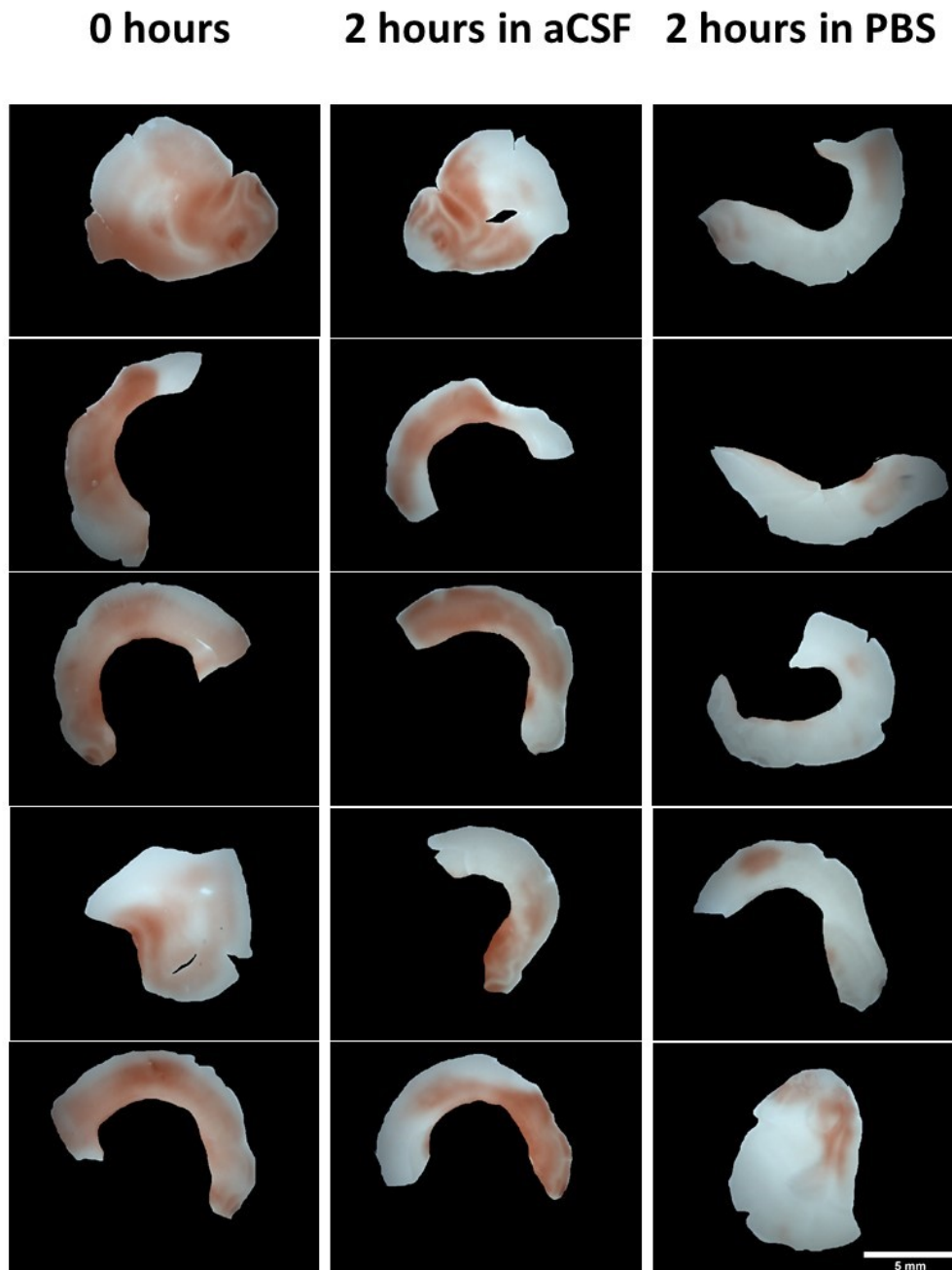


**Figure 3.15:** TTC staining results. All three groups of samples show some red staining, although this is considerably more pronounced in the 0 and 2h aCSF groups, which indicate the start and end of the typical recording periods. In both of these groups, there are regions which have not been stained, however. Scale = 5 mm



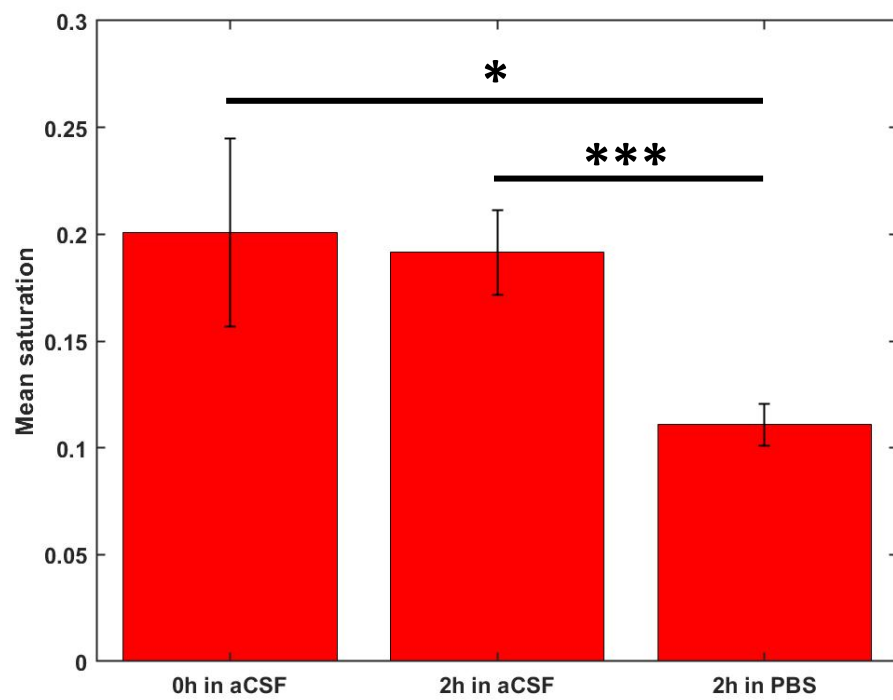


Figure 3.16: Bar plot showing mean colour saturation for the cortex of each group of TTC stained slices. Error bars are standard deviations between slices. \*  $p=0.040$ , \*\*\*  $p=8.4e-5$

### **3.4 Discussion**

This study presents direct observations of microbubble dynamics in the microvasculature of live brain tissue, at both microsecond and millisecond timescales, when exposed to ultrasound pulses typically used to deliver drugs across the BBB. These results demonstrate that microbubble oscillations within microvessels can displace surrounding tissue on both microsecond and millisecond timescales, and these displacements can extend significantly beyond the inner wall of the vessel. Additionally, the primary radiation force on microbubbles in microvessels can also be very significant, both through directly generating directional stresses on the tissues, and also by moving bubbles within vessels, enabling them to exert forces on a wider region of tissue.

While these observations are in an *ex vivo* setting, meaning firm conclusions about their relevance to an *in vivo* setting are difficult to state, the slice platform represents a valuable tool to prove high quality images of microbubbles in an environment that is likely to be more physiologically relevant than many previous published studies.

#### **3.4.1 Tissue deformation by individual microbubbles.**

Oscillating microbubbles can generate significant displacements of surrounding tissues on both microsecond and millisecond time scales. Imaging at 10 million frames per second revealed that the vessel wall oscillates with the microbubble. MHz frequency tissue movements cannot be achieved through known physiological mechanisms. However, due to the high magnitude of deformations being produced, it is worth investigating whether this behaviour could stimulate mechanotransduction pathways as has been shown directly in isolated cell cultures (De Cock et al. 2015).

Vessel distension appeared to be more significant than invagination. The vessel shown in Fig 3.7 reached a maximum diameter during its oscillations 10% larger than its initial diameter, but the

minimum diameter during this period was still very close to the initial diameter. This is in contrast to results presented previously from mesenteric microvessels, which showed vessel invagination to be especially significant (Chen et al. 2011). The difference may be due to the longer pulse lengths, lower pressures, smaller microvessels used here, or difference in tissue model.

In addition to causing vessel wall oscillations oscillating with the ultrasound cycle at MHz frequencies, microbubbles exposed to 10-ms pulses can displace surrounding tissues on millisecond time scales. Imaging at 5,481 fps revealed displacement of tissues well beyond the vessel boundaries. Thus, while the focus on mechanisms have previously focused on the tight junctions, endothelial cells, and other vessel wall features, it is plausible that mechanical stimuli may be elicited in other surrounding regions.

In most cases, deformations generated in the tissue by microbubbles relaxed rapidly at the end of the pulse. However, as shown in Figure 3.12, vessels could still remain slightly distended for several milliseconds after the pulse. This deformation was generated with a large bubble (7.3  $\mu\text{m}$  initial diameter) exposed to a low pressure of just 200 kPa, indicating that significant tissue strains can be generated at low acoustic pressures.

### 3.4.2 Extravasation of microbubbles

Microbubbles can extravasate from small microvessels using ultrasound parameters that have been used to deliver drugs across the BBB in mice and in humans. Unlike observations in a previous study (Caskey et al. 2007), this did not require coalescence of microbubbles. While several studies have observed the rupture of small microvessels by microbubble oscillations (Miller and Qudus 2000; Skyba et al. 1998), we additionally observed microbubbles that had left the vessels were often pushed deep into the tissue by the primary radiation force. This has previously been observed in agarose gels, but only at PNPs in excess of 1 MPa at 1 MHz (Caskey et al. 2009).

If this were to occur *in vivo*, it could have several effects. Firstly, as shown in Figure 3.9A, microbubble extravasation is associated with extravasation of dye contained within the vessels. It may therefore act as a potential physical mechanism of BBB disruption. Intravital microscopy studies have shown two distinct timescales of opening – ‘fast’: immediate extravasation, primarily in smaller vessels, and ‘slow’: a gradual increase in permeability over a period of minutes. As demonstrated in Figure 3.9B, extravasation of microbubbles can cause extravasation of dye within the vessel to start immediately through the pore created. It is plausible therefore that extravasation of microbubbles could be one mechanism of the ‘Fast’ phase of opening, particularly considering that extravasation has only been seen here in small vessels, and is likely to be far less common in larger vessels with thicker walls.

Secondly, it is plausible that microbubble extravasation could be a mechanism of tissue damage, and, in particular, be a cause of localized red blood cell (RBC) extravasation. RBC extravasation has been observed in histological examinations of animals exposed to BBB opening treatments. The rate at which extravasation of microbubbles occurs in the slices correlates quite well with the relative rate of erythrocyte extravasation observed in *in vivo* studies of animals sonicated at these parameters, with a mechanical index of 0.2 and 0.4 being generally safe, but damage significantly increasing at higher pressures (Fan et al. 2016; McMahon et al. 2020; Morse et al. 2019; Shen et al. 2016; Shin et al. 2018). Haemorrhage resulting from sparsely distributed micrometre-sized pores created by bubbles in very small microvessels is unlikely to be large enough to be observable on an MRI scan or to directly generate observable symptoms in a patient or animal, however.

Finally, while microbubble extravasation may be a mechanism of damage, it is also plausible that it may have therapeutic benefits. The pores created by whole microbubbles are likely to be large enough to allow almost any therapeutic agent to pass through. Penetration of oscillating bubbles deep into the tissue may be an effective way of increasing the distribution of drugs throughout the

organ, as has been proposed with nanoparticles in other organs (Kwan et al. 2015). This may be particularly valuable for microbubbles loaded with therapeutics.

### 3.4.3 Microbubble dynamics in confinement

Asymmetric oscillations of microbubbles were often observed when confined in very small microvessels. This asymmetry in oscillations could potentially alter the bubbles' acoustic signatures, which may be of significance in real time therapy monitoring. This phenomenon has particular implications for modelling studies, as it highlights the limitations of Rayleigh-Plesset based models (which usually assume spherical symmetry) in predicting the dynamics of microbubbles in the microvasculature of real tissue.

### 3.4.4 Mechanisms of drug delivery across the BBB

It is likely that there are many different mechanisms behind BBB opening with microbubbles and ultrasound. Some may be linked to tight junction disruption, transcytosis, or simply small regions of vascular damage. MHz oscillations of endothelial cells (Figure 3.7) clearly exert strains that could plausibly disrupt tight junctions directly, or stimulate the inner layer of the vessel. However, this study also demonstrates that investigations into the mechanism of drug delivery across the BBB should not be limited to vascular endothelial cells. As shown in Figure 3.12, the spatial extent of mechanical stress can extend well beyond the vessel lumen. A single bubble can therefore apply mechanical stress to tissues beyond the endothelial cells, potentially influencing other cells to modulate the blood-brain barrier permeability. Additionally, microbubbles can be pushed significant distances during an ultrasound pulse, causing direct effects over a much wider region of tissue than a single site beside the bubble's initial location. An additional potential mechanism suggested here is

through vessel rupture caused by microbubble extravasation. The potential significance of this is discussed in more detail in Chapter 4.

### 3.4.4 Limitations

This ultimate purpose of this study is to improve our understanding of the mechanisms of therapies to inform future refinements of clinical treatments. There are many differences between the environment in the slices and an *in vivo* setting, however, which may mean some of the observations here may not be seen *in vivo*. Firstly, there was no blood flow or blood pressure in the slices, with vessels collapsed in many sections. This made it difficult to observe extravasation of a dye over longer time periods as fluid did not continually replenish the site. It also meant that vessels were not exposed to typical flow stresses, which may be important in regulating the BBB.

Secondly, the blood was replaced by SonoVue and ink. The presence of red blood cells in an *in vivo* setting is likely to impact the bubble dynamics (Masuda et al. 2011). Additionally, the concentration of dissolved gases in the perfused solution may be different to that of blood, affecting the transfer of gas in or out of the bubble, and therefore its lifetime or behaviour. Thirdly, because the tissue is being kept *in vitro*, cellular activity is likely lower than in an *in vivo* setting. However, most of the tissue is likely to have remained viable throughout the period of imaging, as shown in Figure 3.15. The viability of acute slices is typically around 6-12 hours (Buskila et al. 2014), considerably longer than the <2 hours these experiments took place over. While some tissue degradation may have occurred, it is unlikely that significant necrosis would have set in during this short period. Surface layers of the tissue that have been sliced directly were more likely to contain necrotic tissue, but these were ignored where possible. While the depth of each bubble in the tissue could not be accurately measured, bubbles that were clearly located near the surface of the slice were ignored.

The slices used here were from juvenile rats, chosen for their high tissue viability and transparency. Because the brain is still developing however, many aspects of their physiology are different to that of an adult brain. Rodents are born with far less developed brains than humans, making this age difference more pronounced. In rats, most of the tight junction structure of the BBB is formed in-utero, although this is less structurally complex than in adults. A significant proportion of the capillaries form postnatally within the first three weeks after birth (Ogunshola et al. 2000).

A particularly significant difference is the lack of active transporters of the BBB that are present and fully developed in the neonate. P-glycoprotein transporters for instance play an important role in the BBB function by active transport of a variety of hydrophobic amphipathic molecules (>400 Da) back into the blood. These transporters are not fully developed until after weaning (Schmitt et al. 2017). Juvenile slices may therefore be unsuitable as a platform to fully investigate all of the mechanisms of BBB opening.

The microbubble dynamics studied in this paper focused on larger microbubbles. While SonoVue has a mean diameter of around 2.5  $\mu\text{m}$  (Schneider 1999), this study was limited to microbubbles above 2  $\mu\text{m}$  in diameter. This was due to the difficulties of acquiring clear images of very small microbubbles against a complex tissue background.

While efforts were made to avoid bubble-bubble interactions, the nature of the slice environment meant these could not be avoided with certainty. In many videos, especially those observing over 10 ms pulses where bubble motion was significant, it was possible that bubbles outside the focal plane were present, or were obscured by regions of denser tissue. Conclusively categorizing microbubbles as having extravasated was sometimes difficult, as the quality of the images varied and the precise locations of the vessel boundaries were not always obvious. It is possible that slicing may have physically weakened vessels or introduced small tears that may artificially have increased the probability of extravasation. However, bubble extravasation was obvious in many videos based on vessel shape changes, dye extravasation, and bubble motion.

### 3.4.5 Relevance to clinical and *in vivo* studies

Because of the many differences between the setup used here and an *in vivo* setting, it is impossible to state conclusively which, if any, of the phenomena reported here may be occurring *in vivo*, and none of these observations can be directly linked to clinical effects.

However, despite the limitations outlined in §3.4.4, such as the lack of blood and blood flow, the slices are likely to remain a reasonable approximation to the *in vivo* environment. Large regions of the slices continue to exhibit aerobic respiration throughout the imaging period (Figure 3.16) for instance. The results here focussed on the mechanical properties of the tissues, meaning slightly reduced cellular activity is not a major concern (provided there is no significant necrosis), although high viability may be essential for potential future experiments using this platform to investigate biological responses. This is therefore an area for future refinement. There are several ways tissue viability could be improved in future experiments, for instance by perfusing the slices with 95% O<sub>2</sub>: 5% CO<sub>2</sub> gas, and performing the transcatheter perfusion while the heart is still beating, enabling slices to be obtained more rapidly.

Many phenomena reported here may therefore be occurring *in vivo*. Some may be more important than others in achieving therapeutic outcomes, and some may be leading to damage. It may therefore be useful to design microbubble formulations and ultrasound pulse sequences that increase or reduce the likelihood of specific phenomena, initially as a way of testing the validity of the slices as a platform to predict biological effects. The observations of extravasation demonstrate that microbubbles may not be confined to the vessel lumen, and therefore more distant effects should be investigated in future *in vivo* studies.

While acute slices cannot predict with certainty the behaviour of microbubbles *in vivo*, this study demonstrates their potential value as a platform to elucidate the mechanisms of ultrasound and microbubble drug delivery across the blood brain barrier. This understanding could lead to refinements in clinical approach to improve safety and efficacy.



### **3.5 Conclusions**

This chapter demonstrates a technique to directly observe microbubbles under sonication in the microvasculature of living brain tissue, using ex vivo acute juvenile cortical slices. This study has shown many different phenomena can occur in brain tissue when exposed to therapeutic ultrasound pulses, including microsecond-scale vessel wall oscillations, millisecond-scale tissue deformations, microbubble extravasation, microbubble dissolution, and asymmetric bubble oscillations. The relative significances of these phenomena are unclear, however, and this is investigated in more detail in Chapter 4.

These results demonstrate the potential value of acute slices from perfused rats as a method of investigating the mechanisms of BBB opening in more detail in future, especially for investigating biological effects on the brain tissue, which could be investigated using transgenic animals or staining combined with real time fluorescence imaging. Acute slices could provide a valuable platform from which to better understand the mechanisms of BBB opening using microbubbles, and thus to refine clinical approaches.

# Chapter 4: Effects of ultrasound parameters on microbubble extravasation and destruction

## 4.1 Introduction

In the previous chapters, several ways in which ultrasound-driven microbubbles can interact with soft tissues are investigated. These include distention and invagination of microvessels (due to volumetric oscillations), indentation into soft tissues, and extravasation through microvessels (both due to the primary radiation force). When exposed to ultrasound, microbubbles have also been observed to dissolve and fragment within microvessels. It is unclear, however, which (if any) of these different phenomena may be occurring *in vivo*, which (if any) are most important as mechanisms of BBB opening, and which (if any) are potentially harmful. One way to improve our understanding of this is to investigate the probability of these various phenomena under different ultrasound and microbubble parameters, and compare trends to observations from published *in vivo* studies performed with similar parameters. While this cannot tell us conclusively what is happening *in vivo*, this information may nonetheless be valuable in highlighting areas for further study.

This chapter aims to investigate in detail two of the phenomena described in Chapter 3: extravasation of microbubbles due to the primary radiation force, and dissolution of microbubbles after ultrasound exposure. Both of these phenomena are investigated using the acute brain slice platform described in Chapter 3, due to its improved relevance to an *in vivo* setting in comparison to artificial vessels.

As shown in Chapter 3, microbubbles can extravasate from brain microvessels at parameters typical of BBB opening. Extravasation of microbubbles may be an important mechanism of either drug delivery or tissue damage, through creating pores in vessels that could allow drugs or blood to escape into the parenchyma. If extravasation is deemed to be potentially significant, it is important

to investigate under what parameters extravasation is most and least likely, so the probability of this can be maximised or minimised through the careful selection of ultrasound parameters.

Chapter 3 also demonstrates that microbubbles can be destroyed by exposure to ultrasound. This typically occurs shortly ( $<1$  second) after exposure to a 10 ms pulse. Understanding the situations in which microbubbles are most and least likely to dissolve could enable pulse sequence designs that enable greater effects to be generated by each bubble, by prolonging its lifetime. If using lower pressure amplitudes, or splitting a single long pulse into many short pulses, could prolong the total lifetime of the bubble, its motion due to blood flow could potentially enable more uniform effects over a wider region.

Extravasation and dissolution are binary phenomena that can be much more easily defined and compared than continuous variables, such as tissue displacement for instance. Binary classifiers were chosen to simplify analysis of phenomena dependent on a wide range of different variables within the slices that cannot be controlled for (including some which cannot even be measured). These include vessel size and wall stiffness, vessel orientation, and bubble properties.

There are several important parameters to be investigated in relation to these bubble phenomena. Firstly, the relationship between bubble behaviours and the size of microbubbles is investigated, as this can affect their behaviour (Choi et al. 2010; Feshitan et al. 2009). Microbubbles have a resonant frequency dependent on their diameter, and so bubbles that are closer to resonance will respond more significantly than bubbles driven well off resonance (Supponen et al. 2020; van der Meer et al. 2007).

Secondly, ultrasound pressure is an important variable that strongly affects the behaviour of microbubbles, with higher pressures causing increased amplitude of radial oscillations, and probability of nonlinear oscillations, as well as increased radiation forces (Shi et al. 1999; Vos et al. 2007)

Two different centre frequencies are compared. In the previous chapters, a centre frequency of 1 MHz was used. This is quite common in many therapeutic applications, as well as in *in vivo* animal studies of BBB opening. However, for clinical studies, lower frequencies must be used, to allow good penetration through the skull. Typically this is around 200-300 kHz. Typically, 220 kHz is used clinically (such as by the InsignTec system) for transcranial BBB disruption (Abraham et al. 2019; Lipsman et al. 2018; Mainprize et al. 2019; Pouliopoulos et al. 2020b). For these experiments, a very small transducer was required to fit horizontally under the surface of the water tank while remaining aligned with the focal plane of the lens immersed from the top of the tank. Low frequencies are difficult to generate from small transducers, however, and obtaining small 220 kHz transducer elements proved challenging, so 330 kHz was used instead.

In order to investigate trends with ultrasound parameters, it is important to establish a meaningful means of comparison between different sets of parameters. Instead of comparing equivalent pressures between the two frequencies, the pressures were matched to mechanical index. Comparable pressures were chosen across the two frequencies based on mechanical index, as this has been shown to be a reliable indicator of the threshold and extent of BBB opening across frequencies in *in vivo* studies (McDannold et al. 2008). This approach was first validated through simulations. Because the primary radiation force is the main force behind extravasation, simulations were performed of the magnitude of the radiation force on different sized microbubbles at the two frequencies, as a function of mechanical index, to explore this relationship further, as mechanical index is typically used to compare acoustic emissions from cavitation, not radiation forces.

Finally, ultrasound pulse length and pulse sequences are investigated. Typical studies use pulse lengths of the order of 2-10 ms in length, which are very long in comparison to the 1  $\mu$ s period of an acoustic cycle. However, several studies have shown that much shorter pulses can also deliver drugs (Choi et al. 2011; Fletcher et al. 2021). One sequence that utilises short pulses is the Rapid Short Pulse (RaSP) sequence. RaSP is a pulse sequence designed to improve the uniformity of BBB opening.

It is based around short ultrasound pulses of a few acoustic cycles. The sequence was first developed in an *in vitro* setting to enable more uniform cavitation activity than can be achieved with 10 ms pulses. One particular sequence used splits up each 10 ms pulse into a sequence of 13 even spaced 5 cycle pulses. This mean the total period of sonication is 0.65% of the 10 ms pulse (Pouliopoulos et al. 2016). When tested *in vivo*, in comparison to a 10 ms pulse at the same PNP, RaSP can deliver drugs more uniformly and with lower rates of tissue damage (Morse et al. 2019). Smaller quantities of drugs are typically delivered in comparison to the equivalent 10 ms pulses, however (McMahon et al. 2020; Zhou et al. 2021). It is hypothesised that RaSP reduces destruction of microbubbles, enabling them to deliver drugs more gradually over a larger area, while also limiting local damage due to reduced cavitation activity (Pouliopoulos et al. 2016). The destruction of microbubbles due to both RaSP and 10 ms tone bursts are investigated here, to evaluate the different bubble behaviours during different BBB opening pulse sequences.

In summary, this chapter aims to investigate the probability of microbubble extravasation and microbubble dissolution in acute brain slices, as a function of various ultrasound parameters, to better understand their potential significance in *in vivo* settings. The probability of extravasation is investigated as a function of mechanical index (0.2-0.8) and centre frequency (1 MHz and 330 kHz). The probability of bubble destruction is investigated as a function of mechanical index and pulse sequence, comparing the 10 ms tone bursts used throughout this thesis with the Rapid Short Pulse sequence which has previously been evaluated *in vivo* (Morse et al. 2019).

### **4.2 Methods**

The overall aim of this chapter is to investigate trends in microbubble extravasation and microbubble dissolution within brain tissue with varying ultrasound parameters. Specifically, ultrasound centre frequency and pressure, and ultrasound pulse sequence were tested. Parameters were first investigated through simulations to identify theoretical trends. These simulations were used to inform the parameter selection used in the experiments to enable a meaningful comparison between different frequencies. Two different frequencies were chosen: 1 MHz and 330 kHz, and each of these was tested at 3 or 4 different pressures, corresponding to a range of therapeutic applications. Once suitable parameters had been identified for comparison, the probability of extravasation of microbubbles was investigated at different pressures at both frequencies, and the probability of dissolution was investigated using two different pulse sequences at different pressures.

#### **4.2.1 Simulations - methods**

##### **Radiation force**

In order to inform the selection of ultrasound parameters for experiments, simulations were performed. As mentioned, Mechanical Index is believed to be a useful indicator for degree of cavitation effects induced by ultrasound across different pressures and frequencies (McDannold et al. 2008; Miller et al. 2008). Because the key phenomenon here was the primary radiation force, not simply volumetric oscillations, simulations were performed to investigate whether mechanical index is a reliable indicator of the magnitude of radiation force on SonoVue microbubbles across the two frequencies compared here.

These simulations were performed using the Rayleigh-Plesset equation (equation 2), as described in Chapter 1 (Marmottant et al. 2005):

$$\rho_l \left( R\ddot{R} + \frac{3}{2}\dot{R}^2 \right) = \left[ P_0 + \frac{2\sigma(R_0)}{R_0} \right] \left( \frac{R}{R_0} \right)^{-3\kappa} \left( 1 - \frac{3\kappa}{c} \dot{R} \right) - P_0 - \frac{2\sigma(R)}{R} - \frac{4\mu\dot{R}}{R} - \frac{4\kappa_s\dot{R}}{R^2} - P_{ac}(t)$$

With the surface tension term defined as a function of bubble radius as:

$$\sigma(R) = \begin{cases} 0 & \text{if } R \leq R_{buckling} \\ \chi \left( \frac{R^2}{R_{buckling}^2} - 1 \right) & \text{if } R_{buckling} < R \leq R_{break-up} \\ \sigma_{water} & \text{if } R > R_{break-up} \end{cases}$$

Once the radius-time curve had been predicted for each bubble, the radiation force was determined using the following equation (Dayton et al. 2002; Leighton 1994):

$$\mathbf{F} = -V(t)\nabla P$$

Symbol	Parameter	Value
$\rho_l$	Density of water	1000 kg/m <sup>3</sup>
$P_0$	Atmospheric pressure	101 kPa
$\kappa$	Gas exponent (sulphur hexafluoride)	1.07
$\mu$	Water dynamic viscosity	2000 Pa s
$\kappa_s$	Shell viscosity	1.5e-8 kg/s
$\sigma_{water}$	Surface tension of water	72 e-3 N/m
$R_{break-up}$	Break-up radius	$\left( \frac{\sigma_{water}}{\chi} + 1 \right) R_0^2$
$\chi$	Shell elasticity	0.2 N/m
$R_{buckling}$	Buckling radius	$R_0$
$c$	Speed of sound	1540 m/s

**Table 1:** Parameters used in simulations, taken from (Tu et al. 2009)

This force was then time averaged over the 5<sup>th</sup>-10<sup>th</sup> ultrasound cycles to avoid the effect of transient behaviour at the start of the pulse. The time-average force was calculated for bubbles with radii from 1 to 4.5  $\mu\text{m}$  at both 1 MHz and 330 kHz at an equivalent mechanical index. This was because

the radiation force should vary with bubble size, due to resonance behaviour (Dayton et al. 2002).

The equations were solved in Matlab using the built-in ODE solver ode45, which uses a 4<sup>th</sup> and 5<sup>th</sup> order Runge-Kutte formula.

### 4.2.2 Experimental methods

The experimental setup was the same as that used in Chapter 3. In brief, rat pups were euthanised and then transcardially perfused with a concentrated solution of SonoVue, heparin and ink. The frontal cortices were sectioned into 250  $\mu\text{m}$  thick slices, and these were placed in a bath of aCSF within a water tank, under an objective lens linked to a high-speed camera. While imaged at 5,480 fps, the sample was sonicated, and the movement of individual microbubbles was observed. For the studies investigating bubble dissolution, images were also obtained using the IDS colour camera used in Chapter 3, recording at 20 fps. Slices were sonicated using either the 1 MHz Olympus immersion transducer used previously (Figure 2.7), or an in-house manufactured 330 kHz transducer.

### Extravasation

To investigate the probability of extravasation within the slices, mechanical indices of 0.2, 0.4 and 0.6 were tested, corresponding to 0.2 MPa, 0.4 MPa and 0.6 MPa at 1 MHz, and 0.11 MPa, 0.23 MPa and 0.35 MPa at 330 kHz. Additionally, and MI of 0.8 (0.8 MPa) was tested at 1 MHz only, because of the limitations of the 330 kHz transducer.

Because of the large number of variables that can affect extravasation, results were compared across groups of approximately 20 bubbles for each parameter. Several properties of each group, including bubble radii, and angle of the vessel relative to the direction of ultrasound propagation, were compared to ensure the different groups were comparable overall.



### Dissolution

For evaluation of bubble dissolution, the probability of dissolution was compared between 0.2 and 0.4 MI 10 ms pulses, and between RaSP sequences at the same pressures and frequencies. For bubbles that did dissolve, their sizes and times taken to dissolve were measured and compared.

RaSP sequences were chosen because they have previously been evaluated as potential alternative pulse sequences to tone bursts (McMahon et al. 2020; Morse et al. 2019; Zhou et al. 2021).

Mechanical Indices (equivalent to PNPs in MPa) of 0.2 and 0.4 were chosen because these are close to the pressure threshold required for drug delivery. Higher pressures were not tested, because, with the 10 ms pulses, bubbles often moved too far and were therefore frequently pushed out of focus by the end of the pulse.

The probability of extravasation was not compared systematically between RaSP and tone bursts. With 10 ms pulses, when microbubbles burst through the walls of blood vessels, they typically accelerate and move great distances out of the vessel. This behaviour is easy to categorise due to the sudden change in behaviour, and the obvious distance the bubble has moved from the initial location of the vessel. With RaSP sequences, the bubbles do not move very significant distances, because the total duration of sonication is much shorter. Because the precise boundary of the vessel is not always easy to define, the shorter distances travelled during RaSP sequences made evaluating whether or not a bubble had extravasated much more challenging, and consequently a reliable comparison was not thought to be possible with the methods used here.

### 4.2.3 Analysis

For the videos investigating extravasation of bubbles, videos were first assessed to see if they met the inclusion criteria. Videos were excluded if: the bubble was not approximately in focus in the first frame; there was a second bubble in the field of view that was either in the same vessel, or in a different but nearby vessel ( $< 20\mu\text{m}$  separation); or if the whole slice moved so much during the pulse that the vessel was no longer in the field of view of the camera at the end of the video.

Bubbles were chosen for sonication if both they and the boundaries of the surrounding vessel could be resolved clearly, and did not appear to be close to the surface of the slice.

Two independent observers categorised all the approved videos into extravasated, did not extravasate, or unclear, based on both the colour and high-speed videos. The observers were blinded to the pressure/mechanical index, and to the other observer's results. The diameter of each bubble was measured using the same Matlab script as used in Chapter 2. The subgroups were compared against each other using a Chi-squared test, excluding unclear results.

The angle of each vessel was measured manually in Fiji, to ensure the orientation of vessels relative to the direction of ultrasound propagation was not biased due to selection of bubbles by a single operator. The angle was measured in degrees, anticlockwise from the horizontal, from 0 to 180°. Vessel angles and radii were compared between groups to ensure each group contained a similar population of bubbles. Vessel angles were important to measure, because it is important to investigate whether there was any bias in vessel orientation when the bubbles in each slice were being selected for sonication. It is also important to investigate as the probability of a bubble extravasating may be higher if it is being driven perpendicularly into the vessel wall. The 2D projection shown in the remains a valid indication of angle in 3D, because the important factor is the angle of the vessel relative to the plane of propagation of the ultrasound.

For the bubble destruction studies, dissolution was observed using the 20 fps colour camera, because this enabled higher resolution images of the bubbles to be obtained over much longer time periods than with the Chronos 1.4. Whether or not the bubbles dissolved was categorised based on whether the bubbles were still present 30 seconds after the pulse. The probability of dissolution was compared between groups using a Chi-square test. The time to dissolution was determined manually by the frame at which the bubble could no longer be seen. The time to dissolution was compared with the bubble radii and compared between groups (pressure or pulse sequence) using a multivariate t-test.

#### 4.2.4 330 kHz transducer calibration

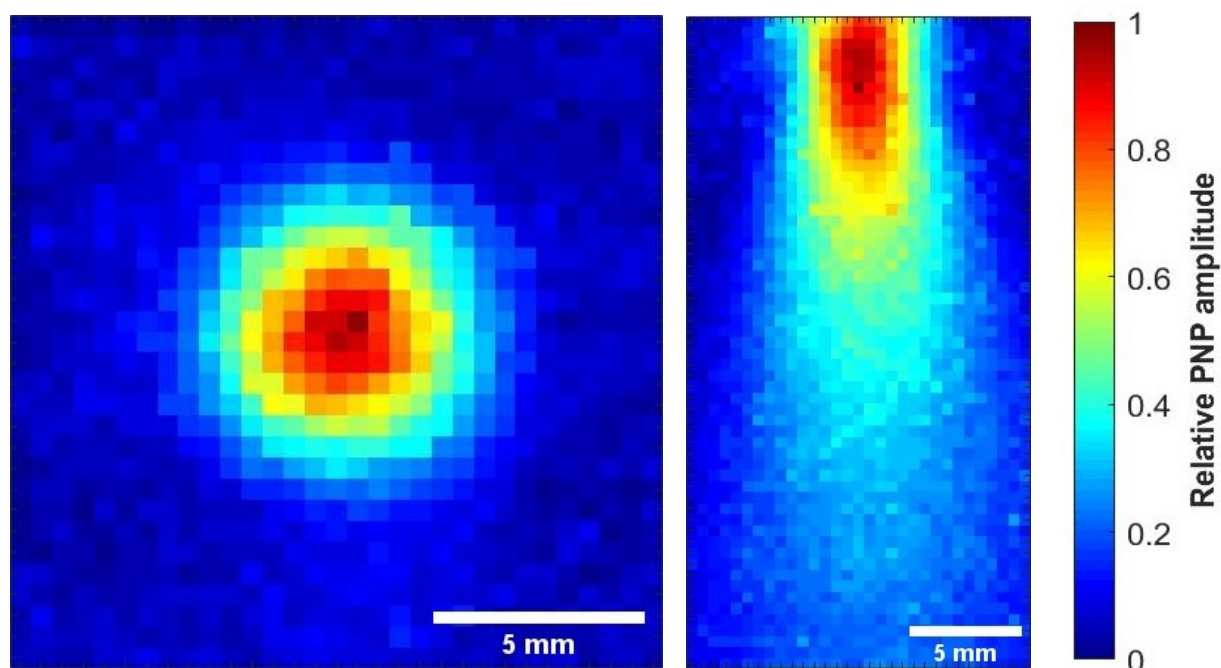


**Figure 4.1:** Beam profile of in-house manufactured 330 kHz transducer, measured at a centre

frequency of 330 kHz, PNP of 100 kPa, and pulse length of 20 cycles. The focus is very close to the surface of the transducer (approximately 5 mm).

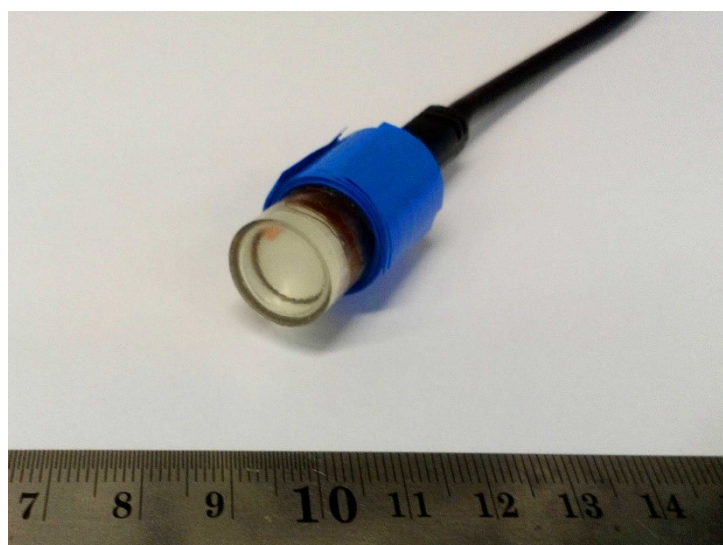


**Figure 4.2:** 330 kHz PZT transducer built in-house. Ruler scale is in centimetres.

A 330 kHz transducer was manufactured in-house (Figure 4.2). This transducer contained an 11 mm diameter PZT element, and was encased in 3D printed Veroclear resin. The casing was curved to give

a theoretical focal length of 50 mm, but in practice this was considerably closer due to the practical constraints of building a small transducer at a low frequency.

The transducer beam profile was calibrated using the same method as in Chapter 2, with a 0.2 mm needle hydrophone attached to a 3D positioning system. This is shown in Figure 4.1. Because of the relatively large focal size, the transducer beam overlapped with the objective lens somewhat, meaning the pressure values under the lens were slightly lower than those measured away from the lens. Because the pressure values were measured by the hydrophone in situ, however, this did not affect the validity of the pressure values used here, although it may have changed the shape of the beam in the focus.

### 4.2.5 Short pulse generation

In previous chapters, only 10 ms pulses were used. With long pulses, it is relatively easy to create a uniform pressure over time, at a single frequency. Here, shorter pulses were also tested. Some transducers designed for long pulse sonications cannot create short pulses due to ringing artifacts, and many imaging transducers, designed to create broadband pulses, will generate a non-uniform wavelet in response to a short impulse.

The ability of the two transducers to generate short pulses was therefore evaluated. The 1 MHz Olympus immersion transducer characterised in Chapter 2 (purchased commercially) is designed primarily for narrowband imaging, and is consequently well damped. It can therefore produce very high quality narrowband short pulses with a uniform peak pressure amplitude and a fast ramp up time. For the 330 kHz transducer, the ramp-up time was much longer, and the transducer experienced prolonged ringing after the pulse (Figure 4.3). This was therefore not suitable for short pulse generation with RaSP sequences, and so short pulses were tested only at 1 MHz.

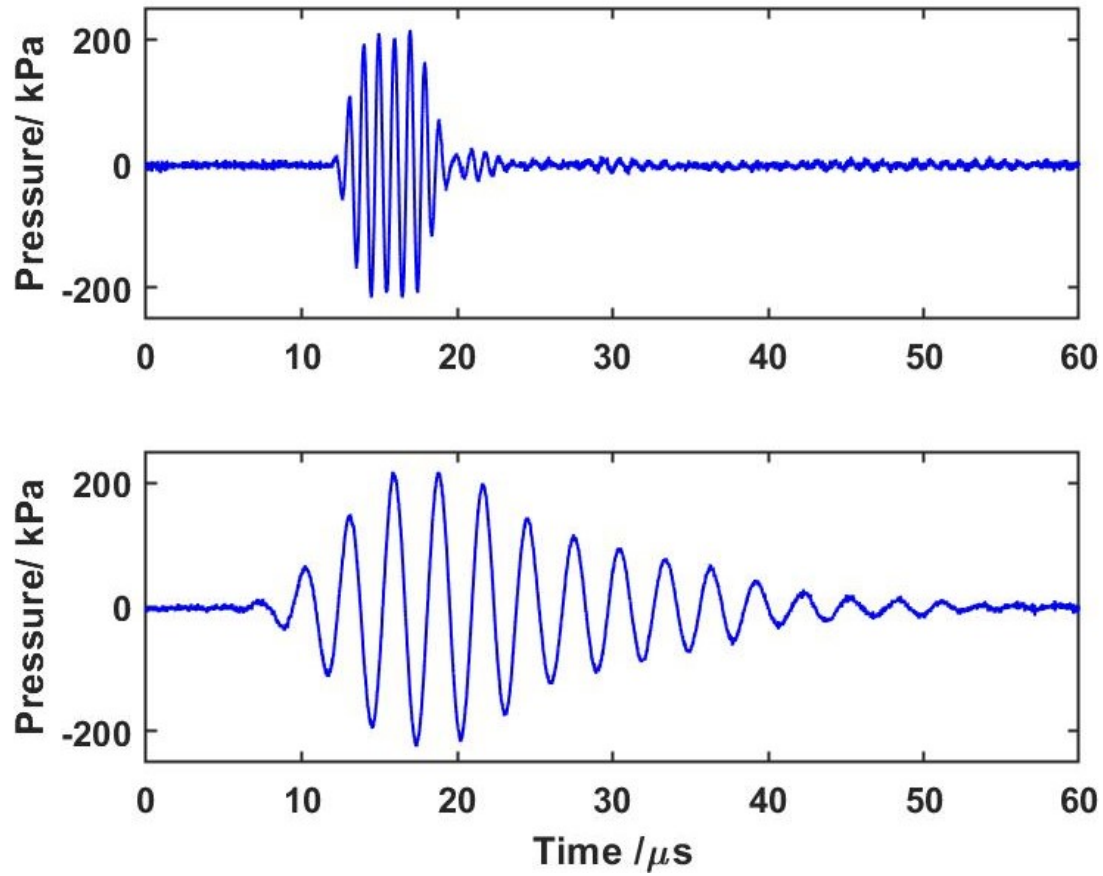


**Figure 4.3:** Pulse shape for 5 cycle input pulses generated by 1 MHz Olympus (above) and 330 kHz in-house (below) transducers. Time measured from the start of the pulse output by the function generator to the transducer. The 1 MHz pulse has a short ramp up time and the peaks are approximately uniform. The 330 kHz transducer has significant ringing.

### **4.3 Results**

This chapter presents results investigating two different phenomena: extravasation of microbubbles due to the primary radiation force, and dissolution of bubbles after an ultrasound pulse. These are investigated using microbubble-perfused acute brain slices. Probabilities of extravasation and dissolution are compared as a function of various ultrasound parameters. To investigate the probability of extravasation, microbubbles were exposed to 10 ms ultrasound pulses at a range of pressures (informed by theoretical results), and two different frequencies. 63 videos at 330 kHz and 86 at 1 MHz were acquired and included for analysis of extravasation. These figures exclude test videos and those with very poor image quality where bubbles could not be identified, which numbered over 100. Dissolution of microbubbles was investigated using two different pressures and pulse sequences. Microbubbles were exposed to an ultrasound pulse and then the time taken to dissolve afterwards was measured. A total of 40 videos were acquired to investigate dissolution.

#### **4.3.1 Parameter selection – simulations**

In Figure 4.4, the radiation force values on the vertical axes are predicted from the Rayleigh-Plesset equation assuming a free bubble, and so the exact values are unlikely to be accurate for a complex tissue environment. However, this model can still provide useful information about trends.

Overall, matching mechanical index across frequencies provides a better approximation to typical magnitude of radiation force than using equal pressures at the two frequencies. However, the trends in primary radiation force with bubble radius are not the same at the two frequencies, or at the three different mechanical indices. For instance, at an MI of 0.6, the two frequencies provide good approximation to equivalent radiation forces at bubble radii up to around 2  $\mu\text{m}$ , but this diverges with larger bubbles. However, because the resonant size of bubbles varies is larger at lower frequencies, this trend does not continue for large bubbles, with those exposed to the lower frequency experiencing far greater forces than at 1 MHz.

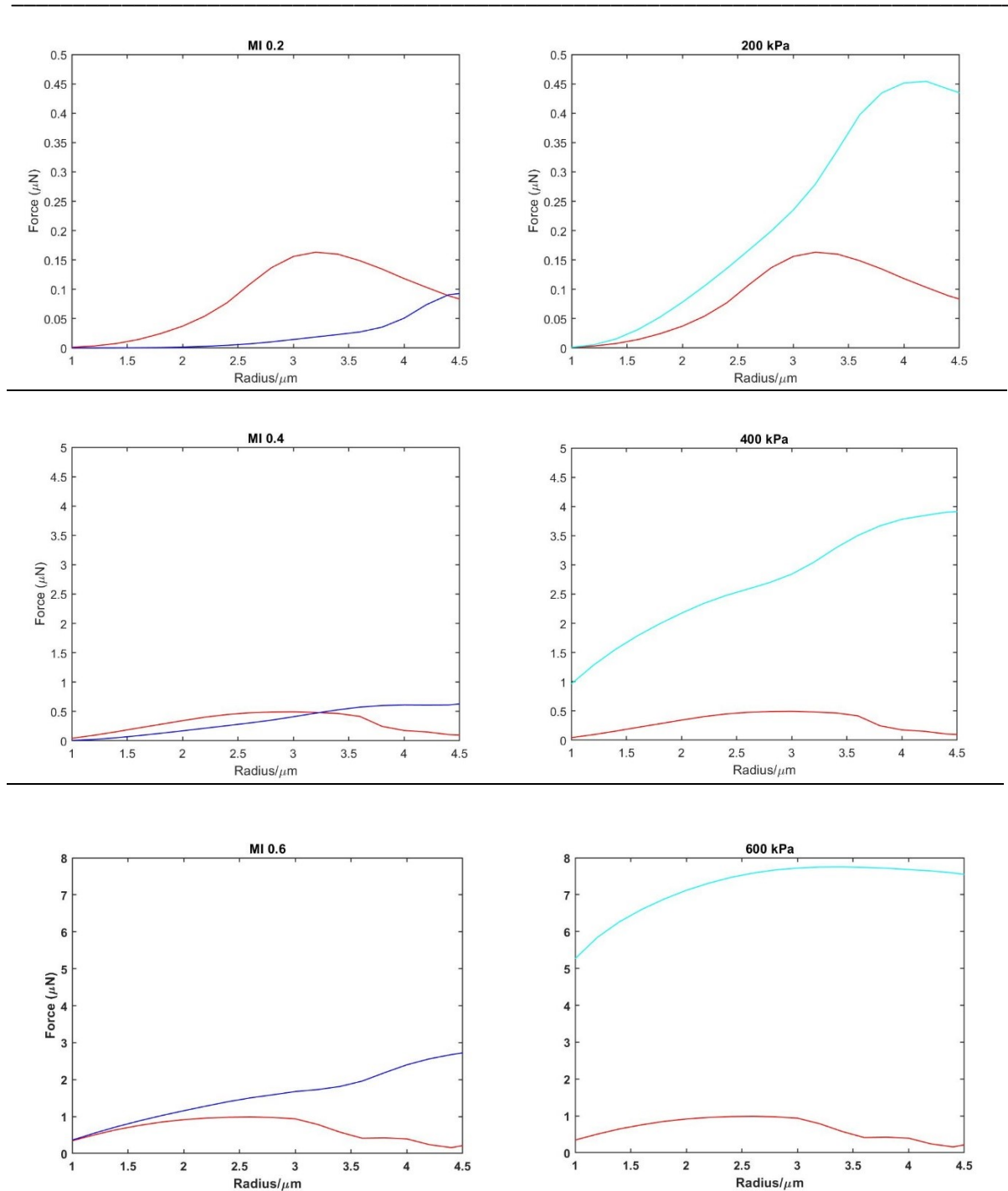


**Figure 4.4:** Predicted time-average radiation force on a bubble of different radii when exposed to an ultrasound pulse. at 1 MHz and 330 kHz at an MI of A) 0.2, B) 0.4, and C) 0.6. D) is the same as A but with a smaller y-scale. Red: 1MHz; Blue: 330 kHz at the same MI as 1 MHz; Cyan: 330 kHz at the same pressure as 1 MHz. The trends vary considerably at different pressures. However, by matching mechanical index across frequencies, the radiation force appears to be kept much more similar than by matching pressures.

### 4.3.2 Microbubble extravasation

#### Extravasation at 330 kHz

Microbubble extravasation can occur during 10 ms pulses at 330 kHz. This can occur at comparable mechanical indices as when extravasation was observed at 1 MHz, as shown in Chapter 3. Figure 4.5 shows the extravasation of a microbubble exposed to a 0.6 MI 330 kHz pulse. Despite the low frame rate, the maximum expansion of the bubble is clearly very significant once it leaves the vessel.

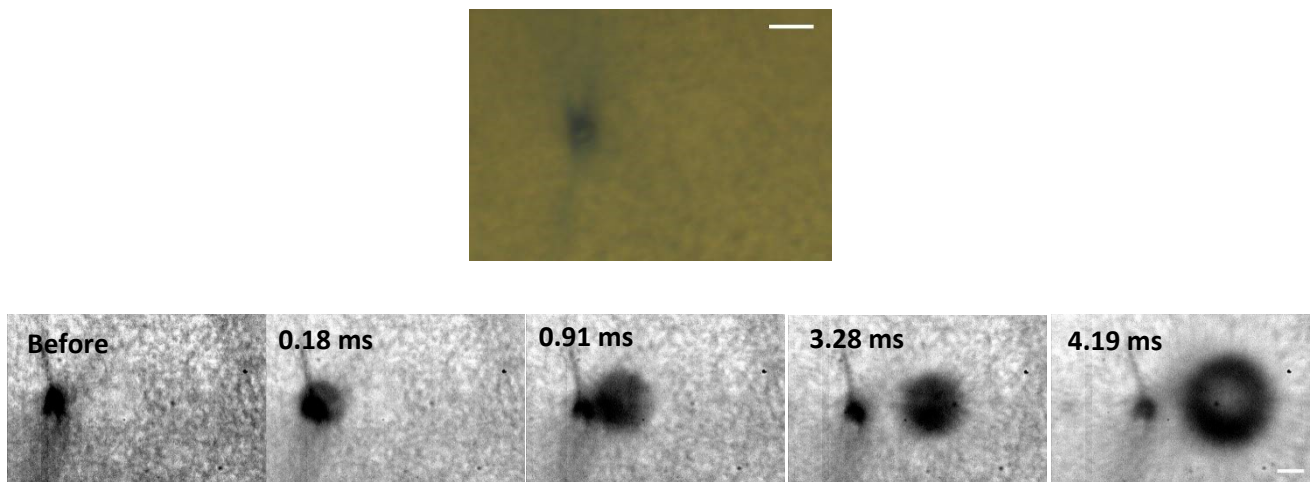


**Figure 4.5:** Extravasation of a microbubble exposed to a 330 kHz, 0.6 MI, 10 ms ultrasound pulse. Top: Colour image from before the pulse, showing the bubble in the vessel. Bottom: Still images taken at (L-R) Before, 0.18, 0.91, 3.28 and 4.19 ms after the start of the pulse. The maximum expansion of the microbubble grows very significantly during the pulse. Scale: 10  $\mu\text{m}$ .



Trends in extravasation with ultrasound pressure and frequency, and bubble size

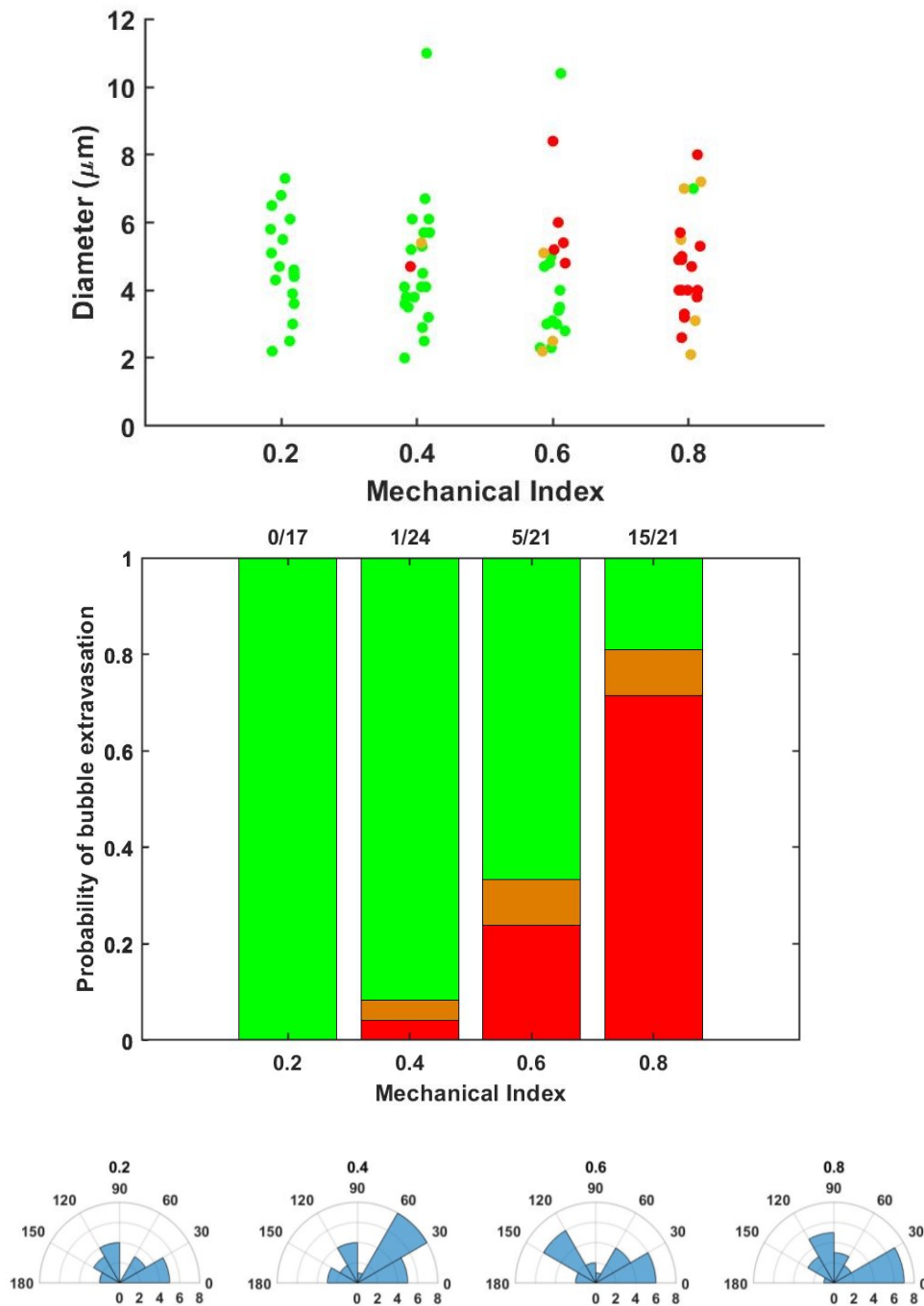


**Figure 4.6:** Extravasation of microbubbles at 1 MHz. A) Extravasation of microbubbles indicating bubble initial radius and ultrasound mechanical index. Red: extravasated; Green: Did not extravasate; Brown: unclear. B) Probability of microbubble extravasation at 1 MHz over mechanical indices. C) Angles of vessels containing microbubbles sonicated at each pressure. Radial axis indicates number of videos in each bin.

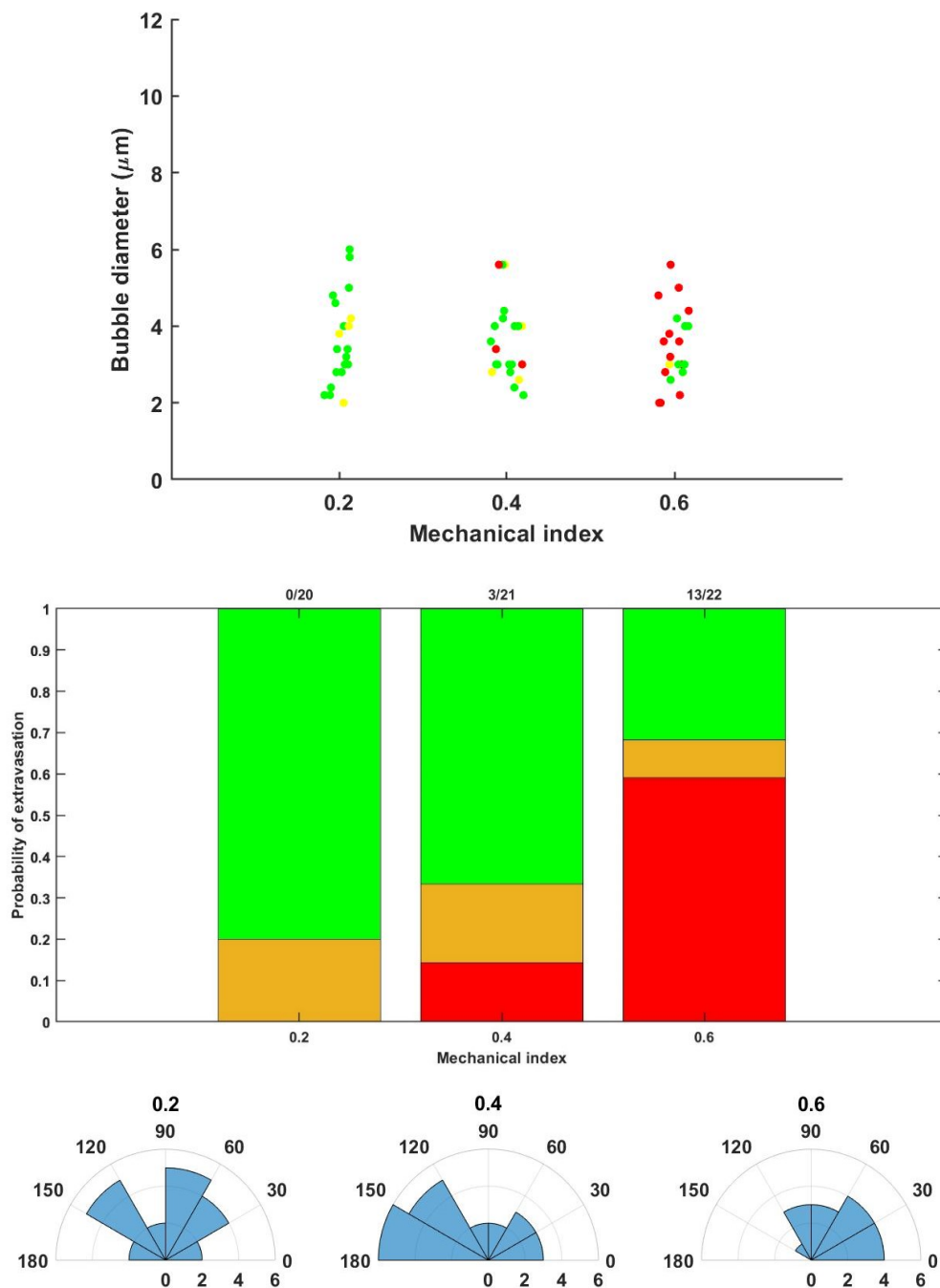


**Figure 4.7:** Extravasation of microbubbles at 330 kHz. A) Extravasation of microbubbles indicating bubble initial radius and ultrasound mechanical index of a 330 kHz, 10 ms pulse. Red: extravasated; Green: Did not extravasate; Brown: unclear. A mechanical index of 0.8 could not be tested, as in Figure 4.6, due to the limitations of the transducer B) Probability of microbubble extravasation at 330 kHz over different mechanical indices. C) Angles of vessels containing microbubbles sonicated at each pressure

The probability of microbubble extravasation was investigated as a function of initial bubble radius, ultrasound pressure and ultrasound frequency. At 1 MHz, no microbubbles extravasated at an MI of 0.2, and only one was confirmed to extravasate at 0.4. The probability of extravasation increased significantly at higher ultrasound pressures, with the majority of bubbles extravasating when exposed to an MI of 0.8. At 0.4 and 0.6 MIs, the bubbles which extravasated were larger than average ( $>4\ \mu\text{m}$  in diameter). These are around the predicted resonant diameter for a bubble at 1 MHz. However, because of the small sample size, this observation is not rigorous. There was no trend in extravasation with bubble size at 0.8 MI, with bubbles of all sized extravasating.

At 330 kHz, a broadly similar trend was observed, with no bubbles extravasating at an MI of 0.2, but increasing probabilities at 0.4 and 0.6. Probabilities of extravasation at each mechanical index were compared between frequencies using a Chi-square test. There was no significant difference between probabilities of extravasation at 0.2 and 0.4 ( $p>0.1$ ), but there was a significant difference ( $p<0.05$ ) at 0.6. Given the relatively small sample sizes, uncertainty in categorising for several videos (indicated by the orange regions), and many other variables, this result in only one of the subgroups must be viewed with caution.

Angles were generally well distributed in all subgroups, with no more than 1/3 of the bubbles in each subgroup being within a single  $30^\circ$  bin. The distributions were not perfectly even however, because of the small sample sizes, and so there was variation between the different groups.

### 4.3.3 Dissolution of microbubbles

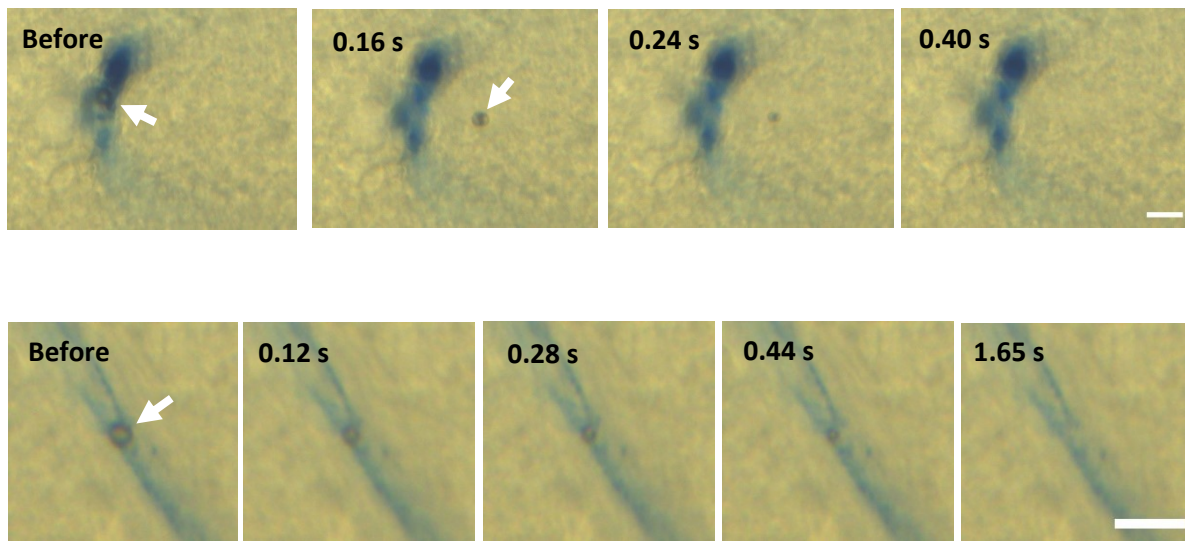


**Figure 4.8:** Examples of dissolution of microbubbles (highlighted with arrows) with (Top) 10 ms pulses (following extravasation) and (Bottom) RaSP, both at 400 kPa, 1 MHz. Scale: 10  $\mu\text{m}$

Without ultrasound, activated SonoVue microbubbles typically dissolve gradually over a period of several hours (Schneider 1999). However, when exposed to an ultrasound pulse of sufficient amplitude, microbubbles can dissolve much more quickly, as shown in Figure 4.8.

Of the 40 bubbles tested, none was destroyed during the pulse, with the only mode of destruction observed being a gradual dissolution over a time period after the pulse ranging from hundreds of milliseconds to several seconds. Dissolution can occur following either a single 10 ms pulse, or a RaSP burst.

#### Trends in microbubble dissolution

The probability and speed of bubble destruction was investigated when exposed to RaSP and 10-ms pulses at 1 MHz and either 0.2 and 0.4 MPa PNP, and is shown in Figure 4.10.

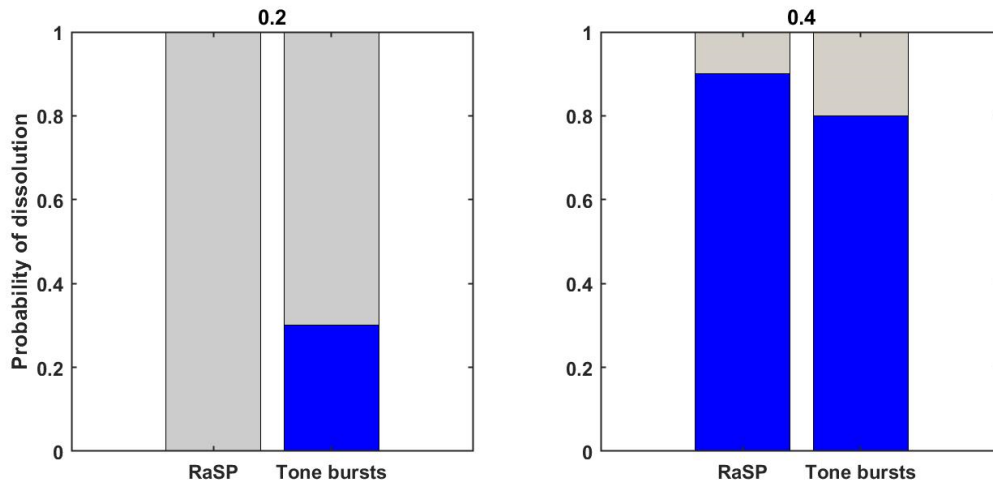


**Figure 4.9:** Probability of dissolution of microbubbles over a 30 second period after exposure to RaSP or 10 ms tone bursts, at either 0.2 or 0.4 MPa at 1 MHz. There were 10 bubbles in each group. Grey: Did not dissolve, Blue: dissolved

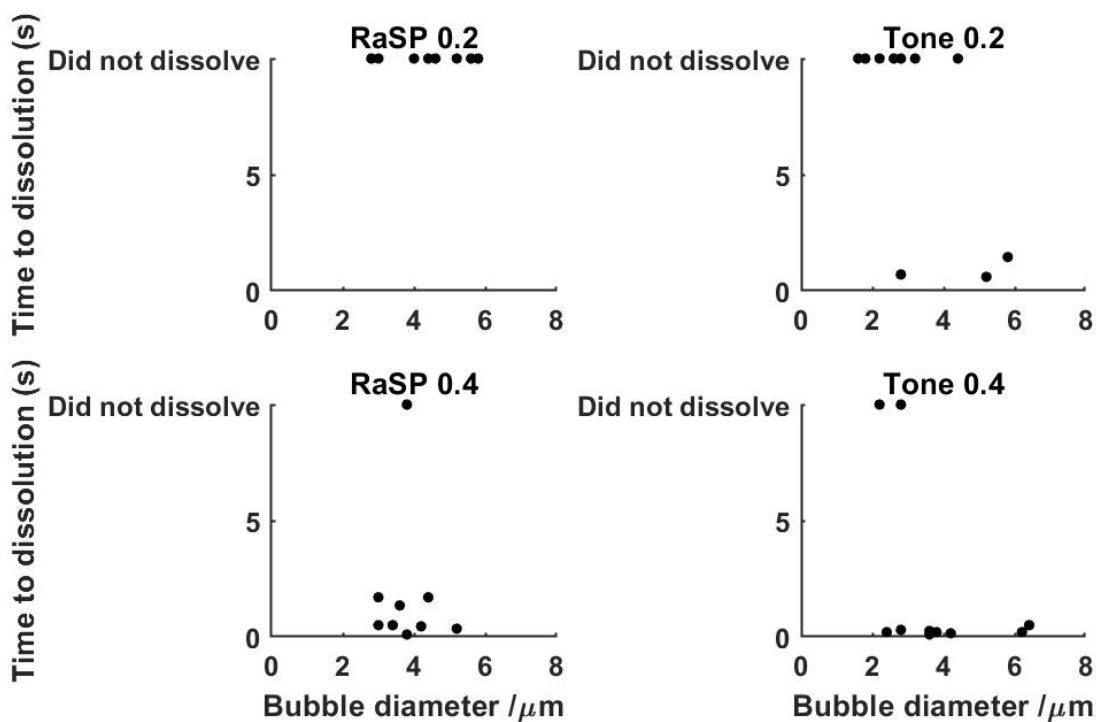


**Figure 4.10:** Time to dissolution of microbubbles vs bubble diameter with RaSP vs 10 ms tone bursts at 0.2 and 0.4 MPa at 1 MHz. There is no clear trend in dissolution time with bubble diameter

As shown in Figure 4.10, the probability of bubble dissolution was higher at 0.4 MPa than at 0.2 MPa for both RaSP and tone bursts. There was no difference between the two sequences in terms of

probability of destruction at either of the pressures tested (Chi-square test,  $p>0.1$ ). For bubbles that did dissolve, at an MI of 0.4, average time to dissolution was significantly greater ( $p=0.02$ ) in the RaSP group than in the tone burst group (Figure 4.10), with an average time of 0.79 s compared to 0.24 s.

### **4.4 Discussion**

The results here demonstrate that extravasation of microbubbles can occur in brain slices at both 330 kHz and 1 MHz, at pressures and pulse lengths typical of those used in blood-brain barrier opening *in vivo*, and that dissolution of microbubbles after an ultrasound pulse is the primary mode of bubble destruction in perfused slices.

#### **Extravasation**

As shown in Figures 4.5 - 4.7, microbubbles can extravasate at parameters typical of those used *in vivo*. Extravasation is rare at low pressures, but becomes much more common at higher pressures. Higher pressures cause higher radiation forces, and so this trend is unsurprising. In Figure 4.7, there are no obvious differences between frequencies, which is likely because the matched MI ensures microbubbles exhibit relatively similar behaviours.

As discussed in Chapter 3, extravasation of microbubbles, if it were to occur *in vivo*, could plausibly be a mechanism of either BBB opening, tissue damage, or both. When comparing the relative probabilities of extravasation shown in Figures 4.6 and 4.7 with published results from *in vivo* studies, the rate at which extravasation of microbubbles occurs in the slices correlates relatively well with the relative rate of erythrocyte extravasation observed in *in vivo* studies of animals sonicated at similar parameters, with a mechanical index of approximately 0.2 and 0.4 generally appearing to be safe, but damage significantly increasing at higher pressures (Fan et al. 2016; McMahon et al. 2020; Morse et al. 2019; Shen et al. 2016; Shin et al. 2018). It is therefore plausible that microbubble extravasation could be a cause of vessel perforation and therefore erythrocyte extravasation *in vivo*.

While erythrocyte extravasation from small blood vessels following histological examination is potentially concerning, very small haemorrhages resulting from sparsely distributed micrometre-sized pores created by bubbles in very small microvessels are unlikely to be large enough to be observable on an MRI scan or to directly generate symptoms in a patient or animal. In conditions

with extremely poor prognoses, such as glioblastoma (Van Tellingen et al. 2015) or diffuse intrinsic pontine glioma (DIPG), any potential damage caused by extravasation of microbubbles may be an acceptable price to pay for increased permeability and distribution of drugs that this may enable. Whether this is also the case in diseases with much slower progressions, such as Alzheimer's Disease, is less clear, and would depend on the precise extent of the damage, and the effects this may have on the brain, which are difficult to predict.

As mentioned in Chapter 3, extravasation of microbubbles is plausible as a mechanism of BBB opening, as it necessarily involves creating pores in microvessel walls to enable the passage of microbubbles, which are most probably also large enough to allow almost any therapeutic through. However, in this study, extravasation primarily occurred at pressures (0.6 and 0.8 MPa) that were above the likely pressure threshold for brain drug delivery *in vivo* (around 0.3-0.6 MPa at frequencies close to 1 MHz (Choi et al. 2010; McDannold et al. 2008; Nhan et al. 2013)). Therefore, extravasation is unlikely to be occurring when BBB opening is being performed at low pressures that are generally considered to be safe.

Many studies have observed a sensitivity of opening to molecular size (Chen and Konofagou 2014). This is difficult to explain through bubble extravasation, as a micrometre-sized pore created by a bubble should be large enough to allow almost any therapeutic to pass through. While extravasation may be one component of BBB opening under certain parameters, it is therefore highly unlikely to be the dominant mechanism of drug delivery.

### **Dissolution**

Figure 4.10 indicates that, in the situation observed here, the probability of microbubble dissolution is not obviously influenced by choice of pulse sequence. It is however strongly dependent on ultrasound pressure amplitude.



Dissolution is likely to be related to disruption of the microbubble shell. When microbubbles are exposed to ultrasound above a certain pressure, even if this is only for a short period, this causes a breakup of the shell (Marmottant et al. 2005), exposing the gas inside to the surroundings. While this is assumed to be reversible, it is plausible that an expansion of the bubble beyond the breakup radius could cause permanent changes to the shell structure. It is therefore reasonable to expect that bubble dissolution should be dependent on maximum pressure amplitude, and less strongly pulse duration.

Gas escape is determined by the properties of the gas, and surrounding liquid (such as diffusion coefficient of the gas or gas saturation of the surrounding liquids), and happens on timescales of the order of hundreds of milliseconds (Borden et al. 2005). Therefore, splitting a single 10 ms pulse into shorter pulses does not appear to increase the lifetime of the bubble. RasP therefore is unlikely to increase the area over which the mechanical stresses are applied by each individual bubble *in vivo*. The improved uniformity of cavitation activity observed *in vivo* (Pouliopoulos et al. 2016) may have been caused primarily by reduced secondary forces between the bubbles, resulting in lower levels of coalescence. Coalescence is unlikely in microvessels due to the very large separations between bubbles. This may be more significant in larger vessels however.

### Limitations

As described in Chapter 3, there are many differences between the slice environment and an *in vivo* setting, including the replacement of the blood, lack of blood pressure and flow, differences in cellular activity in an *ex vivo* environment, and differences in brain physiology between juvenile rats and adults. The lack of blood is likely to be especially significant for the dissolution studies, as the gas concentrations are unlikely to be similar to that of blood. The absolute measurements of dissolution are therefore of unclear relevance, but trends can still be assessed.

When comparing the pressures used here with those stated in *in vivo* studies, it is important to be mindful of the different ways in which these values were measured. In some *in vivo* studies,

pressures are measured without the animal in situ, and so the actual pressures experienced by the bubbles within the brain will most likely be lower, due to reflection and attenuation through the skull. The comparisons made here may therefore be overestimating which pressures in the slices are equivalent to published *in vivo* experiments.

In the analysis of the videos, there is occasionally some uncertainty in categorising whether a bubble had left the vessel. This is because the boundary of the vessel is difficult to define precisely, because they are collapsed due to the lack of blood flow. This was often not a major concern, because bubbles usually moved quite significant distances from the vessel, making it easy to categorise. To improve the reliability of the categorisation of extravasation, this was performed by two independent observers.

During sonications using RaSP, microbubbles often moved noticeable distances within the vessels. However, these were much less than those observed during long pulses. During long pulses, microbubbles usually moved quite long distances from the vessel through the parenchyma. Because bubbles travelled much shorter periods during RaSP, it was very difficult to tell whether they had penetrated the vessel wall, as much greater precision was required in determining the location of the vessel boundary on the high-speed videos, and this was therefore not investigated in depth. This is a potential benefit of RaSP, however, as, even if bubbles did extravasate, they would not move as far into the tissue as with a 10 ms pulse of the same maximum pressure amplitude.

### **4.5 Conclusions**

As shown in Chapter 3, extravasation of microbubbles from microvessels in acute brain slices can occur at ultrasound parameters typical of those used in BBB opening. Extravasation does not occur at low pressures (0.2 MI), but becomes increasingly common with higher ultrasound pressure amplitudes. Probability of extravasation at 330 kHz appears to be relatively similar to the probabilities observed at equivalent mechanical indices at 1 MHz.

If extravasation is an important cause of tissue damage, optimal calibration of ultrasound pressure within the skull would be important. It is however plausible that extravasation of microbubbles may enhance distribution of drugs through the parenchyma, and so may be beneficial in specific clinical scenarios. Using shorter pulses may also be an effective way to reduce the probability of extravasation, although it is also important to remember that high-amplitude short pulses can still cause vessel rupture without microbubble extravasation (Chen et al. 2010). There are therefore important questions to be asked about the degree of potential damage to tissue that is acceptable in relation to the probability and spatial extent of drug delivery.

Microbubbles can also be destroyed by exposure to ultrasound. At pressures used here, this typically occurs after the pulse, due to dissolution of the gas. RaSP sequences do not reduce the probability of bubble dissolution in microvessels, although they may increase the time taken for bubbles to dissolve.

The slice platform opens up a wide range of potential avenues for future work. To better improve our understanding of the relationships between microbubble dynamics and bioeffects in the brain, more biological investigations could be performed to analyse the effects on the blood brain barrier in more detail. The results from the slices could then more accurately be used to make quantitative predictions of effects for *in vivo* studies, to validate the relationship between *ex vivo* and *in vivo* phenomena.

## Chapter 5: Conclusions

Since the technique was first demonstrated 20 years ago, focussed ultrasound and microbubble-induced blood-brain barrier opening has developed rapidly through *in vivo* studies into clinical trials. Yet despite these successes, many unanswered questions remain regarding the nature of the mechanisms of the technique, and of the fundamental behaviours of microbubbles within the brain when exposed to ultrasound pulses.

This thesis aimed to improve our understanding of some of these phenomena. Through experimental investigation of microbubble behaviours within artificial and *ex vivo* tissues, the results presented here provide indications of bubble behaviours that may be significant during brain therapy, either as part of various mechanisms of drug delivery, or as potential causes of tissue damage. These may provide a useful basis for future studies to answer fundamental questions in more detail.

In Chapter 2, in the controlled environment of a soft tissue-mimicking hydrogel, the primary radiation force on a microbubble is shown to be a significant way in which microbubbles can exert forces on surrounding tissue, when exposed to ultrasound pulses typical of those used *in vivo*. Microbubbles were able to reversibly deform gels by several micrometres, indicating this as a potentially significant contributor to the stresses microbubbles exert on tissue, in addition to their volumetric oscillations which have received greater attention in previous studies.

In Chapter 3, microbubbles were observed under sonication within intact microvessels in live brain tissue. Oscillating microbubbles were shown to exert mechanical stresses on brain tissues through a variety of mechanisms. On microsecond timescales oscillating microbubbles were shown to periodically deform the walls of microvessels at the ultrasound driving frequency. Microbubbles could also displace tissues several micrometres beyond the vessel boundary. A new phenomenon of

microbubble extravasation from small microvessels, due to the primary radiation force, was described.

In Chapter 4, extravasation was investigated in more detail, and was shown to be rare at the lower range of ultrasound pressures typically used *in vivo*, but much more common towards the higher end. In addition, dissolution of microbubbles following an ultrasound pulse was investigated. Probability of dissolution was shown to be linked to mechanical index, but not obviously linked to pulse length. These results have implications for the design of pulse sequences in drug delivery studies, in order to maximise the duration and spatial extent of effects caused by each bubble.

Overall, the results from this thesis provide a more detailed and specific insight into potential physical mechanisms of Blood-Brain Barrier opening than have been achieved in previous *in vitro* studies, or *ex vivo* studies in other tissue types. Previous studies have emphasised the significance of disruption of tight junctions between endothelial cells and transcytosis, but this thesis demonstrates that the effects of microbubbles may not be confined to the endothelial cells. Distension of vessels and mechanical stimulation of surrounding tissues may stimulate endogenous mechanotransduction pathways that cause the brain to modulate the permeability of the BBB. Additionally, extravasation of microbubbles at higher pressures creates pores to allow drugs to pass through, and may enhance drug distribution within the tissues.

### **Future work**

In Chapter 2, microbubbles were shown to indent into the walls of hydrogels when exposed to therapeutic ultrasound pulses. The rate and extent of indentation were used to extract properties of the system. These experiments could be built upon in several ways.

To improve the reliability of the parameters extracted from the indentation curves, a better measurement of the properties of the gels could be acquired, using different techniques that may be more temporally and spatially relevant to the bubbles. This may include shear wave imaging (to

measure elasticity on shorter time scales), or nanoindentation (to measure elasticity on the spatial scale experienced by bubbles).

The gels could be modified to make them more relevant to an *in vivo* setting, such as by coating the channel with a layer of endothelial cells. This could then be used to investigate biological effects of microbubble indentation on endothelial cells specifically, in a controlled setting.

The relationship between indentation depths and ultrasound parameters such as frequency and, pulse sequences could also be investigated to design ways of reducing or increasing the indentation depths achieved. Monodisperse bubbles could also be used to reduce variation in indentation depth and investigate more deeply the causes of variation in results that is observed.

One of the most potentially significant outcomes of this thesis is the demonstration in Chapters 3 and 4 that acute brain slices offer an effective way of observing microbubbles within brain tissue under sonication. This thesis utilises the platform to investigate potential physical mechanisms of BBB opening. There are several potential refinements to this approach that could improve the broader relevance of the observations

Micropipetting of single bubbles into the vessels of the slices was attempted here but was not successful. In principle, however, this should be possible (Kozlov et al. 2006), and with refinement of the technique, it may be possible to ensure that only a single microbubble is present in the field of view of the lens, and the focus of the transducer. This would enable interactions between bubbles to be controlled for and may be very valuable for biological or acoustic studies.

In the experiments performed here, the blood within the tissue is replaced with a solution based on SonoVue. The lack of red blood cells in particular may have affected the behaviour of bubbles, and so using a more physiologically perfusate may be valuable in future studies.

It would be extremely valuable to be able to confirm whether the behaviours observed in the slices are occurring in *in vivo* studies. One method would be to detect the acoustic emissions of each

bubble using a hydrophone and see whether there are any characteristics of the signal that correlate with specific behaviours observed under the microscope. It is possible to detect emissions from a single bubble using a typical hydrophone (Johnston et al. 2014). This may be useful as a way of linking observations in the slices to behaviour occurring *in vivo*. If a reliable acoustic signature can be identified for specific behaviours then this could be sought out in traces from *in vivo* studies.

Another more detailed method would be to track bubbles *in vivo* before and very shortly after ultrasound exposure using extremely high spatial resolution confocal or multiphoton imaging (combined with fluorescently-tagged microbubbles (Hosny et al. 2013), or super resolution acoustic imaging of single bubbles (Christensen-Jeffries et al. 2015; Errico et al. 2015). These methods could be used to identify if any bubbles moved from within to outside vessels during sonication. This may be quite challenging to perform experimentally however, and the spatial resolution required of approximately 10  $\mu\text{m}$  is likely to be close to the boundary of current technologies.

With additional equipment and biological tools, these physical phenomena described in this thesis could be directly linked to biological activity within the tissue. For instance, this could include using staining, or tissue from transgenic animals with fluorescent tags, to investigate tight junctional integrity before and after pulses (Marchiando et al. 2010). Additionally, observations of signalling pathways, such as calcium waves (Beekers et al. 2020), due to the mechanical stimulation caused by the microbubbles, could be performed using similar real-time fluorescence approaches to observe broader biological stimulation.

### Conclusion

This thesis has demonstrated a wide range of physical effects microbubbles may have on their surroundings during ultrasound therapy, as well as introducing acute brain slices as a valuable method to investigate microbubble behaviours in the microvasculature. These results, and future studies that may build upon them, have potential value in informing the optimisation of brain therapies in a clinical setting, and thus improving outcomes for patients with neurological disorders.

# References

- Abbott NJ. Astrocyte–endothelial interactions and blood–brain barrier permeability. *J Anat* 2002;629–638.
- Abbott NJ, Patabendige AAK, Dolman DEM, Yusof SR, Begley DJ. Structure and function of the blood–brain barrier. *Neurobiol Dis Elsevier Inc.*, 2010;37:13–25. Available from: <http://www.ncbi.nlm.nih.gov/pubmed/19664713>
- Abbott NJ, Rönnbäck L, Hansson E. Astrocyte – endothelial interactions at the blood – brain barrier. *Nat Rev Neurosci* 2006;7:41–53.
- Abou-Elkacem L, Bachawal S V, Willmann JK. Ultrasound molecular imaging : Moving toward clinical translation. *Eur J Radiol Elsevier Ireland Ltd*, 2015;84:1685–1693. Available from: <http://dx.doi.org/10.1016/j.ejrad.2015.03.016>
- Abraham A, Meng Y, Llinas M, Huang Y, Hamani C, Mainprize T, Aubert I, Heyn C, Black SE, Hynynen K, Lipsman N, Zinman L. First-in-human trial of blood–brain barrier opening in amyotrophic lateral sclerosis using MR-guided focused ultrasound. *Nat Commun Springer US*, 2019;10:1–9. Available from: <http://dx.doi.org/10.1038/s41467-019-12426-9>
- Angelov L, Doolittle ND, Kraemer DF, Siegal T, Barnett GH, Peereboom DM, Stevens G, McGregor J, Jahnke K, Lacy CA, Hedrick NA, Shalom E, Ference S, Bell S, Sorenson L, Tyson RM, Haluska M, Neuwelt EA. Blood-brain barrier disruption and intra-arterial methotrexate-based therapy for newly diagnosed primary CNS lymphoma: A multi-institutional experience. *J Clin Oncol* 2009;27:3503–3509.
- Apfel RE. Sonic effervescence: A tutorial on acoustic cavitation. *J Acoust Soc Am* 1997;101:1227–1237. Available from: <http://asa.scitation.org/doi/10.1121/1.418130>
- Ballabh P, Braun A, Nedergaard M. The blood-brain barrier: An overview: Structure, regulation, and clinical implications. *Neurobiol Dis* 2004;16:1–13.
- Barnett SB, Ter Haar GR, Ziskin MC, Rott HD, Duck FA, Maeda K. International recommendations and guidelines for the safe use of diagnostic ultrasound in medicine. *Ultrasound Med Biol* 2000;26:355–366.
- Bartanusz V, Jezova D, Alajajian B, Digicaylioglu M. The blood-spinal cord barrier: Morphology and clinical implications. *Ann Neurol* 2011;70:194–206.
- Beekers I, Mastik F, Beurskens R, Tang PY, Vegter M, van der Steen AFW, de Jong N, Verweij MD, Kooiman K. High-resolution imaging of intracellular calcium fluctuations caused by oscillating microbubbles. *Ultrasound Med Biol* 2020;8:2017–2029.
- Bennett HS, Luft JH, Hampton JC. Morphological classifications of vertebrate blood capillaries. *Am J Physiol* 1959;196:381–390.
- Bhatnagar S, Kwan JJ, Shah AR, Coussios CC, Carlisle RC. Exploitation of sub-micron cavitation nuclei to enhance ultrasound-mediated transdermal transport and penetration of vaccines. *J Control Release The Authors*, 2016;238:22–30. Available from: <http://dx.doi.org/10.1016/j.jconrel.2016.07.016>
- Blaber J, Adair B, Antoniou A. Ncorr: Open-Source 2D Digital Image Correlation Matlab Software. *Exp Mech* 2015;55:1105–1122.
- Blue LM, Guidi F, Vos HJ, Slagle CJ, Borden MA, Tortoli P. Plane-wave contrast imaging: A radiation



- 
- force point of view. *IEEE Trans Ultrason Ferroelectr Freq Control* IEEE, 2018;65:2296–2300.
- Borden MA, Kruse DE, Caskey CF, Zhao S, Dayton PA, Ferrara KW. Influence of lipid shell physicochemical properties on ultrasound-induced microbubble destruction. *IEEE Trans Ultrason Ferroelectr Freq Control* IEEE, 2005;52:1992–2002.
- Borden MA, Martinez G V., Ricker J, Tsvetkova N, Longo M, Gillies RJ, Dayton PA, Ferrara KW. Lateral phase separation in lipid-coated microbubbles. *Langmuir* 2006;22:4291–4297.
- Bude RO, Adler RS. An easily made, low-cost, tissue-like ultrasound phantom material. *J Clin Ultrasound* 1995;23:271–273.
- Burgess A, Cho EE, Shaffaf L, Nhan T, Poon C, Hynynen K. The use of two-photon microscopy to study the biological effects of focused ultrasound on the brain. *Multiphot Microsc Biomed Sci XII* 2012;8226:822642.
- Burgess A, Nhan T, Moffatt C, Klibanov AL, Hynynen K. Analysis of focused ultrasound-induced blood-brain barrier permeability in a mouse model of Alzheimer's disease using two-photon microscopy. *J Control Release Elsevier B.V.*, 2014;192:243–248. Available from: <http://dx.doi.org/10.1016/j.jconrel.2014.07.051>
- Burgess A, Shah K, Hough O, Hynynen K. Focused ultrasound-mediated drug delivery through the blood-brain barrier. *Expert Rev Neurother* 2015;15:477–91. Available from: <http://www.ncbi.nlm.nih.gov/pubmed/25936845> <http://www.pubmedcentral.nih.gov/articlerender.fcgi?artid=PMC4702264>
- Bushberg JT, Seibert JA, Leidholdt EM, Boone JM. The essential physics of medical imaging.
- Buskila Y, Breen PP, Tapson J, Van Schaik A, Barton M, Morley JW. Extending the viability of acute brain slices. *Sci Rep* 2014;4:4–10.
- Cabezas R, Ávila M, Gonzalez J, El-Bachá RS, Báez E, García-Segura LM, Coronel JCJ, Capani F, Cardona-Gomez GP, Barreto GE. Astrocytic modulation of blood brain barrier: Perspectives on Parkinson's disease. *Front Cell Neurosci* 2014;8:1–11.
- Cafarelli A, Verbeni A, Poliziani A, Dario P, Menciasci A, Ricotti L. Tuning acoustic and mechanical properties of materials for ultrasound phantoms and smart substrates for cell cultures. *Acta Biomater Acta Materialia Inc.*, 2017;49:368–378. Available from: <http://dx.doi.org/10.1016/j.actbio.2016.11.049>
- Carpentier A, Canney M, Vignot A, Reina V, Beccaria K, Horodyckid C, Karachi C, Leclercq D, Lafon C, Chapelon JY, Capelle L, Cornu P, Sanson M, Hoang-Xuan K, Delattre JY, Idhahbi A. Clinical trial of blood-brain barrier disruption by pulsed ultrasound. *Sci Transl Med* 2016;8.
- Caskey CF, Kruse DE, Dayton PA, Kitano TK, Ferrara KW. Microbubble oscillation in tubes with diameters of 12, 25, and 195 microns. *Appl Phys Lett American Institute of Physics*, 2006 [cited 2018 Jan 19];88:033902. Available from: <http://aip.scitation.org/doi/10.1063/1.2164392>
- Caskey CF, Qin S, Dayton PA, Ferrara KW. Microbubble tunneling in gel phantoms. *J Acoust Soc Am* 2009;125:EL183–EL189. Available from: <http://scitation.aip.org/content/asa/journal/jasa/125/5/10.1121/1.3097679> <http://pubs.aip.org/jasa/article/doi/10.1121/1.3097679>
- Caskey CF, Stieger SM, Qin S, Dayton PA, Ferrara KW. Direct observations of ultrasound microbubble contrast agent interaction with the microvessel wall. *J Acoust Soc Am* 2007;122:1191–1200. Available from: <http://asa.scitation.org/doi/10.1121/1.2747204>
-

- 
- Chen H, Brayman AA, Bailey MR, Matula TJ. Blood vessel rupture by cavitation. *Urol Res* 2010;38:321–326.
- Chen H, Brayman AA, Matula TJ. Characteristic microvessel relaxation timescales associated with ultrasound-activated microbubbles. *Appl Phys Lett* 2012;101.
- Chen H, Konofagou EE. The size of blood-brain barrier opening induced by focused ultrasound is dictated by the acoustic pressure. *J Cereb Blood Flow Metab* 2014;34:1197–1204.
- Chen H, Kreider W, Brayman AA, Bailey MR, Matula TJ. Blood vessel deformations on microsecond time scales by ultrasonic cavitation. *Phys Rev Lett* 2011;106:1–4.
- Chen X, Leeman JE, Wang J, Pacella JJ, Villanueva FS. New insights into mechanisms of sonothrombolysis using ultra-high-speed imaging. *Ultrasound Med Biol* 2014;40:258–262.
- Choi JJ, Feshitan JA, Baseri B, Wang S, Tung Y, Borden MA, Konofagou EE. Microbubble-Size Dependence of Focused ultrasound-induced blood-brain barrier opening in mice. *IEEE Trans Biomed Eng* 2010;57:145–154.
- Choi JJ, Selert K, Vlachos F, Wong A, Konofagou EE. Noninvasive and localized neuronal delivery using short ultrasonic pulses and microbubbles. *Proc Natl Acad Sci U S A* 2011;108:16539–16544.
- Chomas JE, Dayton P, Alien J, Morgan K, Ferrara KW. Mechanisms of contrast agent destruction. *IEEE Trans Ultrason Ferroelectr Freq Control* 2001a;48:232–248.
- Chomas JE, Dayton P, May D, Ferrara K. Threshold of fragmentation for ultrasonic contrast agents. *J Biomed Opt* 2001b;6:141.
- Christensen-Jeffries K, Browning RJ, Tang M-X, Dunsby C, Eckersley RJ. In Vivo Acoustic Super-Resolution and Super-Resolved Velocity Mapping Using Microbubbles. *IEEE Trans Med Imaging* 2015;34:433–440. Available from: <http://ieeexplore.ieee.org/lpdocs/epic03/wrapper.htm?arnumber=6908009>
- Cleve S, Inserra C, Prentice P. Contrast Agent Microbubble Jetting during Initial Interaction with 200-kHz Focused Ultrasound. *Ultrasound Med Biol* 2019;45:3075–3080.
- Collis J, Manasseh R, Liovic P, Tho P, Ooi A, Petkovic-duran K. Cavitation microstreaming and stress fields created by microbubbles. *Ultrasonics Elsevier B.V.*, 2010;50:273–279. Available from: <http://dx.doi.org/10.1016/j.ultras.2009.10.002>
- Conversano F, Franchini R, Lay-Ekuakille A, Casciaro S. In vitro evaluation and theoretical modeling of the dissolution behavior of a microbubble contrast agent for ultrasound imaging. *IEEE Sens J* 2012;12:496–503.
- Cosgrove D. Ultrasound contrast agents: An overview. *Eur J Radiol* 2006;60:324–330.
- Cox DJ, Thomas JL. Ultrasound-induced dissolution of lipid-coated and uncoated gas bubbles. *Langmuir* 2010;26:14774–14781.
- Cox DJ, Thomas JL. Rapid Shrinkage of Lipid-Coated Bubbles in Pulsed Ultrasound. *Ultrasound Med Biol* 2013;39:466–474.
- Crake C, Owen J, Smart S, Coviello C, Coussios CC, Carlisle R, Stride E. Enhancement and Passive Acoustic Mapping of Cavitation from Fluorescently Tagged Magnetic Resonance-Visible Magnetic Microbubbles In Vivo. *Ultrasound Med Biol* 2016;42:3022–3036.
- Dayton PA, Allen JS, Ferrara KW. The magnitude of radiation force on ultrasound contrast agents. *J Acoust Soc Am* 2002;112:2183–2192. Available from:
-

- 
- <http://asa.scitation.org/doi/10.1121/1.1509428>
- De Cock I, Zagato E, Braeckmans K, Luan Y, de Jong N, De Smedt SC, Lentacker I. Ultrasound and microbubble mediated drug delivery: acoustic pressure as determinant for uptake via membrane pores or endocytosis. *J Control Release Elsevier B.V.*, 2015;197:20–28. Available from: <http://dx.doi.org/10.1016/j.jconrel.2014.10.031>
- De Saint Victor M, Crake C, Coussios CC, Stride E. Properties, characteristics and applications of microbubbles for sonothrombolysis. *Expert Opin Drug Deliv* 2014;11:187–209.
- Deng J, Huang Q, Wang F, Liu Y, Wang Z, Wang Z, Zhang Q, Lei B, Cheng Y. The role of caveolin-1 in blood-brain barrier disruption induced by focused ultrasound combined with microbubbles. *J Mol Neurosci* 2012;46:677–687.
- Dick EA, Gedroyc WMW. ExAblate® magnetic resonance-guided focused ultrasound system in multiple body applications. *Expert Rev Med Devices* 2010;7:589–597.
- Dingledine R, Dodd J, Kelly JS. The in vitro brain slice as a useful neurophysiological preparation for intracellular recording. *J Neurosci Methods* 1980;2:323–362.
- Doinikov AA, Bienaimé Di, Gonzalez-Avila SR, Ohi CDi, Marmottant P. Nonlinear dynamics of two coupled bubbles oscillating inside a liquid-filled cavity surrounded by an elastic medium. *Phys Rev E American Physical Society*, 2019;99:1–16.
- Doinikov AA, Bouakaz A. Review of shell models for contrast agent microbubbles. *IEEE Trans Ultrason Ferroelectr Freq Control* 2011;58:981–993.
- Engler A, Bacakova L, Newman C, Hategan A, Griffin M, Discher D. Substrate Compliance versus Ligand Density in Cell on Gel Responses. *Biophys J Elsevier*, 2004;86:617–628. Available from: [http://dx.doi.org/10.1016/S0006-3495\(04\)74140-5](http://dx.doi.org/10.1016/S0006-3495(04)74140-5)
- Erpelding TN, Hollman KW, O'Donnell M. Bubble-based acoustic radiation force elasticity imaging. *Ultrason Ferroelectr Freq Control IEEE Trans* 2005;52:971–979.
- Errico C, Pierre J, Pezet S, Desailly Y, Lenkei Z, Couture O, Tanter M. Ultrafast ultrasound localization microscopy for deep super-resolution vascular imaging. *Nature Nature Publishing Group*, 2015 [cited 2018 Jan 18];527:499–502. Available from: <http://www.nature.com/doi/10.1038/nature16066>
- Faez T, Emmer M, Kooiman K, Versluis M, Van Der Steen A, De Jong N. 20 Years of Ultrasound Contrast Agent Modeling. *IEEE Trans Ultrason Ferroelectr Freq Control* 2013;60:7–20.
- Fan CH, Chang EL, Ting CY, Lin YC, Liao EC, Huang CY, Chang YC, Chan HL, Wei KC, Yeh CK. Folate-conjugated gene-carrying microbubbles with focused ultrasound for concurrent blood-brain barrier opening and local gene delivery. *Biomaterials Elsevier Ltd*, 2016;106:46–57. Available from: <http://dx.doi.org/10.1016/j.biomaterials.2016.08.017>
- Ferrara KW, Borden MA, Zhang H. Lipid-shelled vehicles: Engineering for ultrasound molecular imaging and drug delivery. *Acc Chem Res* 2009;42:881–892.
- Feshitan JA, Chen CC, Kwan JJ, Borden MA. Microbubble size isolation by differential centrifugation. *J Colloid Interface Sci Elsevier Inc.*, 2009;329:316–324. Available from: <http://dx.doi.org/10.1016/j.jcis.2008.09.066>
- Fini M, Tyler WJ. Transcranial focused ultrasound : a new tool for non-invasive neuromodulation. *Int Rev Psychiatry* 2017;0261.
- Fletcher SMP, Choi M, Ramesh R, O'Reilly MA. Focused Ultrasound-Induced Blood–Spinal Cord
-

- 
- Barrier Opening Using Short-Burst Phase-Keying Exposures in Rats: A Parameter Study. *Ultrasound Med Biol* 2021;47:1747–1760.
- Food and Drug Administration. Marketing Clearance of Diagnostic Ultrasound Systems and Transducers. 2019;64. Available from: <https://www.regulations.gov>
- Frey MT, Engler A, Discher DE, Lee J, Wang YL. Microscopic Methods for Measuring the Elasticity of Gel Substrates for Cell Culture: Microspheres, Microindenters, and Atomic Force Microscopy. *Methods Cell Biol* 2007;83:47–65.
- Frinking PJA, Tardy I, Théraulaz M, Arditi M, Powers J, Pochon S, Tranquart F. Effects of Acoustic Radiation Force on the Binding Efficiency of BR55, a VEGFR2-Specific Ultrasound Contrast Agent. *Ultrasound Med Biol* 2012;38:1460–1469.
- Garbin V, Cojoc D, Ferrari E, Di Fabrizio E, Overvelde MLJ, Van Der Meer SM, De Jong N, Lohse D, Versluis M. Changes in microbubble dynamics near a boundary revealed by combined optical micromanipulation and high-speed imaging. *Appl Phys Lett* 2007;90.
- Garbin V, Dollet B, Overvelde M, Cojoc D, Di Fabrizio E, van Wijngaarden L, Prosperetti A, de Jong N, Lohse D, Versluis M. History force on coated microbubbles propelled by ultrasound. *Phys Fluids* 2009;21.
- Gordon GRJ, Mulligan SJ, MacVicar BA. Astrocyte Control of the Cerebrovasculature. *Glia* 2007;55:1214–1221.
- Gust J, Hay KA, Hanafi LA, Li D, Myerson D, Gonzalez-Cuyar LF, Yeung C, Liles WC, Wurfel M, Lopez JA, Chen J, Chung D, Baker SH, Ozpolat T, Fink KR, Riddell SR, Maloney DG, Turtle CJ. Endothelial activation and blood–brain barrier disruption in neurotoxicity after adoptive immunotherapy with CD19 CAR-T cells. *Cancer Discov* 2017;7:1404–1419.
- Hawkins BT, Davis TP. The Blood-Brain Barrier/Neurovascular Unit in Health and Disease. *Pharmacol Rev* 2005;57:173–185.
- Helfield B. A Review of Phospholipid Encapsulated Ultrasound Contrast Agent Microbubble Physics. *Ultrasound Med Biol Elsevier Inc.*, 2019;45:282–300. Available from: <https://doi.org/10.1016/j.ultrasmedbio.2018.09.020>
- Helfield B, Chen X, Watkins SC, Villanueva FS. Biophysical insight into mechanisms of sonoporation. *Proc Natl Acad Sci U S A* 2016;113:9983–9988.
- Helfield BL, Leung BYC, Goertz DE. The influence of compliant boundary proximity on the fundamental and subharmonic emissions from individual microbubbles. *J Acoust Soc Am* 2014;136:EL40–EL46. Available from: <http://asa.scitation.org/doi/10.1121/1.4885544>
- Högman M, Mörk AC, Roomans GM. Hypertonic saline increases tight junction permeability in airway epithelium. *Eur Respir J* 2002;20:1444–1448.
- Hosny NA, Mohamedi G, Rademeyer P, Owen J, Wu Y, Tang MX, Eckersley RJ, Stride E, Kuimova MK. Mapping microbubble viscosity using fluorescence lifetime imaging of molecular rotors. *Proc Natl Acad Sci U S A* 2013;110:9225–9230.
- Hunt Bobo R, Laske DW, Akbasak A, Morrison PF, Dedrick RL, Oldfield EH. Convection-enhanced delivery of macromolecules in the brain. *Proc Natl Acad Sci U S A* 1994;91:2076–2080.
- Hynynen K, McDannold N, Vykhodtseva N, Jolesz FA. Noninvasive MR Imaging–guided Focal Opening of the Blood-Brain Barrier in Rabbits. *Radiology* 2001;220:640–646. Available from: <http://pubs.rsna.org/doi/10.1148/radiol.2202001804>
-

- 
- Iadecola C. The Neurovascular Unit Coming of Age: A Journey through Neurovascular Coupling in Health and Disease. *Neuron Elsevier Inc.*, 2017;96:17–42. Available from: <https://doi.org/10.1016/j.neuron.2017.07.030>
- Idbaih A, Canney M, Belin L, Desseaux C, Vignot A, Bouchoux G, Asquier N, Law-Ye B, Leclercq D, Bissery A, De Rycke Y, Trosch C, Capelle L, Sanson M, Hoang-Xuan K, Dehais C, Houillier C, Laigle-Donadey F, Mathon B, André A, Lafon C, Chapelon JY, Delattre JY, Carpentier A. Safety and feasibility of repeated and transient blood-brain barrier disruption by pulsed ultrasound in patients with recurrent glioblastoma. *Clin Cancer Res* 2019;25:3793–3801.
- Ilinskii YA, Meegan GD, Zabolotskaya EA, Emelianov SY. Gas bubble and solid sphere motion in elastic media in response to acoustic radiation force. *J Acoust Soc Am* 2005;117:2338–2346. Available from: <http://asa.scitation.org/doi/10.1121/1.1863672>
- Jamburidze A. Ultrasound-driven dynamics of microbubbles confined in tissue-mimicking phantoms. Imperial College London, 2019.
- Jamburidze A, De Corato M, Huerre A, Pommella A, Garbin V. High-frequency linear rheology of hydrogels probed by ultrasound-driven microbubble dynamics. *Soft Matter Royal Society of Chemistry*, 2017;13:3946–3953. Available from: <http://xlink.rsc.org/?DOI=C6SM02810A>
- Jia C, Xu L, Han T, Cai P, Yu ACH, Qin P. Generation of reactive oxygen species in heterogeneously sonoporated cells by microbubbles with single-pulse ultrasound. *Ultrasound Med Biol Elsevier Inc.*, 2018;44:1074–1085. Available from: <https://doi.org/10.1016/j.ultrasmedbio.2018.01.006>
- Johnston K, Tapia-Siles C, Gerold B, Postema M, Cochran S, Cuschieri A, Prentice P. Periodic shock-emission from acoustically driven cavitation clouds: A source of the subharmonic signal. *Ultrasonics Elsevier B.V.*, 2014;54:2151–2158. Available from: <http://dx.doi.org/10.1016/j.ultras.2014.06.011>
- Jones RM, Hynynen KR. Advances in acoustic monitoring and control of focused ultrasound-mediated increases in blood-brain barrier permeability. *Br J Radiol* 2019;92:1–13.
- Joshi CN, Jain SK, Murthy PSR. An optimized triphenyltetrazolium chloride method for identification of cerebral infarcts. *Brain Res Protoc* 2004;13:11–17.
- Kaneko Y, Maruyama T, Takegami K, Watanabe T, Mitsui H, Hanajiri K, Nagawa H, Matsumoto Y. Use of a microbubble agent to increase the effects of high intensity focused ultrasound on liver tissue. *Eur J Radiol* 2005;15:1415–1420.
- Karakatsani ME, Pouliopoulos A, Liu M, Jambawalikar SR, Konofagou EE. Contrast-free detection of focused ultrasound-induced blood-brain barrier opening using diffusion tensor imaging. *IEEE Trans Biomed Eng* 2020;9294:1–1.
- Karbowski J. Scaling of brain metabolism and blood flow in relation to capillary and neural scaling. *PLoS One* 2011;6.
- Karmur BS, Philteos J, Abbasian A, Zacharia BE, Lipsman N, Levin V, Grossman S, Mansouri A. Blood-Brain Barrier Disruption in Neuro-Oncology: Strategies, Failures, and Challenges to Overcome. *Front Oncol* 2020;10.
- Karpf S, Riche CT, Di Carlo D, Goel A, Zeiger WA, Suresh A, Portera-Cailliau C, Jalali B. Spectro-temporal encoded multiphoton microscopy and fluorescence lifetime imaging at kilohertz frame-rates. *Nat Commun Springer US*, 2020;11:1–9. Available from: <http://dx.doi.org/10.1038/s41467-020-15618-w>
- Kaster T, Sack I, Samani A. Measurement of the hyperelastic properties of ex vivo brain tissue slices. *J*

- 
- Biomech Elsevier, 2011;44:1158–1163. Available from:  
<http://dx.doi.org/10.1016/j.jbiomech.2011.01.019>
- Kaufmann BA, Wei K, Lindner JR. Contrast Echocardiography. *Curr Probl Cardiol* 2007;32:51–96.
- Khokhlova VA, Fowlkes JB, Roberts WW, Schade GR, Xu Z, Khokhlova TD, Hall TL, Maxwell AD, Wang YN, Cain CA. Histotripsy methods in mechanical disintegration of tissue: Towards clinical applications. *Int J Hyperth* 2015;31:145–162.
- Kiviniemi V, Korhonen V, Kortelainen J, Rytty S, Keinänen T, Tuovinen T, Isokangas M, Sonkajärvi E, Siniluoto T, Nikkinen J, Alahuhta S, Tervonen O, Turpeenniemi-Hujanen T, Myllylä T, Kuittinen O, Voipio J. Real-time monitoring of human blood-brain barrier disruption. *PLoS One* 2017;12:1–16.
- Kooiman K, van der Steen AFW, De Jong N. Role of Intracellular Calcium and Reactive Oxygen Species in Microbubble-Mediated Alterations of Endothelial Layer Permeability. *IEEE Trans Ultrason Ferroelectr Freq Control IEEE*, 2013;60:1811–1815.
- Koruk H, Choi JJ. Displacement of a bubble by acoustic radiation force into a fluid–tissue interface. *J Acoust Soc Am* 2018;143:2535–2540. Available from:  
<http://asa.scitation.org/doi/10.1121/1.5034175>
- Koruk H, Choi JJ. Displacement of a bubble located at a fluid-viscoelastic medium interface. *J Acoust Soc Am* 2019;145:EL410–EL416. Available from: <http://dx.doi.org/10.1121/1.5108678>
- Koruk H, El Ghamrawy A, Pouliopoulos AN, Choi JJ. Acoustic particle palpation for measuring tissue elasticity. *Appl Phys Lett* 2015;107.
- Kovacs R, Papageorgiou I, Heinemann U. Slice Cultures as a Model to Study Neurovascular Coupling and Blood Brain Barrier In Vitro. 2011;2011.
- Kozlov AS, Angulo MC, Audinat E, Charpak S. Target cell-specific modulation of neuronal activity by astrocytes. *Proc Natl Acad Sci* 2006;103.
- Kuitunen H, Tokola S, Siniluoto T, Isokangas M, Sonkajärvi E, Alahuhta S, Turpeenniemi-Hujanen T, Jantunen E, Nousiainen T, Vasala K, Kuittinen O. Promising treatment results with blood brain barrier disruption (BBBD) based immunochemotherapy combined with autologous stem cell transplantation (ASCT) in patients with primary central nervous system lymphoma (PCNSL). *J Neurooncol Springer US*, 2017;131:293–300. Available from:  
<http://dx.doi.org/10.1007/s11060-016-2293-8>
- Kwan J, Borden M. Microbubble shell break-up and collapse during gas exchange. *Proc - IEEE Ultrason Symp IEEE*, 2010a;:897–899.
- Kwan JJ, Borden MA. Microbubble dissolution in a multigas environment. *Langmuir* 2010b;26:6542–6548.
- Kwan JJ, Myers R, Coviello CM, Graham SM, Shah AR, Stride E, Carlisle RC, Coussios CC. Ultrasound-Propelled Nanocups for Drug Delivery. *Small* 2015;11:5305–5314.
- Leighton TG. The Acoustic Bubble. *J Acoust Soc Am* 1994;96:2616.
- Lelu S, Afadzi M, Berg S, Aslund AKO, Torp SH, Sattler W, De Davies CL. Primary porcine brain endothelial cells as in vitro model to study effects of ultrasound and microbubbles on blood-brain barrier function. *IEEE Trans Ultrason Ferroelectr Freq Control* 2017;64:281–290.
- Lentacker I, De Cock I, Deckers R, De Smedt SC, Moonen CTW. Understanding ultrasound induced sonoporation: Definitions and underlying mechanisms. *Adv Drug Deliv Rev Elsevier B.V.*,
-

- 2014;72:49–64. Available from: <http://dx.doi.org/10.1016/j.addr.2013.11.008>
- Lingeman JE, Mcateer JA, Gnessin E, Evan AP. Shock wave lithotripsy : advances in technology and technique. *Nat Rev Urol* Nature Publishing Group, 2009;6:660–670. Available from: <http://dx.doi.org/10.1038/nrurol.2009.216>
- Lipsman N, Meng Y, Bethune AJ, Huang Y, Lam B, Masellis M, Herrmann N, Heyn C, Aubert I, Boutet A, Smith GS, Hynynen K, Black SE. Blood–brain barrier opening in Alzheimer’s disease using MR-guided focused ultrasound. *Nat Commun* 2018;9:2336. Available from: <http://www.nature.com/articles/s41467-018-04529-6>
- Lukka H, Waldron T, Chin J, Mayhew L, Warde P, Winquist E, Rodrigues G, Shayegan B. High-intensity Focused Ultrasound for Prostate Cancer: A Systematic Review. *Clin Oncol* 2011;23:117–127.
- Lum AFH, Borden MA, Dayton PA, Kruse DE, Simon SI, Ferrara KW. Ultrasound radiation force enables targeted deposition of model drug carriers loaded on microbubbles. *J Control Release* 2006;111:128–134.
- Lyon PC, Gray MD, Mannaris C, Folkes LK, Stratford M, Campo L, Chung DYF, Scott S, Anderson M, Goldin R, Carlisle R, Wu F, Middleton MR, Gleeson F V., Coussios CC. Safety and feasibility of ultrasound-triggered targeted drug delivery of doxorubicin from thermosensitive liposomes in liver tumours (TARDOX): a single-centre, open-label, phase 1 trial. *Lancet Oncol* The Author(s). Published by Elsevier Ltd. This is an Open Access article under the CC BY license, 2018;19:1027–1039. Available from: [http://dx.doi.org/10.1016/S1470-2045\(18\)30332-2](http://dx.doi.org/10.1016/S1470-2045(18)30332-2)
- Lyu Z, Park J, Kim KM, Jin HJ, Wu H, Rajadas J, Kim DH, Steinberg GK, Lee W. A neurovascular-unit-on-a-chip for the evaluation of the restorative potential of stem cell therapies for ischaemic stroke. *Nat Biomed Eng* Springer US, 2021;5. Available from: <http://dx.doi.org/10.1038/s41551-021-00744-7>
- Macé E, Montaldo G, Cohen I, Baulac M, Fink M, Tanter M. Functional ultrasound imaging of the brain. *Nat Methods* Nature Publishing Group, 2011 [cited 2018 Jan 18];8:662–664. Available from: <http://www.nature.com/doifinder/10.1038/nmeth.1641>
- Mainprize T, Lipsman N, Huang Y, Meng Y, Bethune A, Ironside S, Heyn C, Alkins R, Trudeau M, Sahgal A, Perry J, Hynynen K. Blood-Brain Barrier Opening in Primary Brain Tumors with Non-invasive MR-Guided Focused Ultrasound: A Clinical Safety and Feasibility Study. *Sci Rep* Springer US, 2019;9:1–7. Available from: <http://dx.doi.org/10.1038/s41598-018-36340-0>
- Marchiando AM, Shen L, Vallen Graham W, Weber CR, Schwarz BT, Austin JR, Raleigh DR, Guan Y, Watson AJM, Montrose MH, Turner JR. Caveolin-1-dependent occludin endocytosis is required for TNF-induced tight junction regulation in vivo. *J Cell Biol* 2010;189:111–126.
- Marmottant P, van der Meer S, Emmer M, Versluis M, de Jong N, Hilgenfeldt S, Lohse D. A model for large amplitude oscillations of coated bubbles accounting for buckling and rupture. *J Acoust Soc Am* 2005;118:3499–3505. Available from: <http://asa.scitation.org/doi/10.1121/1.2109427>
- Martínez-Fernández R, Rodríguez-Rojas R, del Álamo M, Hernández-Fernández F, Pineda-Pardo JA, Dileone M, Alonso-Frech F, Foffani G, Obeso I, Gasca-Salas C, de Luis-Pastor E, Vela L, Obeso JA. Focused ultrasound subthalamotomy in patients with asymmetric Parkinson’s disease: a pilot study. *Lancet Neurol* 2018;17:54–63.
- Martynov S, Stride E, Saffari N. The natural frequencies of microbubble oscillation in elastic vessels. *J Acoust Soc Am* 2009;126:2963–2972. Available from: <http://asa.scitation.org/doi/10.1121/1.3243292>

- 
- Masuda K, Nakamoto R, Watarai N, Ren K, Taguchi Y, Kozuka T, Miyamoto Y, Kakimoto T, Enosawa S, Chiba T. Effect of existence of red blood cells in trapping performance of microbubbles by acoustic radiation force. *Jpn J Appl Phys* 2011;50.
- Mathias W, Tsutsui JM, Tavares BG, Fava AM, Aguiar MOD, Borges BC, Oliveira MT, Soeiro A, Nicolau JC, Ribeiro HB, Chiang HP, Sbrana JCN, Morad A, Goldsweig A, Rochitte CE, Lopes BBC, Ramirez JAF, Kalil Filho R, Porter TR. Sonothrombolysis in ST-Segment Elevation Myocardial Infarction Treated With Primary Percutaneous Coronary Intervention. *J Am Coll Cardiol* 2019;73:2832–2842.
- McDannold N, Vkhodtseva N, Hynynen K. Blood-brain barrier disruption induced by focused ultrasound and circulating preformed microbubbles appears to be characterized by the mechanical index. *Ultrasound Med Biol* 2008;34:834–840.
- McDannold N, Vkhodtseva N, Hynynen K. Targeted disruption of the blood-brain barrier with focused ultrasound: Association with cavitation activity. *Phys Med Biol* 2006;51:793–807.
- McKee CT, Last JA, Russell P, Murphy CJ. Indentation Versus Tensile Measurements of Young's Modulus for Soft Biological Tissues. *Tissue Eng Part B Rev* 2011;17:155–164. Available from: <https://www.liebertpub.com/doi/10.1089/ten.teb.2010.0520>
- McMahon D, Deng L, Hynynen K. Comparing rapid short-pulse to tone burst sonication sequences for focused ultrasound and microbubble-mediated blood-brain barrier permeability enhancement. *J Control Release Elsevier*, 2020;0–1. Available from: <https://doi.org/10.1016/j.jconrel.2020.10.004>
- Mehta AM, Sonabend AM, Bruce JN. Convection-Enhanced Delivery. *Neurotherapeutics* 2017;14:358–371.
- Meijlink B, Skachkov I, van der Steen AFW, de Jong N, Kooiman K. The Preparation of Chicken Ex Ovo Embryos and Chorioallantoic Membrane Vessels as In Vivo Model for Contrast-Enhanced Ultrasound Imaging and Microbubble-Mediated Drug Delivery Studies. *J Vis Exp* 2021;1–27.
- Miller DL, Averkiou MA, Brayman AA, Everbach EC, Holland CK, Wible JH, Wu J. Bioeffects considerations for diagnostic ultrasound contrast agents. *J Ultrasound Med* 2008;27:611–632.
- Miller DL, Qudus J. Diagnostic ultrasound activation of contrast agent gas bodies induces capillary rupture in mice. *Proc Natl Acad Sci U S A* 2000;97:10179–10184.
- Morse S V, Pouliopoulos AN, Chan TG, Copping MMJ, Lin J, Long MNJ, Choi JJ. Rapid Short-pulse Ultrasound Delivers Drugs Uniformly across the Murine Blood-Brain Barrier with Negligible Disruption. *Radiology* 2019; Available from: <https://doi.org/10.1148/radiol.2019181625>
- Nhan T, Burgess A, Cho EE, Stefanovic B, Lilge L, Hynynen K. Drug delivery to the brain by focused ultrasound induced blood-brain barrier disruption: Quantitative evaluation of enhanced permeability of cerebral vasculature using two-photon microscopy. *J Control Release Elsevier B.V.*, 2013;172:274–280. Available from: <http://dx.doi.org/10.1016/j.jconrel.2013.08.029>
- Nightingale K. Acoustic Radiation Force Impulse (ARFI) Imaging: a Review. *Curr Med Imaging Rev* 2012;7:328–339.
- Normand V, Lootens DL, Amici E, Plucknett KP, Aymard P. New insight into agarose gel mechanical properties. *Biomacromolecules* 2000;1:730–738.
- Nuriya M, Shinotsuka T, Yasui M. Diffusion Properties of Molecules at the Blood – Brain Interface : Potential Contributions of Astrocyte Endfeet to Diffusion Barrier Functions. *Cereb Cortex* 2013;2118–2126.
-



- 
- O'Reilly MA, Hynynen K. Blood-brain barrier: Real-time feedback-controlled focused ultrasound disruption by using an acoustic emissions-based controller. *Radiology* 2012;263:96–106.
- Ogunshola OO, Stewart WB, Mihalcik V, Solli T, Madri JA, Ment LR. Neuronal VEGF expression correlates with angiogenesis in postnatal developing rat brain. *Dev Brain Res* 2000;119:139–153.
- Ohl CD, Arora M, Ikink R, De Jong N, Versluis M, Delius M, Lohse D. Sonoporation from jetting cavitation bubbles. *Biophys J Elsevier*, 2006;91:4285–4295. Available from: <http://dx.doi.org/10.1529/biophysj.105.075366>
- Overvelde M, Garbin V, Dollet B, De Jong N, Lohse D, Versluis M. Dynamics of Coated Microbubbles Adherent to a Wall. *Ultrasound Med Biol* 2011;37:1500–1508.
- Owen J, Kamila S, Shrivastava S, Carugo D, Bernardino De La Serna J, Mannaris C, Pereno V, Browning R, Beguin E, McHale AP, Callan JF, Stride E. The Role of PEG-40-stearate in the Production, Morphology, and Stability of Microbubbles. *Langmuir* 2019;35:10014–10024.
- Oyen ML. Mechanical characterisation of hydrogel materials. *Int Mater Rev* 2014;59:44–59. Available from: <http://www.tandfonline.com/doi/full/10.1179/1743280413Y.0000000022>
- Pandit R, Koh WK, Sullivan RKP, Palliyaguru T, Parton RG, Götz J. Role for caveolin-mediated transcytosis in facilitating transport of large cargoes into the brain via ultrasound. *J Control Release Elsevier*, 2020;327:667–675. Available from: <https://doi.org/10.1016/j.jconrel.2020.09.015>
- Papouin T, Haydon P. Obtaining Acute Brain Slices. *Bio Protoc* 2018;20.
- Partyka PP, Godsey GA, Galie JR, Kosciuk MC, Acharya NK, Nagele RG, Galie PA. Mechanical stress regulates transport in a compliant 3D model of the blood-brain barrier. *Biomaterials Elsevier Ltd*, 2017;115:30–39. Available from: <http://dx.doi.org/10.1016/j.biomaterials.2016.11.012>
- Patching SG. Glucose Transporters at the Blood-Brain Barrier: Function, Regulation and Gateways for Drug Delivery. *Mol Neurobiol Molecular Neurobiology*, 2017;54:1046–1077.
- Patel MM, Goyal BR, Bhadada S V, Bhatt JS, Amin AF. Getting into the Brain: Approaches to Enhance Brain Drug Delivery. *CNS Drugs* 2009;23:35–58.
- Patel MM, Patel BM. Crossing the Blood–Brain Barrier: Recent Advances in Drug Delivery to the Brain. *CNS Drugs Springer International Publishing*, 2017;31:109–133.
- Postema M, Gilja OH. Jetting does not cause sonoporation. *Biomed Eng* 2010;55:19–20.
- Postema M, Marmottant P, Lancée CT, Hilgenfeldt S, Jong N De. Ultrasound-induced microbubble coalescence. *Ultrasound Med Biol* 2004;30:1337–1344.
- Pouliopoulos AN. Controlling microbubble dynamics in ultrasound therapy. Imperial College London, 2017.
- Pouliopoulos AN, Li C, Tinguely M, Garbin V, Tang M-X, Choi JJ. Rapid short-pulse sequences enhance the spatiotemporal uniformity of acoustically driven microbubble activity during flow conditions. *J Acoust Soc Am* 2016;140:2469–2480. Available from: <http://dx.doi.org/10.1121/1.4964271>
- Pouliopoulos AN, Smith CAB, Bezer JH, El Ghamrawy A, Bouldin CJ, Morse S V., Tang M-X, Choi JJ. Doppler passive acoustic mapping. *IEEE Trans Ultrason Ferroelectr Freq Control* 2020a;67:2692–2703.
-

- 
- Pouliopoulos AN, Wu SY, Burgess MT, Karakatsani ME, Kamimura HAS, Konofagou EE. A Clinical System for Non-invasive Blood–Brain Barrier Opening Using a Neuronavigation-Guided Single-Element Focused Ultrasound Transducer. *Ultrasound Med Biol* 2020b;46:73–89.
- Prentice P, Cuschieri A, Dholakia K, Prausnitz M, Campbell P. Membrane disruption by optically controlled microbubble cavitation. *Nat Phys* 2005;1:107–110.
- Qin S, Caskey CF, Ferrara KW. Ultrasound contrast microbubbles in imaging and therapy: Physical principles and engineering. *Phys Med Biol* 2009;54.
- Qin S, Ferrara KW. Acoustic response of compliant microvessels containing ultrasound contrast agents. *Phys Med Biol* 2006;51:5065–5088.
- Ramnarine K V, Garrard JW, Kanber B, Nduwayo S, Hartshorne TC, Robinson TG. Shear wave elastography imaging of carotid plaques: feasible, reproducible and of clinical potential. *Cardiovasc Ultrasound* 2014;12:1–8. Available from: <http://www.cardiovascularultrasound.com/content/12/1/49>
- Raymond SB, Skoch J, Hynynen K, Bacskai BJ. Multiphoton imaging of ultrasound/Optison mediated cerebrovascular effects in vivo. *J Cereb Blood Flow Metab* 2007;27:393–403.
- Roovers S, Segers T, Lajoinie G, Deprez J, Versluis M, De Smedt SC, Lentacker I. The Role of Ultrasound-Driven Microbubble Dynamics in Drug Delivery: From Microbubble Fundamentals to Clinical Translation. *Langmuir* 2019;35:10173–10191.
- Saharkhiz N, Koruk H, Choi JJ. The effects of ultrasound parameters and microbubble concentration on acoustic particle palpation. *J Acoust Soc Am* 2018;144:796–805.
- Sarkaria JN, Hu LS, Parney IF, Pafundi DH, Brinkmann DH, Laack NN, Giannini C, Burns TC, Kizilbash SH, Laramy JK, Swanson KR, Kaufmann TJ, Brown PD, Agar NYR, Galanis E, Buckner JC, Elmquist WF. Is the blood-brain barrier really disrupted in all glioblastomas? A critical assessment of existing clinical data. *Neuro Oncol* 2018;20:184–191.
- Sassaroli E, Hynynen K. Resonance frequency of microbubbles in small blood vessels : a numerical study Resonance frequency of microbubbles in small blood vessels : a numerical study. *Phys Med Biol* 2005;
- Saunders NR, Dziegielewska KM, Møllgård K, Habgood MD. Markers for blood-brain barrier integrity: How appropriate is Evans blue in the twenty-first century and what are the alternatives? *Front Neurosci* 2015;9:1–16.
- Scemes E, Guame C. Astrocyte Calcium Waves: What are they and what do they do. *Glia* 2006;54:716–725.
- Schindelin J, Arganda-Carreras I, Frise E, Kaynig V, Longair M, Pietzsch T, Preibisch S, Rueden C, Saalfeld S, Schmid B, Tinevez JY, White DJ, Hartenstein V, Eliceiri K, Tomancak P, Cardona A. Fiji: An open-source platform for biological-image analysis. *Nat Methods* 2012;9:676–682.
- Schmitt G, Parrott N, Prinssen E, Barrow P. The great barrier belief : The blood – brain barrier and considerations for juvenile toxicity studies. *Reprod Toxicol Elsevier Inc.*, 2017;72:129–135. Available from: <http://dx.doi.org/10.1016/j.reprotox.2017.06.043>
- Schneider M. Characteristics of SonoVue(TM). *Echocardiography* 1999;16:743–746.
- Şen T, Tüfekçioğlu O, Koza Y. Mechanical index. *Anadolu Kardiyol Derg* 2015;15:334–336.
- Sennoga CA, Mahue V, Loughran J, Casey J, Seddon JM, Tang M, Eckersley RJ. On sizing and counting of microbubbles using optical microscopy. *Ultrasound Med Biol* 2010;36:2093–2096.
-

- 
- Shamout FE, Pouliopoulos AN, Lee P, Bonaccorsi S, Towhidi L, Krams R, Choi JJ. Enhancement of Non-Invasive Trans-Membrane Drug Delivery Using Ultrasound and Microbubbles During Physiologically Relevant Flow. *Ultrasound Med Biol* 2015;41:2435–2448.
- Sheeran PS, Dayton PA. Phase-Change Contrast Agents for Imaging and Therapy. *Curr Pharm Des* 2016;18:2152–2165.
- Sheikov N, McDannold N, Jolesz F, Zhang Y-Z, Tam K, Hynynen K. Brain arterioles show more active vesicular transport of blood-borne tracer molecules than capillaries and venules after focused ultrasound-evoked opening of the blood-brain barrier. *Ultrasound Med Biol* 2006;32:1399–1409.
- Sheikov N, McDannold N, Sharma S, Hynynen K. Effect of focused ultrasound applied with an ultrasound contrast agent on the tight junctional integrity of the brain microvascular endothelium. *Ultrasound Med Biol* 2008;34:1093–1104.
- Sheikov N, McDannold N, Vykhodtseva N, Jolesz F, Hynynen K. Cellular mechanisms of the blood-brain barrier opening induced by ultrasound in presence of microbubbles. *Ultrasound Med Biol* 2004;30:979–989.
- Shen Y, Guo J, Chen G, Chin CT, Chen X, Chen J, Wang F, Chen S, Dan G. Delivery of liposomes with different sizes to mice brain after sonication by focused ultrasound in the presence of microbubbles. *Ultrasound Med Biol* 2016;42:1499–1511.
- Shi WT, Forsberg F, Raichlen JS, Needleman L, Goldberg BB. Pressure dependence of subharmonic signals from contrast microbubbles. *Ultrasound Med Biol Elsevier*, 1999 [cited 2018 Jan 23];25:275–283. Available from: <https://www.sciencedirect.com/science/article/pii/S030156299800163X>
- Shiina T, Nightingale KR, Palmeri ML, Hall TJ, Bamber JC, Barr RG, Castera L, Choi BI, Chou Y-H, Cosgrove D, Dietrich CF, Ding H, Amy D, Farrokh A, Ferraioli G, Filice C, Friedrich-Rust M, Nakashima K, Schafer F, Sporea I, Suzuki S, Wilson S, Kudo M. WFUMB Guidelines and Recommendations for Clinical Use of Ultrasound Elastography: Part 1: Basic Principles and Terminology. *Ultrasound Med Biol* 2015;41:1126–1147. Available from: <http://linkinghub.elsevier.com/retrieve/pii/S0301562915002227>
- Shin J, Kong C, Cho JS, Lee J, Koh CS, Yoon MS, Na YC, Chang WS, Chang JW. Focused ultrasound-mediated noninvasive blood-brain barrier modulation: Preclinical examination of efficacy and safety in various sonication parameters. *Neurosurg Focus* 2018;44:1–10.
- Shirota E, Ando K. Estimation of mechanical properties of gelatin using a microbubble under acoustic radiation force. *J Phys Conf Ser* 2015;656.
- Shortencarrier MJ, Dayton PA, Bloch SH, Schumann PA, Matsunaga TO, Ferrara KW. A method for radiation-force localized drug delivery using gas-filled lipospheres. *IEEE Trans Ultrason Ferroelectr Freq Control IEEE*, 2004;51:822–831.
- Sirsi SR, Borden MA. State-of-the-art materials for ultrasound-triggered drug delivery. *Adv Drug Deliv Rev Elsevier B.V.*, 2014;72:3–14. Available from: <http://dx.doi.org/10.1016/j.addr.2013.12.010>
- Sivandzade F, Cucullo L. In-vitro blood–brain barrier modeling: A review of modern and fast-advancing technologies. *J Cereb Blood Flow Metab* 2018;38:1667–1681.
- Skyba DM, Price RJ, Linka AZ, Skalak TC, Kaul S. Direct in vivo visualization of intravascular destruction of microbubbles by ultrasound and its local effects on tissue. *Circulation* 1998;98:290–293.
-

- 
- Smyth C, Kudryashov ED, Buckin V. High-frequency shear and volume viscoelastic moduli of casein particle gel. *Colloids Surfaces A* 2001;517–526. Available from: [papers3://publication/uuid/1EAD458E-8815-48ED-8567-B89A175DEE87](https://papers3://publication/uuid/1EAD458E-8815-48ED-8567-B89A175DEE87)
- Steinman J, Koletar MM, Stefanovic B, Sled JG. 3D morphological analysis of the mouse cerebral vasculature: Comparison of in vivo and ex vivo methods. *PLoS One* 2017;12:1–17.
- Supponen O, Upadhyay A, Lum J, Guidi F, Murray T, Vos HJ, Tortoli P, Borden M. The effect of size range on ultrasound-induced translations in microbubble populations. *J Acoust Soc Am* Acoustical Society of America, 2020;147:3236–3247.
- Tarnoki DL, Tarnoki AD, Sukosd H, Folhoffer A, Harkanyi Z. Delayed contrast enhancement of hepatic parenchyma after intravenous sonographic contrast agent: unusual phenomenon. Case report and review of literature. *J Ultrasound Springer International Publishing*, 2021;24:3–9. Available from: <https://doi.org/10.1007/s40477-020-00429-y>
- ter Haar G. Safety and bio-effects of ultrasound contrast agents. *Med Biol Eng Comput* 2009;47:893–900.
- ter Haar G, Coussios C. High intensity focused ultrasound : Physical principles and devices. 2007;23:89–104.
- Tse JR, Engler AJ. Preparation of hydrogel substrates with tunable mechanical properties. *Curr Protoc Cell Biol* 2010;1–16.
- Tu J, Guan J, Qiu Y, Matula TJ. Estimating the shell parameters of SonoVue<sup>®</sup> microbubbles using light scattering. *J Acoust Soc Am* 2009;126:2954–2962.
- Tyler WJ. Noninvasive neuromodulation with ultrasound? A continuum mechanics hypothesis. *Neuroscientist* 2011;17:25–36.
- van der Meer SM, Dollet B, Voormolen MM, Chin CT, Bouakaz A, de Jong N, Versluis M, Lohse D. Microbubble spectroscopy of ultrasound contrast agents. *J Acoust Soc Am* 2007;121:648–656. Available from: <http://asa.scitation.org/doi/10.1121/1.2390673>
- Van Tellingen O, Yetkin-Arik B, De Gooijer MC, Wesseling P, Wurdinger T, De Vries HE. Overcoming the blood-brain tumor barrier for effective glioblastoma treatment. *Drug Resist Updat Elsevier Ltd*, 2015;19:1–12. Available from: <http://dx.doi.org/10.1016/j.drug.2015.02.002>
- van Wamel A, Kooiman K, Harteveld M, Emmer M, ten Cate FJ, Versluis M, de Jong N. Vibrating microbubbles poking individual cells: Drug transfer into cells via sonoporation. *J Control Release* 2006;112:149–155.
- Versluis M, Goertz DE, Palanchon P, Heitman IL, Van Der Meer SM, Dollet B, De Jong N, Lohse D. Microbubble shape oscillations excited through ultrasonic parametric driving. *Phys Rev E - Stat Nonlinear, Soft Matter Phys* 2010;82:2–7.
- Vos HJ, Guidi F, Boni E, Tortoli P. Method for microbubble characterization using primary radiation force. *IEEE Trans Ultrason Ferroelectr Freq Control* 2007;54:1333–1344.
- Vykhodtseva NI, Hynynen K, Damianou C. Histologic effects of high intensity pulsed ultrasound exposure with subharmonic emission in rabbit brain in vivo. *Ultrasound Med Biol* 1995;21:969–979.
- Wang JD, Khafagy ES, Khanafer K, Takayama S, Elsayed MEH. Organization of Endothelial Cells, Pericytes, and Astrocytes into a 3D Microfluidic in Vitro Model of the Blood-Brain Barrier. *Mol Pharm* 2016;13:895–906.
-

- 
- Wang S, Wang Q, Zhang A, Stride E. Experimental observations of the behaviour of a bubble inside a circular rigid tube. *Int J Multiph Flow Elsevier Ltd*, 2019;121:103096. Available from: <https://doi.org/10.1016/j.ijmultiphaseflow.2019.103096>
- Wang S, Zhang A, Liu Y, Zeng D. Numerical simulation of bubble dynamics in an elastic vessel. *Eur Phys J E* 2013;36.
- Waterhouse RN. Determination of lipophilicity and its use as a predictor of blood-brain barrier penetration of molecular imaging agents. *Mol Imaging Biol* 2003;5:376–389.
- Wells PNT. Ultrasound imaging. *Phys Med Biol* 2006;51.
- Wiedemair W, Tukovic Z, Jasak H, Poulikakos D, Kurtcuoglu V. Modeling the interaction of microbubbles: Effects of proximity, confinement, and excitation amplitude. *Phys Fluids* 2014;26. Available from: <http://dx.doi.org/10.1063/1.4883482>
- Wilson S, Burns P. Microbubble-enhanced US in body imaging: What role? *Radiology* 2010;257:24–39.
- Wu SK, Chu PC, Chai WY, Kang ST, Tsai CH, Fan CH, Yeh CK, Liu HL. Characterization of different microbubbles in assisting focused ultrasound-induced blood-brain barrier opening. *Sci Rep Nature Publishing Group*, 2017;7:1–11.
- Yanagisawa K, Moriyasu F, Miyahara T, Yuki M, Iijima H. Phagocytosis of ultrasound contrast agent microbubbles by Kupffer cells. *Ultrasound Med Biol* 2007;33:318–325.
- Yeh WC, Li PC, Jeng YM, Hsu HC, Kuo PL, Li ML, Yang PM, Po HL. Elastic modulus measurements of human liver and correlation with pathology. *Ultrasound Med Biol* 2002;28:467–474.
- Yin X, Hynynen K. A numerical study of transcranial focused ultrasound beam propagation at low frequency. *Phys Med Biol* 2005;50:1821–1836.
- Yoon S, Aglyamov SR, Karpouk AB, Kim S, Emelianov SY. Estimation of mechanical properties of a viscoelastic medium using a laser-induced microbubble interrogated by an acoustic radiation force. *J Acoust Soc Am* 2011;130:2241–2248. Available from: <http://asa.scitation.org/doi/10.1121/1.3628344>
- Yu T, Wang G, Hu K, Ma P, Bai J, Wang Z. A microbubble agent improves the therapeutic efficiency of high intensity focused ultrasound : a rabbit kidney study. *Urol Res* 2004;14–19.
- Yu T, Xiong S, Mason TJ, Wang Z. The use of a microbubble agent to enhance rabbit liver destruction using high intensity focused ultrasound. *Ultrason - Sonochemistry* 2006;143–149.
- Zhang G, Harput S, Lin S, Christensen-Jeffries K, Leow CH, Brown J, Dunsby C, Eckersley RJ, Tang MX. Acoustic wave sparsely activated localization microscopy (AWSALM): Super-resolution ultrasound imaging using acoustic activation and deactivation of nanodroplets. *Appl Phys Lett* 2018;113. Available from: <http://dx.doi.org/10.1063/1.5029874>
- Zhang L, Zhang W, Orsi F, Chen W, Wang Z. Ultrasound-guided high intensity focused ultrasound for the treatment of gynaecological diseases: A review of safety and efficacy. *Int J Hyperther* 2015;31:280–284.
- Zhao B, Chen Y, Liu J, Zhang L, Wang J, Yang Y, Lv Q, Xie M. Blood-brain barrier disruption induced by diagnostic ultrasound combined with microbubbles in mice. *Oncotarget* 2018;9:4897–4914.
- Zhou H, Liu Y, Long X, Qiao Y, Lee J, Liu X, Zheng H, Zou C. MR-guided blood-brain barrier opening induced by rapid short-pulse ultrasound in non-human primates. *Quant Imaging Med Surg* 2021;11:2415–2427.
-

Zhu X, Siamantouras E, Liu KK, Liu X. Determination of work of adhesion of biological cell under AFM bead indentation. *J Mech Behav Biomed Mater* 2016;56:77–86.